

4

RADC-TR-89-75
Final Technical Report
June 1989



AD-A215 643

CHEMICAL PROFILING OF SILICON NITRIDE STRUCTURES

Jet Propulsion Laboratory

R. P. Vasquez

APPROVED FOR PUBLIC RELEASE; DISTRIBUTION UNLIMITED.

ROME AIR DEVELOPMENT CENTER
Air Force Systems Command
Griffiss Air Force Base, NY 13441-5700

DTIC
ELECTE
NOV 24 1989

S B D

This report has been reviewed by the RADC Public Affairs Division (PA) and is releasable to the National Technical Information Service (NTIS). At NTIS it will be releasable to the general public, including foreign nations.

RADC-TR-89-75 has been reviewed and is approved for publication.

APPROVED:



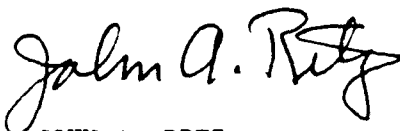
PETER J. DREVINSKY
Project Engineer

APPROVED:



HAROLD ROTH
Director of Solid State Sciences

APPROVED:



JOHN A. RITZ
Directorate of Plans & Programs

If your address has changed or if you wish to be removed from the RADC mailing list, or if the addressee is no longer employed by your organization, please notify RADC (ESRH) Hanscom AFB MA 01731-5000. This will assist us in maintaining a current mailing list.

Do not return copies of this report unless contractual obligations or notices on a specific document require that it be returned.

UNCLASSIFIED

SECURITY CLASSIFICATION OF THIS PAGE

REPORT DOCUMENTATION PAGE				Form Approved OMB No 0704-0188	
1a REPORT SECURITY CLASSIFICATION UNCLASSIFIED			1b RESTRICTIVE MARKINGS N/A		
2a SECURITY CLASSIFICATION AUTHORITY N/A			3 DISTRIBUTION/AVAILABILITY OF REPORT Approved for public release; distribution unlimited.		
2b DECLASSIFICATION/DOWNGRADING SCHEDULE N/A			5 MONITORING ORGANIZATION REPORT NUMBER(S) RADC-TR-89-75		
4 PERFORMING ORGANIZATION REPORT NUMBER(S) N/A			7a NAME OF MONITORING ORGANIZATION Rome Air Development Center (ESRH)		
6a NAME OF PERFORMING ORGANIZATION Jet Propulsion Laboratory		6b OFFICE SYMBOL (If applicable) N/A		7b ADDRESS (City, State, and ZIP Code) Hanscom AFB MA 01731-5000	
8a NAME OF FUNDING SPONSORING ORGANIZATION National Aeronautics and Space Administration Headquarters		8b OFFICE SYMBOL (If applicable) N/A		9 PROCUREMENT INSTRUMENT IDENTIFICATION NUMBER FQ761940038	
3c ADDRESS (City, State, and ZIP Code) Code 3FH-7 Washington DC 20546		10 SOURCE OF FUNDING NUMBERS			
		PROGRAM ELEMENT NO 61102F		PROJECT NO 2306	
		TASK NO J3		WORK UNIT 26	
11 TITLE (Include Security Classification) CHEMICAL PROFILING OF SILICON NITRIDE STRUCTURES					
12 PERSONAL AUTHOR(S) R. P. Vasquez					
13a TYPE OF REPORT Final		13b TIME COVERED FROM Oct 85 to Jun 87		14 DATE OF REPORT (Year, Month, Day) June 1989	
15 PAGE COUNT 138					
16 SUPPLEMENTARY NOTATION N/A					
17 EOSAT CODES			18 SUBJECT TERMS (Continue on reverse if necessary and identify by block number)		
FIELD	GROUP	SUB-GROUP			
09	01		Spectroscopy; nitridation, microscopy		
09	08				
19 ABSTRACT (Continue on reverse if necessary and identify by block number) X-ray photoelectron spectroscopy (XPS), spectroscopic ellipsometry (SE), and scanning electron microscopy (SEM) have been used to study structural and chemical inhomogeneities in several electronic materials and device structures of relevance to radiation hard electronics. The systems studied include metal-nitride-oxide-semiconductor (MNOS) structures, silicon oxynitride (SiO_xN_y) formed by the thermal nitridation of SiO_2 , and semiconductor-on-insulator (SOI) structures. Studies of MNOS structures suggest that the effect of H_2 annealing is to make the $\text{Si}_3\text{N}_4/\text{SiO}_2$ interface less abrupt by causing interdiffusion of silanol and silamine groups with subsequent oxynitride formation. Another effect of the annealing appears to be to relieve the strain at the SiO_2/Si interface.					
20 DISTRIBUTION/AVAILABILITY OF ABSTRACT <input checked="" type="checkbox"/> UNCLASSIFIED/UNLIMITED <input type="checkbox"/> SAME AS RPT <input type="checkbox"/> DTIC USERS			21 ABSTRACT SECURITY CLASSIFICATION UNCLASSIFIED		
22a NAME OF RESPONSIBLE INDIVIDUAL Recal J. Drevinsky			22b TELEPHONE (Include Area Code) 22c OFFICE SYMBOL (617) 337-2367 RADC (ESRH)		

Table of Contents

Chapter 1: Introduction	1
Chapter 2: Studies of Metal-Nitride-Oxide-Semiconductor (MNOS) Structures	12
Chapter 3: Studies of $\text{SiO}_2\text{N}_x/\text{Si}$ Formed by the Thermal Nitridation of SiO_2/Si	16
I. Kinetics of Nitridation: Background	16
II. Experimental	22
III. XPS Measurements	24
III. A. Nitrogen Distributions	24
III. B. Defect Distributions	32
IV. Modeling of the Kinetics of Nitridation	45
IV. A. The Nitridation Process	45
IV. B. The Kinetic Model	48
IV. C. Choice of Kinetic Parameters	55
IV. D. Results and Discussion	63
V. Spectroscopic Ellipsometry Measurements	75
VI. Summary and Conclusions	86
Chapter 4: Studies of Semiconductor-on-Insulator (SOI) Structures	88
I. Introduction	88
II. SOI Formed by Ion Implantation	89
III. SOI Formed by Zone-Melting Recrystallization (ZMR)	99
Chapter 5: Conclusions	102

on For

A&I

ed

tion

tion/

Availability Codes

Avail and/or

Dist

Special

A-1

References	106
Appendix A: Intensity Analysis of XPS Data	114

Chemical Profiling of Silicon Nitride Structures

Abstract

X-ray photoelectron spectroscopy (XPS), spectroscopic ellipsometry (SE), and scanning electron microscopy (SEM) have been used to study structural and chemical inhomogeneities in several electronic materials and device structures of relevance to radiation hard electronics. The systems studied include metal-nitride-oxide-semiconductor (MNOS) structures, silicon oxynitride (SiO_xN_y) formed by the thermal nitridation of SiO_2 , and semiconductor-on-insulator (SOI) structures. Studies of MNOS structures suggest that the effect of H_2 annealing is to make the $\text{Si}_3\text{N}_4/\text{SiO}_2$ interface less abrupt by causing interdiffusion of silanol and silamine groups with subsequent oxynitride formation. Another effect of the annealing appears to be to relieve the strain at the SiO_2/Si interface.

The chemical and structural inhomogeneities in SiO_xN_y formed by the thermal nitridation in NH_3 of SiO_2/Si have been studied. The nitrogen concentration depth profile as a function of nitridation time and temperature has been measured with XPS. The peak interfacial nitrogen concentration initially occurs at the $\text{SiO}_x\text{N}_y/\text{Si}$ interface, then appears to move away from the interface with increasing nitridation time for sufficiently high nitridation temperatures. The kinetics of nitridation has been modeled, and reasonable agreement is obtained with the experimental results, provided the effects of interfacial strain are explicitly taken into account. Electrical data in the literature are found to be correlated with the nitrogen distributions measured

here, and are explained within a model based on the strain-dependent formation of defect states.

Studies of SOI structures formed by ion implantation show that the buried oxide/Si interfaces are smoother with higher implantation temperatures in the range 400° C to 525° C. However, the stoichiometry of the native oxides and thermal SiO₂/Si interface suggests that a higher implantation temperature results in a rougher surface, which may possibly affect device characteristics. SOI structures formed by zone-melting recrystallization have also been studied, but these studies are incomplete at this time.

Figures

2.1.	Schematic diagram of the system used for gas phase XeF_2 etching of Si.	13
3.1.	N 1s and O 1s photoelectron peak intensities, $I_{\text{N}1s}$ and $I_{\text{O}1s}$, measured during the course of depth profiling sample 1, corrected for photoionization cross section differences.	25
3.2.	$I_{\text{N}1s}/(I_{\text{O}1s} + I_{\text{N}1s})$ for (a) sample 1, and (b) sample 2, corrected for photoionization cross section differences.	27
3.3.	Distribution of N in SiO_xN_y produced from a 100 Å-thick SiO_2 film grown in dry O_2 at 1000°C, then nitrided at 1000°C for (a) 10 minutes, (b) 30 minutes, (c) 120 minutes.	28
3.4.	Distribution of N in SiO_xN_y produced by nitriding a 100 Å-thick SiO_2 film at 1150°C for (a) 5 minutes, and (b) 10 minutes.	30
3.5.	(a) Comparison of the distribution of N in SiO_xN_y films produced from 100 Å-thick SiO_2 films grown in dry O_2 at 825°C (solid circles) and 1000°C (open circles), then nitrided at 800°C for 60 minutes. (b) Distribution of N in a SiO_xN_y film produced from a 100 Å-thick SiO_2 film nitrided at 800°C for 240 minutes.	31
3.6.	(a) Magnitude of the flatband voltage shift $ \Delta V_{\text{FB}} $ as a function of nitridation time t_{N} , for 600-Å-thick oxides nitrided at 1000°C (from Ref. 57). (b) Peak interfacial nitrogen concentration $[\text{N}]_p$ and distance of $[\text{N}]_p$ from the interface as functions of t_{N} , for a 100-Å-thick oxide nitrided at 1000°C (from Fig. 3.3).	33
3.7.	Schematic representation of the distribution of defects at various nitridation times. Inset: Schematic diagram of the free energy of formation ΔG_{F} vs. configuration coordinate for the formation of $\text{SiO}_x\text{N}_y/\text{Si}$ without defects (solid line) and with defects (dashed line) to relieve strain energy.	36
3.8.	Surface fluorine concentrations measured during the course of depth profiles of samples nitrided at 1000°C for (a) 10 minutes, and (b) 30 minutes.	40

3.9.	Surface fluorine concentrations measured during the course of depth profiles of samples nitrided at 1150°C for (a) 5 minutes, and (b) 10 minutes.	42
3.10.	Surface fluorine concentrations measured during the course of depth profiles of samples (a) oxidized at 825°C, then nitrided at 800°C for 60 minutes, (b) oxidized at 1000°C, then nitrided at 800°C for 60 minutes, and (c) oxidized at 1000°C, then nitrided at 800°C for 240 minutes.	43
3.11.	Schematic overview of the kinetic model.	51
3.12.	Calculated distribution of N in a SiO_xN_y film produced by nitriding a 92 Å-thick SiO_2 film at 1000°C for (a) 5 minutes, (b) 10 minutes, (c) 20 minutes, and (d) 30 minutes.	64
3.13.	(a) Calculated curve from Fig. 3.12(d). (b) Effect of including an activation energy for nitrogen incorporation in the oxide which decreases linearly within 26 Å of the interface as the interface is approached. (c) Same as (b), but including activation energies for hopping of diffusing species in the oxynitride which decrease linearly in the interfacial region. (d) Same as (c) but extending the region of graded reactivity to include the two Si layers in the substrate which are closest to the $\text{SiO}_x\text{N}_y/\text{Si}$ interface.	66
3.14.	Comparison of the experimental nitrogen distribution in a SiO_xN_y film, produced from a 100 Å-thick SiO_2 film nitrided for 30 minutes at 1000°C (squares, from Fig. 3.3(b)), to the calculated nitrogen distributions (a) from Fig. 3.13(a), and (b) from Fig. 3.13(d).	67
3.15.	Comparison of the experimental nitrogen distribution in a SiO_xN_y film, produced from a 100 Å-thick SiO_2 film nitrided for 10 minutes at 1150°C (squares, from Fig. 3.4(b)), to the calculated nitrogen distribution (a) using the same kinetic parameters as in Fig. 3.13(d), and (b) including the effects of a reversible nitridation.	69
3.16.	Comparison of the experimental data points from Fig. 3.3(b) (squares) to the calculated nitrogen distribution using the same kinetic parameters as in Fig. 3.15(b) for a 30 minute nitridation at 1000°C.	71

3.17	Comparison of the experimental nitrogen distribution in SiO_2/N_2 films, produced from 100 Å-thick SiO_2 films nitrided for 60 minutes at 800°C (solid and open circles, from Fig. 3.5(a)), to the calculated nitrogen distribution (a) using kinetic parameters appropriate for low temperature nitridation, and (b) using kinetic parameters appropriate for high temperature nitridation.	72
3.18	Calculated nitrogen distribution using the same kinetic parameters as Fig. 3.13(d) for a 30 minute nitridation at 1000°C for an initial oxide thickness of (a) 100 Å, (b) 150 Å, and (c) 200 Å.	74
3.19	Spectra of $\tan \psi$ obtained for (a) a 1030 Å-thick layer of SiO_2 on Si, (b) a 1030 Å-thick layer of SiO_2 on Si, nitrided for 2 hours at 800°C, and (c) a 1030 Å-thick layer of SiO_2 on Si, nitrided for 2 hours at 1000°C.	77
3.20	Spectra of $\cos \Delta$ corresponding to the data in Fig. 3.19.	78
3.21	Best fit to the data from Figs. 3.19(c) and 3.20(c), obtained using a single-layer model in which the dielectric consists of a physical mixture of SiO_2 and Si_3N_4 . Only the fit to $\cos \Delta$ is shown, since $\tan \psi$ could be fit well enough that no difference between the data and the fit is apparent to the eye.	80
3.22	Comparison of $\tan \psi$ spectra obtained from sample 11 using aperture sizes of 0.6 mm and 2 mm.	81
3.23	Comparison of $\cos \Delta$ spectra obtained from sample 11 using aperture sizes of 0.6 mm and 2 mm.	82
3.24	Calculated spectrum of $\tan \psi$ for a 1030 Å-thick dielectric on Si, consisting of a physical mixture of 10% Si_3N_4 and 90% SiO_2 , in the energy range 0.5-5.7 eV.	84
3.25	Calculated spectrum of $\cos \Delta$ for a 1030 Å-thick dielectric on Si, consisting of a physical mixture of 10% Si_3N_4 and 90% SiO_2 , in the energy range 0.5-5.7 eV.	85
4.1	SEM micrographs of the surfaces of SOI samples formed by ion implantation of oxygen at (a) 500°C, no anneal, (b) 425°C, 2 hour 1150°C post-implantation anneal, (c) 500°C, 2 hour 1150°C anneal, and (d) 525°C, 2 hour 1150°C anneal.	91
4.2	XPS spectra of the Si 2p region for the samples corresponding to the data in Fig. 4.1.	92

4.3.	SEM micrographs (magnification 10-13kx) of the surfaces of SOI samples formed by ion implantation of oxygen at (a) 500°C, no anneal, (b) 425°C, 2 hour 1150°C post-implantation anneal, (c) 500°C, 2 hour 1150°C anneal, and (d) 525°C, 2 hour 1150°C anneal. The surface Si layer has been removed by XeF_2 etching, exposing the buried oxide.	94
4.4.	Same as Fig. 4.3, but with a magnification of 65kx.	95
4.5.	SEM micrographs (magnification 50kx) of the surfaces of SOI samples formed by ion implantation of oxygen at (a) 500°C, no anneal, (b) 425°C, 2 hour 1150°C post-implantation anneal, (c) 500°C, 2 hour 1150°C anneal, and (d) 525°C, 2 hour 1150°C anneal. The surface Si layer has been removed by XeF_2 etching, and the buried oxide layer has been removed with HF, exposing the buried oxide/substrate interface.	97
4.6.	Same as Fig. 4.5, but with a magnification of 200kx.	98

Tables

I. Summary of the oxidation and nitridation conditions for the samples used in this work.	23
II. Summary of the kinetic parameters used in this work.	62

Chapter 1

Introduction

The results of studies of materials and device structures of relevance to radiation hard electronics is reported herein. This work is a follow-on to a research project (JPL Task Plan #90-1276) performed by JPL for RADC and involves a coordinated study aimed at understanding the chemical and structural features which limit the radiation stability of devices, particularly those based on silicon nitride and oxynitride dielectric films. The participants have been Westinghouse, JPL, MIT Lincoln Laboratory, and the University of Surrey, England, UK. The structures studied include metal-nitride-oxide-semiconductor (MNOS) structures, silicon oxynitride (SiO_xN_y) films formed by the thermal nitridation of SiO_2 films in NH_3 , and semiconductor-on-insulator (SOI) structures. The objectives of the study are to determine the chemical structure of silicon nitride and oxynitride and their interfaces with Si and SiO_2 , to identify the key defects, and to model the mechanism of defect generation which may limit device performance.

Many proposed electronic device structures require insulator or semiconductor thin films which are only a few lattice constants thick. For example, megabit dynamic random access memory devices require an insulator thickness near 100 Å. In the past, defects and inhomogeneities on an atomic scale could often be ignored since they were so much smaller than device dimensions. As device dimensions become smaller, an understanding of interfacial properties, defects, and inhomogeneities on an atomic

scale becomes increasingly important.

Defects and inhomogeneities can be classified as being either structural or chemical. Structural defects include extended defects such as grain boundaries and dislocations, and defects on an atomic scale, such as bond angle distortions, voids, and dangling orbitals. Chemical inhomogeneities include inhomogeneous distributions of constituents in a random alloy (alloy clustering), a logical extension of which is phase separation in the context of metastable alloys. In this work, neither extended structural defects nor chemical inhomogeneities such as trace impurities will be considered.

It is to be noted that any interface between two different materials is inherently inhomogeneous, both structurally and chemically. Structural inhomogeneities arise from lattice mismatch between the two materials, which can be accommodated by lattice distortion of one or both materials, or by defects which allow both materials to retain their preferred lattice dimensions. Chemical inhomogeneities arise from the fact that the interface is a boundary between chemically distinct phases, so that interfacial atoms necessarily have bonding which is different than that found in either bulk material.

Amorphous materials are inherently structurally inhomogeneous, in the sense that the atoms do not occupy well-defined lattice sites, *i.e.* the material is topologically disordered. Amorphous materials can be chemically homogeneous, however. A chemically homogeneous amorphous material which has been extensively studied¹⁻³ is SiO_2 , which consists of Si tetrahedra connected by bridging oxygens in a ring structure. Bulk amorphous SiO_2 ($\alpha\text{-SiO}_2$) consists primarily of 6-membered rings.

corresponding to an Si-O-Si bridging bond angle of 144° , the same as that found in α -quartz. Amorphous SiO_2 differs from α -quartz in having a significant void fraction, manifested in a lower density (2.65 g/cm^3 for α -quartz vs. 2.2 g/cm^3 for $a\text{-SiO}_2$), in a distribution of Si-O-Si bond angles, and hence in a distribution of ring sizes. These distributions are affected by strain; specifically, the strain which is localized within 30 \AA of the SiO_2/Si interface in thermally grown oxides on Si has been shown^{1,2} to result in a higher proportion of 4-membered rings (Si-O-Si bridging bond angle of 120°) in the interfacial region compared to the unstrained bulk SiO_2 . The results of these studies¹⁻³ have important implications for this work, as will be seen.

Another amorphous material which is ideally homogeneous chemically is Si_3N_4 . The study of CVD Si_3N_4 and its interface with SiO_2 in MNOS structures was the primary work of the previous task, and the results are described elsewhere.⁴⁻⁹ Some follow-on work has been done in this task, concerning the effects of H_2 annealing on the Si_3N_4 and the $\text{Si}_3\text{N}_4/\text{SiO}_2$ interface, and the results are described herein.

Amorphous alloys may exhibit chemical inhomogeneities in addition to the structural inhomogeneities which are inherent in amorphous materials. In this work, SiO_xN_y is an example of a material with both chemical and structural inhomogeneities. The SiO_xN_y has been formed by the thermal nitridation in NH_3 of SiO_2 films on Si. As previously mentioned, the structures of SiO_2 and the SiO_2/Si interface have been extensively studied, so that the initial state of the sample prior to nitridation has been characterized. Any chemical inhomogeneities which arise during the

nitridation can be followed by measuring the nitrogen distribution in the film at various nitridation times. It may thus be possible to elucidate the mechanism and kinetics of the nitridation process, and to relate the chemical inhomogeneities to the known structural inhomogeneities present in the initial SiO_2 film. Specifically, the strain which is present at the SiO_2/Si interface may affect the nitridation kinetics. These studies have been done,¹⁰⁻¹⁸ and the results are described here.

Two types of SOI structures have also been studied. The first type is formed by the high dosage implantation of O ions into a crystalline Si wafer at elevated temperatures, followed by a high temperature anneal to redistribute the implanted oxygen and form a buried SiO_2 layer. Samples of this type were obtained from Dr. Peter Hemment of the University of Surrey, England. Studies on similar samples have been done, and the results are reported elsewhere.¹⁹⁻²² The second type of SOI structure studied is formed by growing a thick thermal SiO_2 layer on a crystalline Si substrate, depositing polycrystalline Si on top, and depositing a thick SiO_2 capping layer over the poly-Si. The entire structure is heated, and a graphite strip heater is passed over the top to melt the poly-Si and recrystallize it as a single crystal Si layer. Samples of this type were obtained from Dr. C. K. Chen of MIT Lincoln Laboratory. Studies on similar samples have been done, and the results are reported elsewhere.²³

In order to study the problems discussed above, three techniques, which are in many ways complementary, have been utilized: x-ray photoelectron spectroscopy (XPS), scanning electron microscopy (SEM), and spectroscopic

ellipsometry (SE). SEM is a standard technique for imaging morphological features on surfaces. A detailed description of the technique and its applications can be found in many texts,²⁴ and will not be described here. XPS, also known as ESCA (electron spectroscopy for chemical analysis), is based on the photoelectric effect, in which photons incident on a specimen are absorbed and electrons are emitted. Only a brief description of the basic concepts is presented below, since excellent reviews are available in the literature.²⁵⁻²⁸ The XPS spectrometer used in this work is described elsewhere.¹

The binding energy of an electron relative to the vacuum level is the energy required to remove the electron to infinity with zero kinetic energy. The measured kinetic energy of the emitted electron is thus equal to the x-ray photon energy minus the binding energy of the state from which the electron was emitted. Measurement of the kinetic energy of the emitted electrons will thus, in principle, directly yield the binding energies of the occupied states. In practice, binding energies in XPS are measured relative to the Fermi level, rather than the vacuum level. In this case, the kinetic energy of the emitted electron is equal to the x-ray photon energy minus the sum of the binding energy relative to the Fermi level and the work function of the spectrometer. Each element has a set of energy levels (corresponding to atomic and molecular orbitals) with binding energies characteristic of that element. In a photoelectron intensity vs. binding energy plot, a set of peaks will be observed which correspond to the energy levels of each element in the specimen being irradiated. The relative intensities of the various peaks will

thus be a measure of the chemical composition of the specimen.

The binding energy is actually a measure of the potential around the atom of interest. The same atom in different chemical environments will have a different potential depending on the valence charge distribution. Binding to more electronegative atoms will result in charge transfer to the more electronegative atoms from the atom of interest, decreasing the valence charge density and thus increasing the observed binding energy. The binding energies of the photoelectron peaks are thus not only a measure of the elemental composition of the specimen, but also are a measure of the oxidation states of each of the constituent elements. Differences in binding energies which are due to differences in the chemical environment are termed chemical shifts. Changes in the valence charge distribution can also arise from structural differences, which may also result in observable binding energy shifts. One example of such structure induced charge transfer (SICT) occurs¹⁻³ in the previously mentioned case of SiO_2/Si , in which the structure of the interfacial SiO_2 differs from that of the bulk SiO_2 .

It is to be noted that XPS is a surface sensitive technique, since the photoelectron inelastic mean free path (the path length over which the fraction of photoelectrons which are not inelastically scattered is $1/e$) is typically in the range 5-50 Å, depending upon the material and the kinetic energy of the emitted electron. This surface sensitivity can be exploited to obtain compositional depth profiles. This can be accomplished by varying the photon energy,²⁹ and hence the photoelectron kinetic energy and the mean free path. Alternatively, the electron take-off angle can be varied.³⁰⁻³⁴ In this

work, sequential chemical etching has been used to expose the insulator film at different depths below the initial surface to the vacuum. Details of the etching technique can be found elsewhere.^{1,35} The intensity analysis necessary to obtain a compositional depth profile using this approach was developed¹⁷ as a part of this task, and is a generalization of a previously published technique.³⁶ The intensity analysis is discussed in detail in Appendix A.

In some cases, it is desirable to study the insulator/Si interface from the Si side. Such a situation occurs in device structures which have been metallized, since the metal must be removed uniformly without affecting the insulator film, which is difficult. Another such situation occurs in the study of the buried insulator layer in SOI structures. Finally, verification of the interfacial composition may be required if it is suspected that the chemical etch resulted in preferential etching, yielding results which are artifacts of the etching technique. In all of these cases, an etch of Si which does not affect the insulator film is required. XeF₂ gas-phase etching of Si has been developed^{37,38} as part of this task, and has been used in parts of this work.

While XPS has proven to be a powerful technique for determining chemical compositions, it is not the best technique for all circumstances. Chemical shifts can be small, signals may be weak, and it is difficult to unambiguously determine structural differences from XPS spectra alone. In addition, the surface sensitivity of XPS can be a disadvantage if a bulk property of a material is of interest, or if an interface to be studied is beyond the detection depth of XPS and there is no suitable chemical etch to expose

the interface. In such circumstances, other techniques must be used.

In this work, spectroscopic (wavelength dispersive) ellipsometry has been used in conjunction with XPS. Ellipsometry involves measurement of the polarization state of light reflected from a specimen when the polarization state of the incident light is known. Reviews of the technique and its concepts and applications are available elsewhere,³⁹⁻⁴² so only a brief description of the concepts is presented below. The spectroscopic ellipsometer used in this work is similar to that described by Aspnes and Studna,⁴³ and is described elsewhere.⁴⁴

With the incident and reflected beams defining the plane of incidence, the polarization state of the light can be determined in terms of a component linearly polarized in the plane of incidence (*p*-polarized), and a component linearly polarized perpendicular to the plane of incidence, in the plane of the sample surface (*s*-polarized, from the German *senkrecht* for perpendicular). The ratio of the electric vectors of the reflected and incident beams is defined as the reflection coefficient *R*. The complex ratio of the reflected *p*- and *s*-polarized light components is related to the measured ellipsometric parameters $\tan \psi$ and $\cos \Delta$ via

$$R_p(E)/R_s(E) = \rho(E) \approx \tan \psi(E) \exp[i\Delta(E)], \quad (1.1)$$

where *E* is the photon energy. The material property to which $\rho(E)$ is related is the dielectric function $\epsilon(E)$, which is defined as the permittivity relative to the free space permittivity ϵ_0 .

The region of the sample which contributes to the ellipsometric measurement depends upon how absorbing the sample is at the photon energy used in the measurement. For Si and GaAs, the absorption depth (the distance over which the light intensity is attenuated by a factor of e , analogous to the photoelectron mean free path in XPS) in the visible - ultraviolet energy range can be as low as 50 - 100 Å, as large as thousands of Å near the bandgap, and much larger below the bandgap where the materials are transparent. In its ability to "see" through thick films in an appropriate photon energy range, SE is thus complementary to XPS. However, SE can also be surface sensitive, since reflectivity can be significantly affected by the surface condition of the sample.

Spectroscopic ellipsometry differs from conventional null ellipsometry in its use of variable wavelength light, and its use of a continuously rotating polarizer or analyzer together with Fourier analysis of the time-dependent light intensity at the detector,³⁹⁻⁴⁴ making a compensator unnecessary. The Fourier analysis yields the ellipsometric parameters $\tan \psi$ and $\cos \Delta$. The pseudodielectric function (the measured dielectric function assuming a mathematically abrupt solid-ambient interface), $\langle \epsilon(E) \rangle$, can be calculated from $\rho(E)$ if the sample can be considered as a semi-infinite medium of a single material, rather than a multilayer structure of more than one material. The semi-infinite medium may itself consist of a physical mixture of more than one material, in which case the mixture can be modeled by using an effective medium approximation^{45,46} to calculate the effective dielectric function of the mixture. The composition of the mixture is varied to achieve good agreement

with the data. The fraction of each material in the mixture can thus be obtained numerically. The density of a material is a bulk physical property which can be obtained by modeling the material as the same material in some known standard state with an admixture of voids.

Spectroscopic ellipsometric data obtained from multilayer structures is analyzed in a manner similar to that discussed above, though the relevant equations are complicated by interference between light reflected from the different interfaces in the multilayer structure, and by multiple internal reflections within each layer. Physical properties which can be obtained using multilayer analysis include the degree of surface roughness (by modeling the surface as a layer consisting of a physical mixture of the underlying material and voids), interfacial roughness (by modeling the interface as a layer consisting of a physical mixture of the materials on either side of the interface), and the film thickness and composition.

In the discussion above, the use of SE to determine physical properties of materials, *i. e.* properties which would be considered as structure-related in the context of the earlier discussion, has been briefly considered. Chemical information can also be obtained using SE. For example, the chemical composition of the SiO_2/Si interface has been measured⁴⁷ using calculated values⁴⁸ of the dielectric function of SiO_x . However, SE has most commonly been used, and is best suited, for the determination of structure-related properties of materials, and is in this respect complementary to XPS.

The remainder of this report is organized as follows. Studies of metal-nitride-oxide-semiconductor structures are described in Chapter 2, studies of

$\text{SiO}_x\text{N}_y/\text{Si}$ formed by the thermal nitridation of SiO_2/Si are discussed in Chapter 3, and studies of semiconductor-on-insulator structures are described in Chapter 4. The conclusions are contained in Chapter 5, followed by the bibliography and appendix.

Chapter 2

Studies of Metal-Nitride-Oxide-Semiconductor (MNOS) Structures

As previously mentioned, the study of CVD Si_3N_4 and its interface with SiO_2 in MNOS structures was the primary work of the previous task, and the results are described elsewhere.⁴⁻⁹ Some follow-on work has been done in this task, concerning the effects of H_2 annealing on the Si_3N_4 and the $\text{Si}_3\text{N}_4/\text{SiO}_2$ interface, and the results are described herein.

Two samples were obtained from Westinghouse which consisted of approximately 450 Å of Si_3N_4 deposited on Si wafers which had native oxides. One wafer was annealed in H_2 , while the other was used as a control and was not annealed. Both wafers were then metallized with Al to form the MNOS structure and shipped to JPL. The metallized surface was bonded to a Au platen with In and the Si wafer was etched away with XeF_2 gas, a technique described elsewhere.^{37,38} Briefly, XeF_2 reacts spontaneously with Si to form Xe and SiF_4 , but does not react with SiO_2 or Si_3N_4 unless activated with a beam of electrons, ions, or UV photons. XeF_2 is a solid which has a room temperature vapor pressure of 4.5 torr. Since the reaction products of XeF_2 with Si are gases, a simple vacuum system with a valve to separate the XeF_2 holding chamber and the sample chamber can be used to accomplish the etching. Figure 2.1 shows a schematic diagram of the XeF_2 etching system used in this work. Using this technique, the native SiO_2/Si interface was exposed. XPS spectra were recorded, then both samples were

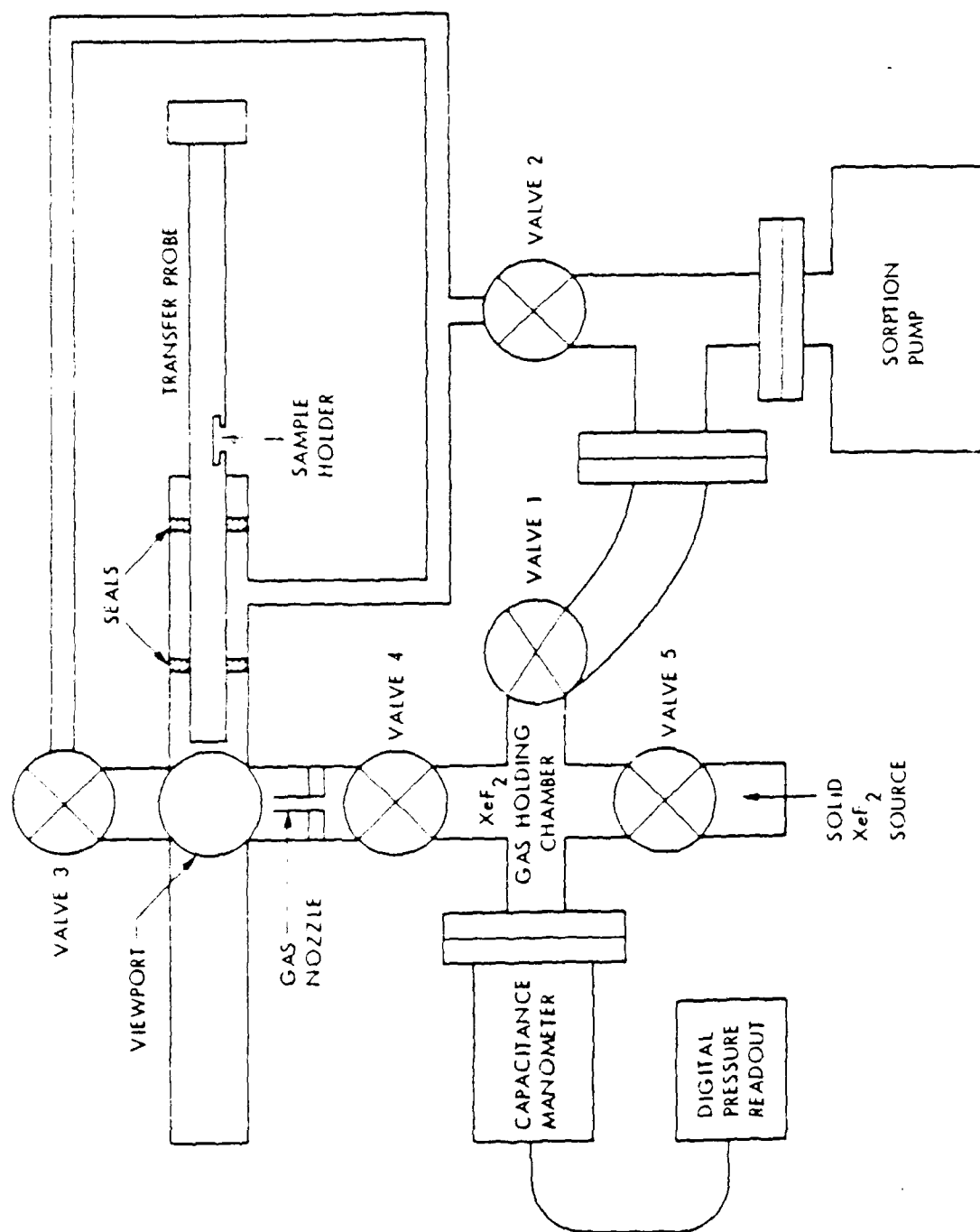


Figure 2.1 Schematic diagram of the system used for gas phase XeF_2 etching of Si.

etched with 1:10 HF:EtOH to expose the $\text{SiO}_2/\text{Si}_3\text{N}_4$ interface and XPS spectra were again accumulated.

Prior to the HF:EtOH etch, the Si 2p spectra from both samples showed two distinct peaks separated by 1.5 eV, the same separation as that observed¹³ between SiO_2 and Si_3N_4 . In addition, the energy separation between the Si 2p peak at higher energy and the O 1s peak is 429.7 eV, which is within experimental error of the 429.6 eV expected¹ for SiO_2 . This confirms that some SiO_2 remains intact at the SiO_2/Si interface after the Si_3N_4 deposition, as previously reported^{7,9} from studies of samples which had been depth profiled from the front side. The earlier findings^{7,9} are thus not due to possible artifacts of the etching technique. In this work, it was found that the two samples had native oxides which were somewhat different in thickness, with the H_2 -annealed sample having a thinner native oxide (17 Å vs. 20 Å for the control sample). These thicknesses were estimated by assuming a 30 Å photoelectron mean free path in both SiO_2 and Si_3N_4 and using intensity analysis as described in Appendix A and elsewhere.^{17,36}

After the HF:EtOH etch, the Si 2p spectra from the two samples showed substantial differences. The H_2 -annealed sample again showed two peaks with the energy separation reduced to 1.2 eV, indicative of an oxynitride.¹³ Only one Si 2p peak was apparent for the control sample, but Fourier analysis⁴⁹ suggested the presence of two peaks with a broader lineshape and wider energy separation than was observed for the H_2 -annealed sample.

The data can be explained in the following manner. The H_2 forms Si-OH groups in the oxide and Si-NH₂ in the nitride in a manner similar to that

proposed¹⁸ for the thermal nitridation of SiO_2 . The hydroxyl and amino groups are mobile at high temperature, resulting in interdiffusion at the $\text{SiO}_2/\text{Si}_3\text{N}_4$ interface with subsequent oxynitride formation. This explains the lower energy separation between the two Si 2p peaks after H_2 annealing. The narrower lineshape observed after H_2 annealing may be a result of strain relaxation. As previously reported,¹⁻³ strain near the SiO_2/Si interface results in a different distribution of Si-O-Si bond angles than that which occurs in bulk SiO_2 , with an accompanying charge transfer which shifts the binding energy of the Si 2p peak. Since different bond angles result in different binding energies, the effect is an apparent broadening in the Si 2p lineshape. The breaking of strained Si-O-Si bonds by the H_2 to form Si-OH would be expected to relieve the strain and allow the unbroken Si-O-Si to relax closer to the 144° bond angle which is predominant in bulk SiO_2 . The reduction in the number of Si-O-Si bond angles with higher and lower values than 144° would thus be expected to narrow the Si 2p lineshape.

In summary, the effect of H_2 annealing appears to be to make the $\text{Si}_3\text{N}_4/\text{SiO}_2$ interface less abrupt by causing interdiffusion of silanol and silamine groups and subsequent oxynitride formation, and also to relieve strain at the SiO_2/Si interface.

Chapter 3

Studies of $\text{SiO}_x\text{N}_y/\text{Si}$ Formed by the Thermal Nitridation of SiO_2/Si

I. Kinetics of Nitridation: Background

SiO_2 films on Si have been extensively studied¹⁻³ and are known to be chemically homogeneous. The reaction of SiO_2 with NH_3 results in the formation of an oxynitride. This material may have chemical inhomogeneities, and the fact that the properties of the initial SiO_2 film are well understood may make it possible to gain a detailed understanding of the formation of these inhomogeneities by studying and modeling the kinetics of nitridation.

Silicon oxynitride (SiO_xN_y), formed by the thermal nitridation in NH_3 of SiO_2 films on Si, is a promising dielectric⁵⁰⁻⁵⁸ for such applications as very large scale integration (VLSI), floating gate electrically erasable programmable read-only memory (EEPROM) devices, and radiation hard devices. The thin gate or tunnel insulators required for VLSI and floating gate EEPROM devices can be a source of serious problems if the insulator is the conventional thermally grown SiO_2 . These problems include⁵⁰⁻⁵⁸ low resistance to dopant and impurity diffusion, high electric field instabilities, hot electron effects, radiation effects, and slow trapping. SiO_xN_y is in many ways superior to SiO_2 in the applications mentioned above. Specifically, it has been shown⁵⁰⁻⁵⁸ that thermally nitrified SiO_2 has an increased resistance to high field instability, forms a better diffusion barrier, is less reactive to gate electrodes, is oxidation resistant, reduces degradation due to carrier injection,

and nearly eliminates formation of ionizing radiation-induced interface states. Si_3N_4 exhibits many of these same advantages. Direct thermal nitridation of Si has been shown to be possible, but the thickness of the Si_3N_4 film is self-limited⁵⁹ at about 30 Å. In addition, deposited Si_3N_4 has been utilized in MNOS (metal-nitride-oxide-semiconductor) structures. However, this dual dielectric structure exhibits⁵³ high trapping efficiency in the nitride and at the nitride/oxide interface, making it unsuitable for some applications. Thermally nitrided SiO_2 has the advantages of not having the dielectric/dielectric interface of MNOS structures, and the thickness is determined by the initial oxide thickness.

The potential use of SiO_xN_y in technologically important device applications has prompted several studies^{10-18,50-53,60-69} of the chemical structure of SiO_2 films which have been thermally nitrided in NH_3 . Early studies^{50-53,60-65} were done for varying nitridation conditions, which (not surprisingly) resulted in reported N distributions which differed from study to study. There was general agreement that the nitrogen concentration in the films is higher at the surface^{50-52,63-65} and near the $\text{SiO}_x\text{N}_y/\text{Si}$ interface^{62,64,65} than in the bulk of the oxynitride film, although two studies^{50,63} found direct evidence only for the higher surface nitrogen concentration, and one study⁶⁰ found the nitrogen distributed uniformly throughout the film. Recently, it was reported¹³ that the peak in the interfacial nitrogen concentration can occur away from the $\text{SiO}_x\text{N}_y/\text{Si}$ interface itself.

Some of the differences noted above may be explainable by the different sensitivities of the techniques employed, since the AES sputter depth profiling typically employed is known to broaden the interface, and thus resolution of

possible differences in N distributions in the critical interfacial region is difficult. However, some of the differences are almost surely related to the kinetics of the nitridation process and differences in nitridation conditions. The findings discussed above have prompted several recent studies^{14-18,67-69} of the kinetics of the nitridation process. The work¹⁰⁻¹⁸ described in detail in this chapter, together with work⁶⁷⁻⁶⁹ done independently and in parallel at Stanford, represents the first comprehensive attempt to determine the dependence of the N distribution on nitridation time and temperature. In addition, this work¹⁰⁻¹⁸ is the first to use a technique, high resolution XPS in conjunction with relatively benign chemical etching, which is capable of a detailed study of the interfacial nitrogen distribution. The reliable determination of the interfacial nitrogen distributions has allowed, for the first time, a detailed picture of the mechanism and kinetics of the nitridation process to be proposed and computer simulations¹⁸ of the nitridation kinetics carried out as part of this work. The kinetic modeling also shows that the role of interfacial strain, discussed in detail below and in section IV, must be taken into account to explain the observed interfacial nitrogen distributions.

The dependence of electrical characteristics on the nitridation conditions has also been reported in the literature, as described in detail below and in section III.B. Thus, as a further check of our proposed model for the kinetics of nitridation we have examined these data and shown, for the first time, a correlation with the nitrogen distributions observed in this work. This correlation is explained within a model¹⁵ in which the defect formation kinetics are postulated to be strain-dependent, and correlated to the strain dependent kinetics of the nitridation process itself. This work thus presents

the first comprehensive explanation of the interdependence of the processing conditions, electrical characteristics, and chemical structure of nitrated oxides within a framework which takes into account known properties of the initial SiO_2 film.

Of the electrical studies alluded to in the preceding paragraph, one study⁵² reported that the interface fixed charge density correlates with the amount of nitrogen at the interface, while another reported⁵³ that the magnitude of the flatband voltage shift $|\Delta V_{\text{FB}}|$ -- typically interpreted as a measure of the fixed charge in the dielectric -- is reduced by the presence of nitrogen at the interface. A more recent report⁵⁷ showed that for a nitridation temperature of 900°C , $|\Delta V_{\text{FB}}|$ increases monotonically with increasing nitridation time, but for a nitridation temperature of 950°C , $|\Delta V_{\text{FB}}|$ initially increases, then decreases with increasing nitridation time.⁵⁷ At nitridation temperatures $\geq 1000^\circ\text{C}$, $|\Delta V_{\text{FB}}|$ decreases monotonically⁵⁷ for nitridation times beyond 30 minutes. Similar observations on the behavior of $|\Delta V_{\text{FB}}|$ have been made by other researchers.⁷⁰

Chen *et al.* suggested⁵⁷ that the lower values of $|\Delta V_{\text{FB}}|$ for $\text{SiO}_x\text{N}_y/\text{Si}$ formed at high nitridation temperatures ($> 1000^\circ\text{C}$) may be due to a small solubility of hydrogen -- which was postulated to be involved in the formation of defects -- at elevated temperatures. However, the solubility of H_2 in fused silica is nearly independent of temperature.⁷¹ The hydrogen may also be in the form of H_2O , which reacts with SiO_2 to form Si-OH bonds, but the solubility of H_2O , and hence the concentration of Si-OH bonds, in fused silica is also not a strong function of temperature.^{72,73} One may thus conjecture that the same holds true for the solubility of NH_3 in SiO_2 . It is more likely that the

formation of the defects giving rise to $|\Delta V_{FB}|$ is related to the nitridation kinetics. In this work,¹⁵ a correlation between the nitrogen distribution and the behavior of $|\Delta V_{FB}|$ will be identified and an explanation will be proposed.

In order to understand the underlying reasons for the measured nitrogen distributions, we have developed¹⁸ a kinetic model which simulates the nitridation process. In any attempt to model the nitridation kinetics, the initial structure of the SiO_2 film must first be understood. In particular, the possibility that strain in the SiO_2 film affects the nitridation kinetics must be considered. It is known that, upon oxidation of Si to form SiO_2 , a large molar volume change produces compressive stress in the oxide in the plane of the Si surface, which relaxes by viscous flow in the growth direction.^{74,75} At oxidation temperatures below 950°C, the relaxation rate is slower than the oxidation rate,⁷⁴ resulting in a buildup of intrinsic stress in the oxide and denser oxides at low oxidation temperatures. This temperature will be referred to as the viscous flow temperature T_v . The stress and densification in the oxide at low growth temperatures may affect the nitridation kinetics. This first type of strain is macroscopic in nature, affecting the entire oxide film.

Another source of strain is the lattice mismatch between the Si and the SiO_2 , and is localized within 30 Å of the SiO_2/Si interface.¹⁻³ This interfacial strain is present even in high temperature oxides^{1-3,36,76,77} which do not exhibit macroscopic stress.⁷⁴ This strained interfacial region is characterized by a higher proportion of 4-membered rings (4 Si tetrahedra with bridging oxygens in a ring structure) compared to the unstrained bulk SiO_2 , which consists primarily of 6-membered rings. The effects of the strain would not be expected to be confined to the SiO_2 side of the interface, but would extend a

few Å into the Si substrate as well. Interfacial strain has been invoked to explain⁷⁸ the observed U-shaped density of states in the Si band gap at the Si/SiO₂ interface, and in general in lattice mismatched systems, and to explain the generation^{76,79,80} and diffusion⁷⁷ of defects in electron-irradiated SiO₂/Si. It will be shown that the measured nitrogen distributions are consistent with the kinetic model provided the influence of the interfacial strain on the nitridation kinetics is explicitly accounted for.

The overall objective of this work¹⁰⁻¹⁸ has been to determine the kinetics and mechanism of the nitridation process. These studies have utilized high resolution XPS in conjunction with nondestructive chemical depth profiling^{13,14,16,17} to measure nitrogen distributions, kinetic simulations of the nitridation process^{14,16-18} to understand the factors giving rise to the measured nitrogen distributions, and spectroscopic ellipsometry for possible complementary information. XPS is not well suited for determining physical properties such as void fractions, interfacial roughness, or lateral nonuniformities. Spectroscopic ellipsometry can, in principle, provide information on these physical properties. Together, these techniques give insight into how processing conditions affect the chemical composition of the nitrided oxides, and provide a basic understanding of the nitridation process and the role of strain in the nitridation kinetics. In addition to determining chemical compositions, defect distributions have also been deduced, both by correlating¹⁵ chemical compositions with electrical characteristics, and through use^{16,17} of a fluorine marker, which is postulated to bind to defect sites. Some understanding of the relationship between processing conditions, chemical composition, and electrical characteristics can thus be

obtained.

The experimental conditions will be described in Section II. The XPS measurements will be described in Section III, with the measured nitrogen distributions in nitrided oxides presented in Section III.A and the defect distributions deduced from electrical and chemical data presented in Section III.B, together with a model to explain the electrical data. Section IV contains the kinetic simulations, with the nitridation process described in Section IV.A, the kinetic model presented in Section IV.B, the choice of kinetic parameters described in Section IV.C, and the simulation results presented in Section IV.D. The spectroscopic ellipsometry results will be described in Section V, and Section VI contains the summary and conclusions.

II. Experimental

Si (100) wafers were thermally oxidized in dry O₂ to a thickness of approximately 100 Å, then heated in pure NH₃ at atmospheric pressure. Oxidation temperatures, nitridation temperatures, and nitridation times are shown in Table I. The XPS spectrometer used in this work is a modified HP5950A¹ utilizing monochromatized AlK_α x-rays (1486.6 eV). The sample introduction area of the spectrometer is enclosed by a dry box in which an N₂ ambient is maintained in order to prevent exposure of the sample to atmospheric oxygen and water vapor after it has been etched. The samples were sequentially chemically etched in the dry box with 1:10 HF:EtOH dispensed with a microliter pipette onto a sample spinning at 3600 rpm. The EtOH used was U.S.P. punctilious grade ethanol. Details of the etching technique and its advantages have been discussed elsewhere.^{1,35} This

Table I. Summary of the oxidation and nitridation conditions for the samples used in this work.

Sample #	Initial Oxide Thickness (Å)	Oxidation Temperature (°C)	Nitridation Temperature (°C)	Nitridation Time (min)
1	100	1000	1000	10
2	100	1000	1000	30
3	100	1000	1000	120
4	100	825	1000	240
5	100	1000	1150	5
6	100	1000	1150	10
7	100	825	800	60
8	100	1000	800	60
9	100	1000	800	240
10	1030	1000	800	60
11	1030	1000	1000	60

chemical depth profiling technique preserves chemical and structural information which would be lost¹ if ion sputtering techniques were employed.

The base pressure of the analysis chamber was $2-3 \times 10^{-10}$ Torr during accumulation of spectra. After each etch step, XPS spectra were recorded and the Si 2p, O 1s, N 1s, and F 1s photoelectron peak intensities were measured by fitting Voigt profiles (convolution of a Lorentzian function representing core hole lifetime broadening and a Gaussian function representing instrumental and other broadening mechanisms)⁴⁹ to the peaks and correcting the intensities using Scofield's calculated photoionization cross sections.⁸¹ These intensities were used to calculate the relative nitrogen concentration $[N]/([O]+[N])$ by the technique described in Appendix A. Using this technique, the actual film composition as a function of depth is obtained, unbiased by the averaging effect of the relatively long photoelectron mean free path.

III. XPS Measurements

The nitrogen distribution measured in nitrided oxides will be described in section III.A. In section III.B, the defect distributions deduced from electrical and chemical data are presented and correlated to the observed nitrogen distributions. A model is proposed to explain the correlation between the electrical data and nitrogen distributions.

III. A. Nitrogen Distributions

Figure 3.1 shows the N 1s and O 1s photoelectron peak intensities, I_{N1s} and I_{O1s} , for sample 1, which has been nitrided at 1000°C for 10 minutes. The

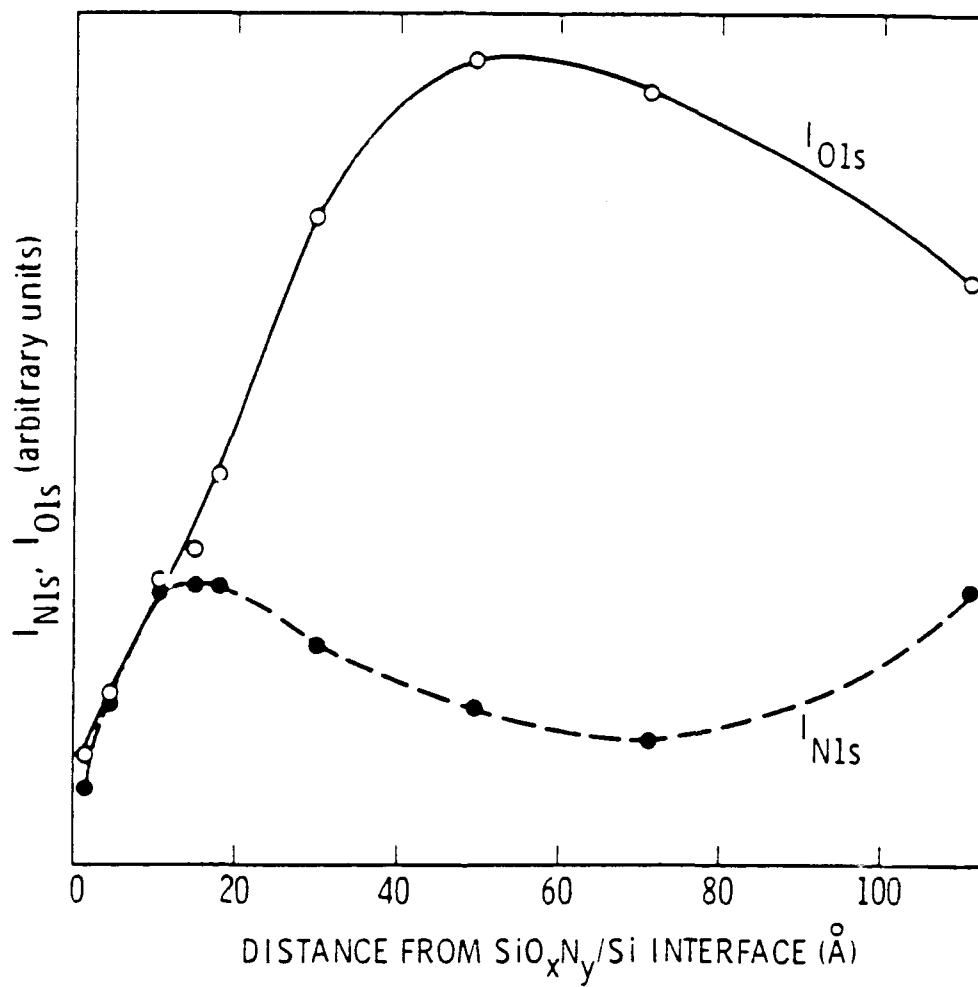


Figure 3.1. N 1s and O 1s photoelectron peak intensities, I_{N1s} and I_{O1s} , measured during the course of depth profiling sample 1, corrected for photoionization cross section differences.

intensities have been corrected for the different photoionization cross sections.⁸¹ The inhomogeneous nitrogen distribution in the nitrated oxide is clearly evident, with the nitrogen signal high relative to the oxygen signal in the surface and interfacial regions. This is consistent with the earliest studies^{50-52,63-65} of the distribution of nitrogen in nitrated oxides. With increased nitridation time, however, I_{N1s} decreases faster than I_{O1s} in the region closest to the interface. This is consistent with a later report¹³ that the peak interfacial nitrogen concentration occurs approximately 20 Å away from the interface. These trends are more apparent when the ratio $I_{N1s}/(I_{O1s} + I_{N1s})$ is plotted, as shown in Fig. 3.2. However, this is not a measure of the actual nitrogen distribution in the film, since a correction for the difference in the mean free paths of N 1s and O 1s photoelectrons (due to the different kinetic energies) has not been included. In addition, the averaging effect of the relatively long mean free paths has not been considered. These corrections have been made using the technique described in Appendix A for the data shown in Fig. 3.3, which shows the nitrogen distributions for samples 1, 2, and 3. For all three samples, the oxidation and nitridation temperatures are both 1000°C, and the nitridation times range from 10 to 120 minutes.

For a nitridation temperature of 1000°C, the nitridation time dependence of the nitrogen distribution can be summarized as follows. Nitrogen initially incorporates rapidly at the interface until a saturation concentration is reached, as seen in Fig. 3.3(a). As the nitridation proceeds, the surface nitrogen concentration also saturates, nitrogen incorporation continues in the bulk of the film, and the interfacial nitrogen peak occurs away from the interface, as seen in Fig. 3.3(b). With increasing nitridation time, nitrogen

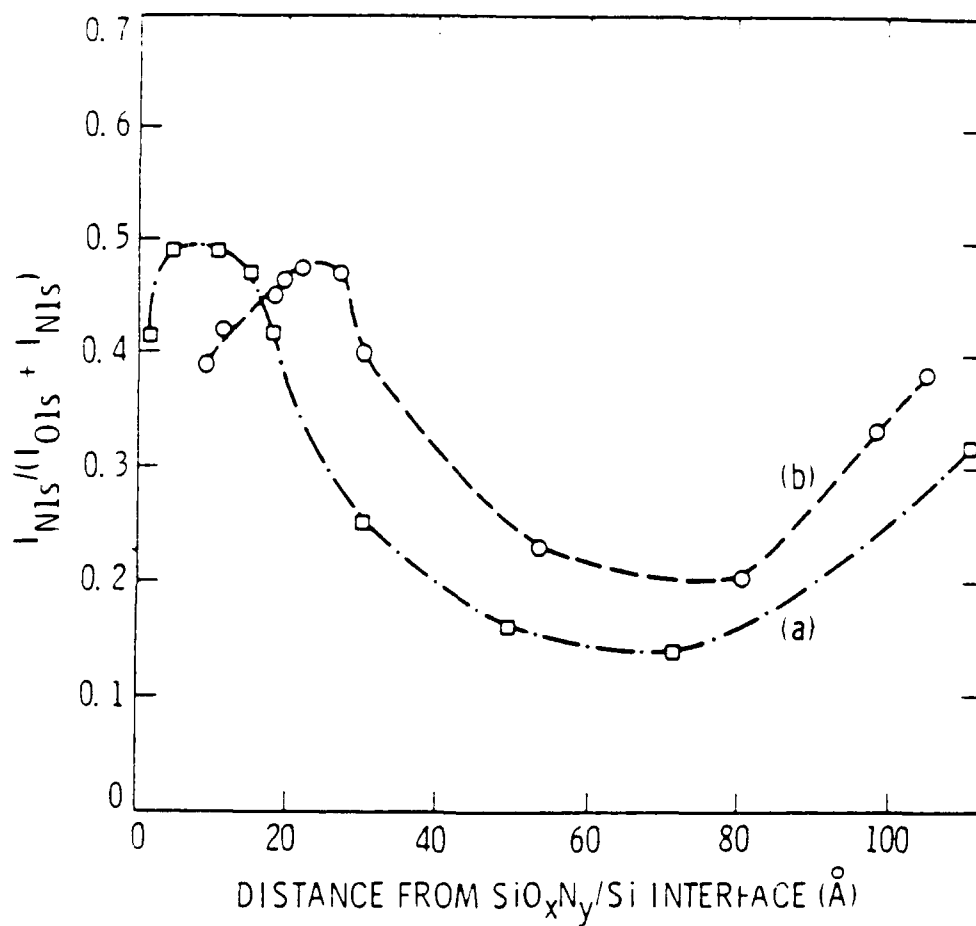


Figure 3.2. $I_{N1s}/(I_{O1s} + I_{N1s})$ for (a) sample 1, and (b) sample 2, corrected for photoionization cross section differences.

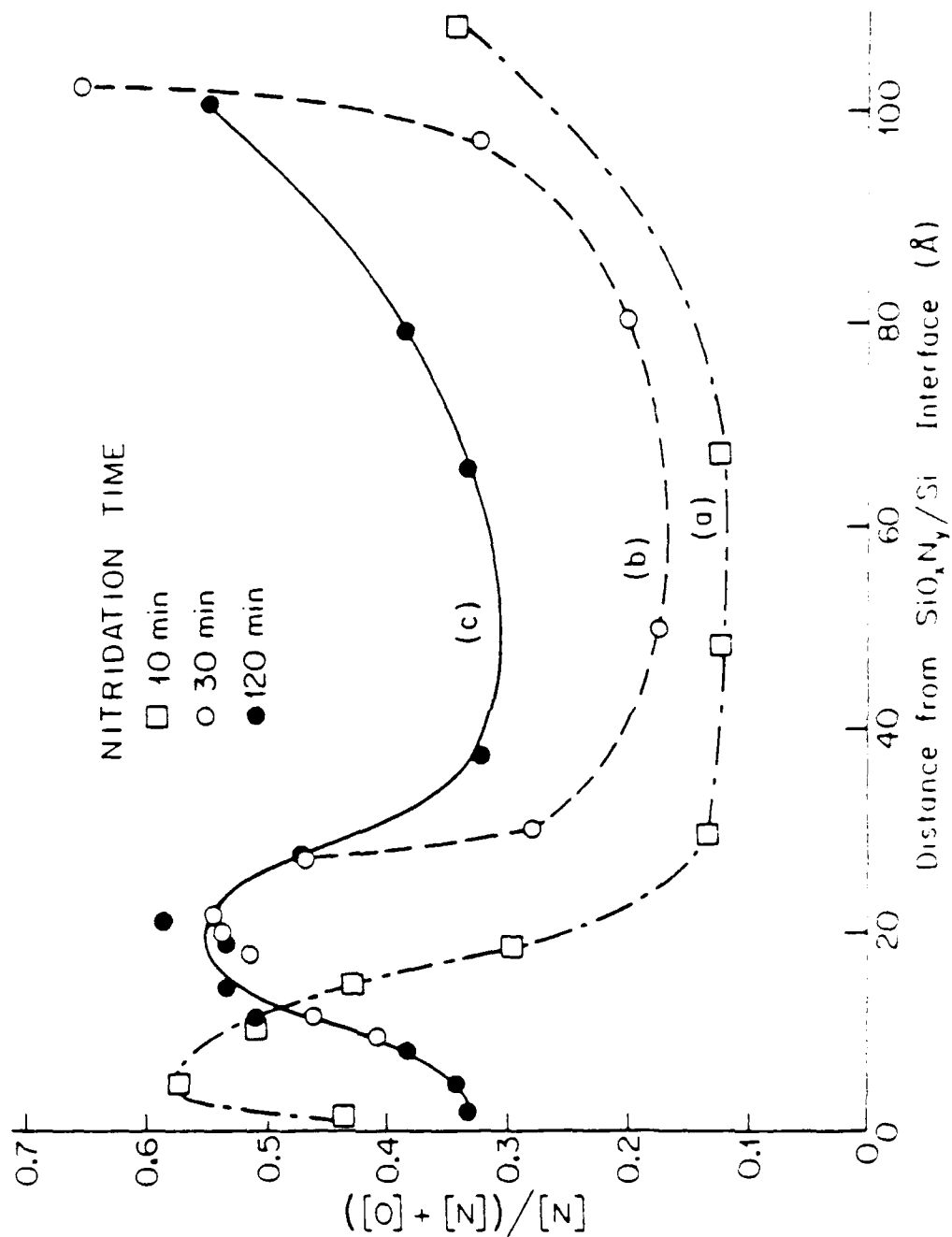


Figure 3.3. Distribution of N in SiO_xN_y produced from a 100 Å-thick SiO_2 film grown in dry O_2 at 1000°C, then nitrided at 1000°C for (a) 10 minutes, (b) 30 minutes, (c) 120 minutes.

incorporation continues in the bulk of the dielectric, as seen in Fig. 3.3(c) and in the data from sample 4, which has been previously reported.¹³ Qualitatively similar results have been reported⁶⁷⁻⁶⁹ for 400-Å-thick oxides nitrated at 1100°C. Quantitative differences can be attributed to the different initial oxide thickness and higher nitridation temperature used in that work.⁵⁷⁻⁶⁹

Figure 3.4 shows the nitrogen distribution in samples 5 and 6, which have been nitrated at 1150°C. Figures 3.4(a) and 3.4(b) are similar to Figures 3.3(b) and 3.3(c), except the peak interfacial nitrogen concentration has saturated at a lower value, although it occurs essentially the same distance from the interface. The ratio $[N]/([O] + [N])$ is seen to have a maximum value near 0.55 in the interfacial region for a nitridation temperature of 1000°C, and near 0.45 for a nitridation temperature of 1150°C. The decreased nitrogen incorporation in the interfacial region at elevated temperatures may partially explain the failure to observe⁵⁰ an interfacial nitrogen buildup for a 500 Å thick oxide nitrated at 1200°C.

Figure 3.5 shows the nitrogen distributions in samples 7, 8, and 9, which have been nitrated at 800°C. Samples 7 and 8 differ only in the oxidation temperature. The purpose of this comparison is to determine the effect of macroscopic intrinsic stress on the nitridation kinetics. The one hour nitridation time for samples 7 and 8 is insufficient⁷⁴ for the macroscopic stress to relax by viscous flow at the nitridation temperature of 800°C, so the low temperature oxide would retain the stress acquired during oxidation. It can be seen in Fig. 3.5(a), however, that the nitridation has not been affected by the oxidation temperature. This may be because the effect of macroscopic

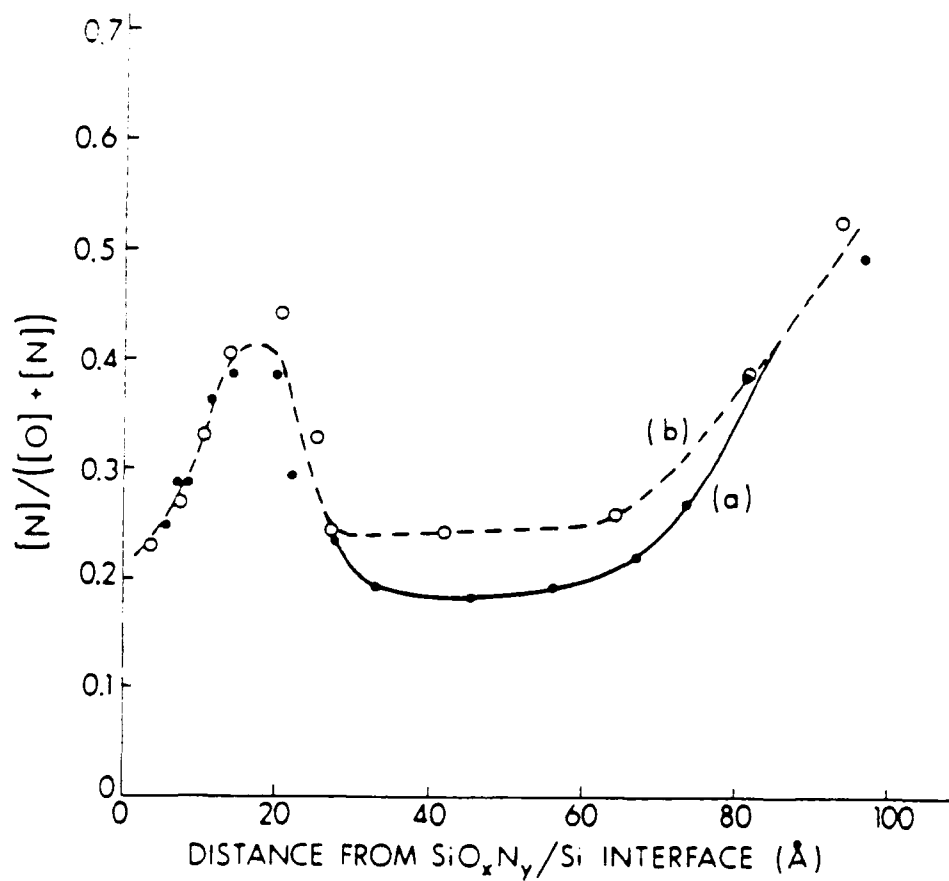


Figure 3.4. Distribution of N in SiO_xN_y produced by nitriding a 100 Å-thick SiO_2 film at 1150°C for (a) 5 minutes, and (b) 10 minutes.

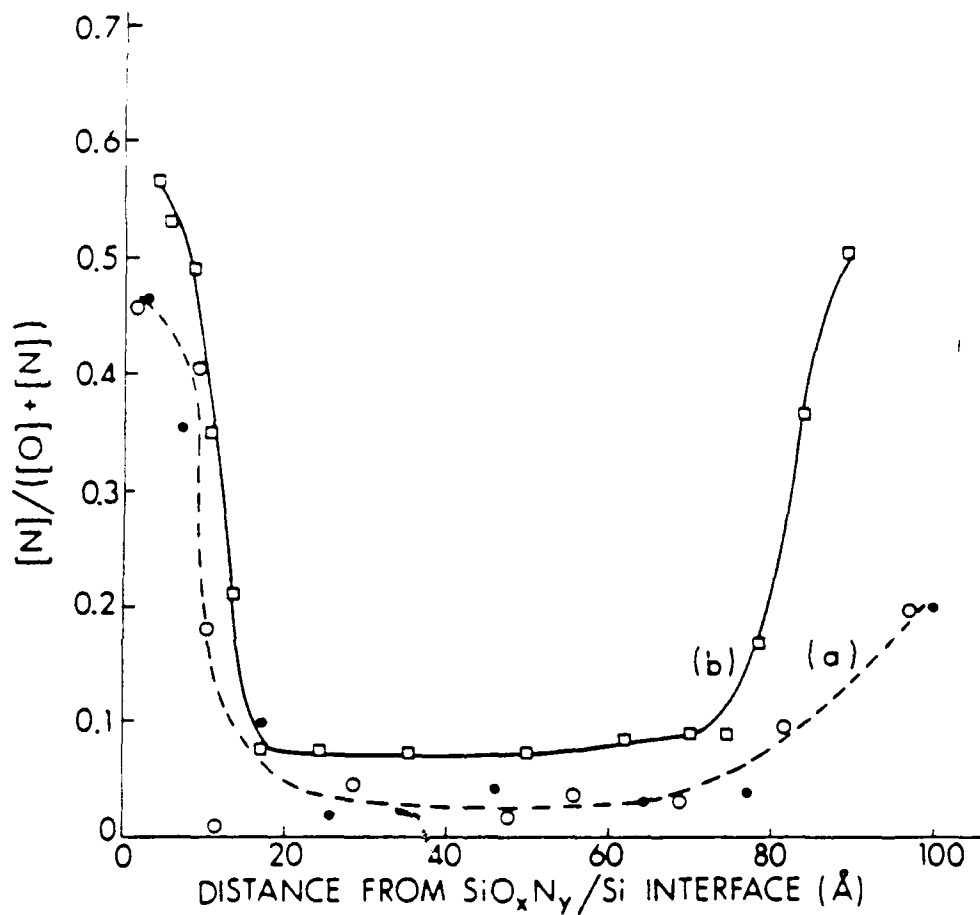


Figure 3.5. (a) Comparison of the distribution of N in SiO_xN_y films produced from 100 Å-thick SiO_2 films grown in dry O_2 at 825°C (solid circles) and 1000°C (open circles), then nitrided at 800°C for 60 minutes. (b) Distribution of N in a SiO_xN_y film produced from a 100 Å-thick SiO_2 film nitrided at 800°C for 240 minutes.

stress on the nitridation is too small to measure, or because the low temperature oxide has relaxed faster than expected due to the formation of Si-OH and Si-NH_x in the oxynitride. It has previously been reported⁷⁴ that relaxation is faster in a H₂O-containing ambient, which reacts with SiO₂ to form silanol groups. The formation of amino groups may also cause accelerated relaxation.

Figure 3.5(b) shows that, for a nitridation temperature of 800°C, the peak interfacial nitrogen concentration does not appear to move away from the interface with increasing nitridation time, as is the case for higher nitridation temperatures. Different nitridation kinetics may become dominant at low nitridation temperatures, even though the oxidation temperature, and hence the macroscopic intrinsic stress, does not appear to affect the nitridation kinetics which determine the nitrogen distribution. The fact that the peak interfacial nitrogen concentration is observed at the interface itself is an indication that the oxygen-rich oxynitride observed at the interface for higher nitridation temperatures is not an etching artifact (*e. g.* resulting from preferential etching or hydroxylation of the surface of the oxynitride by the etchant). This was previously confirmed by the use of XeF₂ gas phase etching of Si to remove the substrate and expose the interface,¹³ and by the observation of the relatively oxygen-rich interface when ion beam etching is used.⁶⁷⁻⁶⁹

III. B. Defect Distributions

Figure 3.6 shows the nitridation time (t_N) dependence of $|\Delta V_{FB}|$, the peak interfacial nitrogen concentration $[N]_p$, and the distance d_{Np} of $[N]_p$ from the

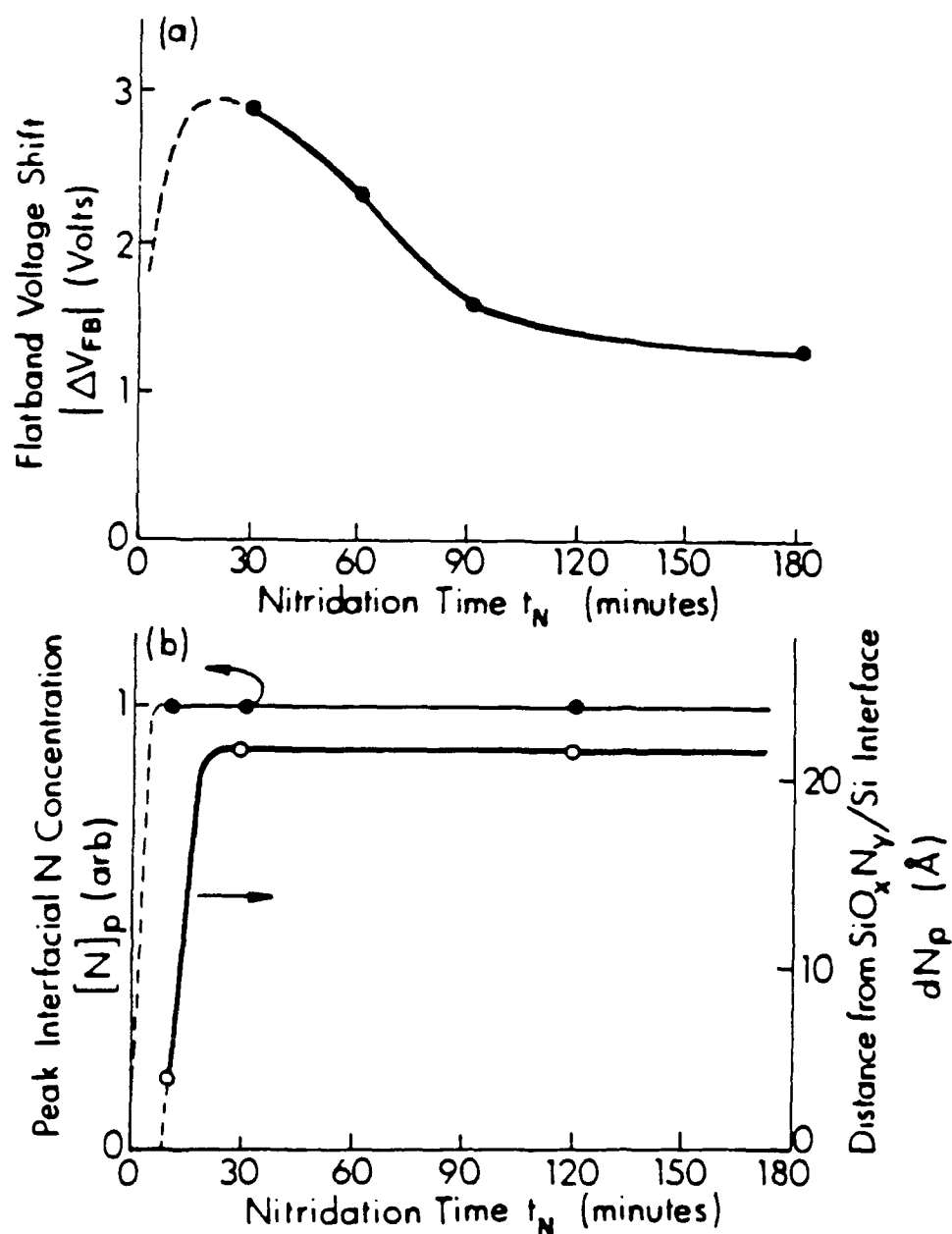


Figure 3.6. (a) Magnitude of the flatband voltage shift $|\Delta V_{FB}|$ as a function of nitridation time t_N , for 600-Å-thick oxides nitrided at 1000°C (from Ref. 57). (b) Peak interfacial nitrogen concentration $[N]_p$ and distance of $[N]_p$ from the interface as functions of t_N , for a 100-Å-thick oxide nitrided at 1000°C (from Fig. 3.3).

interface. Figure 3.6(a) is based on the data⁵⁷ of Chen *et al.*, taken on 600-Å-thick oxides nitrided at 1000°C. Unfortunately, $|\Delta V_{FB}|$ was not measured⁵⁷ for $t_N < 30$ minutes, so that the data does not show the initial increase in $|\Delta V_{FB}|$, as is observed for nitridation temperatures (T_N) below 1000°C. The dashed line in Fig. 3.6(a) for $t_N < 30$ minutes is the expected behavior of $|\Delta V_{FB}|$, based on the initial increase in $|\Delta V_{FB}|$ observed⁵⁷ for $T_N < 1000^\circ\text{C}$. The time scale on which $|\Delta V_{FB}|$ increases is, however, expected to be shorter than is observed for $T_N < 1000^\circ\text{C}$ due to faster reaction rates at elevated temperatures. Figure 3.6(b) is based on the data presented in section III.A on 100-Å-thick oxides nitrided at 1000°C. Qualitatively similar behavior is observed⁶⁷⁻⁶⁹ on 400-Å-thick oxides nitrided at 1100°C. Since the data represented in Figs. 3.6(a) and 3.6(b) were taken on samples with different initial oxide thicknesses, only a comparison of the qualitative trends is useful. In the initial stages of nitridation, $[N]_p$ increases rapidly to some limiting value, and $|\Delta V_{FB}|$ increases. As t_N increases, $[N]_p$ remains nearly constant, d_{Np} increases, and $|\Delta V_{FB}|$ increases until, after some value of d_{Np} , $|\Delta V_{FB}|$ begins to decrease. A clear correlation between the nitrogen distribution and $|\Delta V_{FB}|$ is seen to exist.

It is postulated that the defects giving rise to the charge density responsible for $|\Delta V_{FB}|$ have a spatial distribution which is correlated to, though not the same as, the nitrogen distribution. It is to be noted that the band bending represented by $|\Delta V_{FB}|$ depends on the spatial distribution of the charge within the oxide. The oxide charge induces an image charge in the substrate, and the image potential, which is inversely proportional to the charge separation, causes the band bending. Thus, a decrease in $|\Delta V_{FB}|$,

which is a measure of the band bending, could be caused either by a decrease in the total charged defect density or by an increase in charge separation.

The proposed correlation between the charged defect distribution responsible for $|\Delta V_{FB}|$ and the observed nitrogen distribution may be recognized to occur as follows. As the substrate reacts with the diffusing species, the energy of the system is lowered by the formation of bonds between Si and N or O. The presence of strain at the SiO_2/Si interface, however, partially offsets the gain in energy due to bond formation. This strain energy cost can be lowered if defects which relieve the strain locally are formed during the nitridation process. The ability to lower the system energy via such defects thus suggests that the free energy of defect formation (ΔG_F) behaves as shown schematically in the inset in Fig. 3.7. The result would be an increase in defect concentration at the interface as $[N]_p$ increases in the initial stages of nitridation. As the nitridation proceeds and d_{NO} increases by virtue of the movement of the $\text{SiO}_x\text{N}_y/\text{Si}$ interface, the defects initially formed are left progressively farther from the interface. A schematic representation of this model is shown in Fig. 3.7. The strain energy released via defect formation is then expected to decrease as a result of two different effects: (a) the decrease in strain with increasing distance from the interface^{76,77} and (b) the increasing incorporation of nitrogen in the film. The significance of (b) may be recognized by noting that chemical vapor deposited Si_3N_4 films on Si are known to be in macroscopic intrinsic tensile stress.⁸² Thus, increasing incorporation of nitrogen in the SiO_2 film may counter the compressive stress which is present near the SiO_2/Si interface

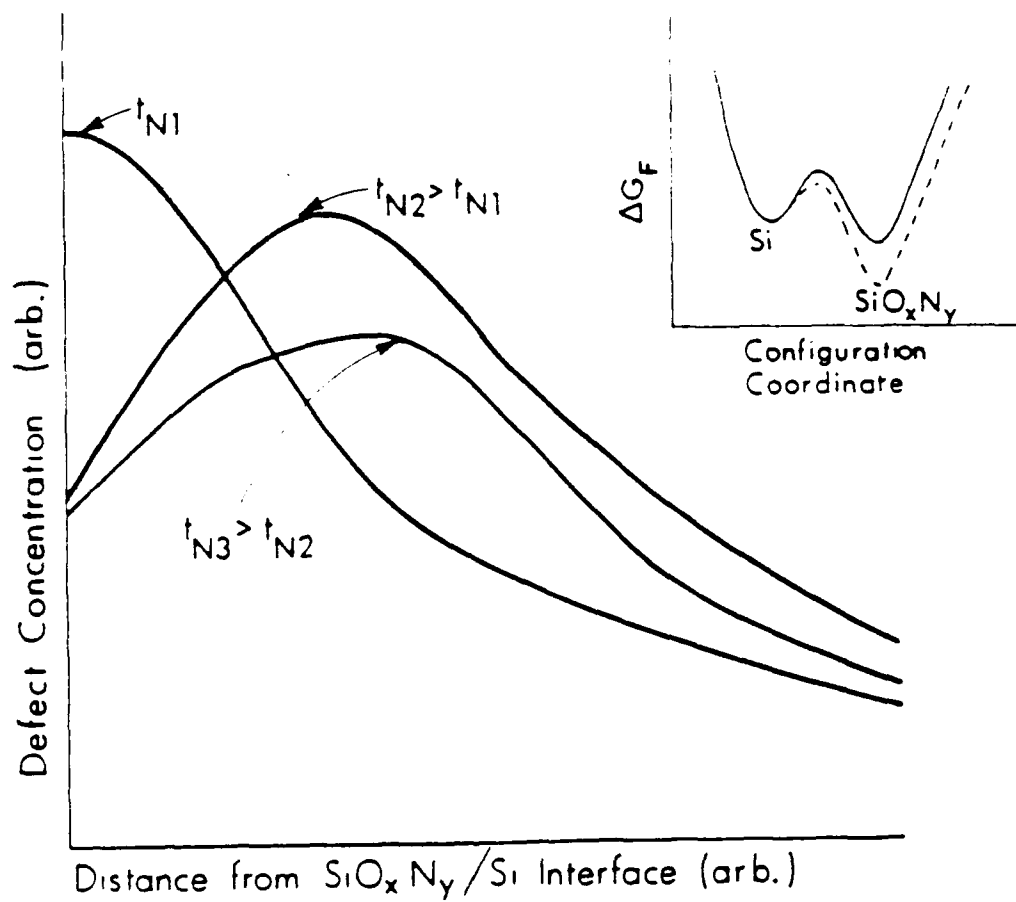


Figure 3.7. Schematic representation of the distribution of defects at various nitridation times. Inset: Schematic diagram of the free energy of formation ΔG_F vs. configuration coordinate for the formation of $\text{SiO}_x\text{N}_y/\text{Si}$ without defects (solid line) and with defects (dashed line) to relieve strain energy.

prior to nitridation. A decrease in the strain implies that the generation of defects is no longer as important for releasing strain energy, and consequently the defect density decreases, as shown schematically in Fig. 3.7.

It is further postulated that the defects discussed above act as charge traps. This postulate has the following consequences for the electrical properties. The initial increase in defect density results in an increase in the charge density, a concomitant increase in band bending, and hence an increase in $|\Delta V_{FB}|$. As the interface moves away from the charged defects, the image potential, and hence $|\Delta V_{FB}|$, decreases, although this effect could, in principle, be offset by a continuing increase in the charge density. As the interface continues to move away from the charged defects, however, the decreased defect density resulting from decreased strain will cause a decrease in the charge density and thus a decrease in $|\Delta V_{FB}|$. In addition to the effect of decreasing strain, electrical properties can also be affected by a decreased strain gradient. A correlation has previously been noted^{83,84} between decreased strain gradients and lower values of the radiation-generated interface trap density. A decreased strain gradient may also play a role in the behavior of $|\Delta V_{FB}|$.

It is important to note that the model discussed above does not depend on the identity of the defects which are proposed to relieve strain. Some possibilities are dangling orbitals and hydrogen-related defects, such as Si bonded to hydroxyl or amino groups or to hydrogen. However, if the defects are hydrogen related, only a small fraction of the defects could be electrically active, since the concentration of hydrogen in nitrided oxide films has been

measured⁶² to be several atomic percent, which is far greater than the concentration of electrically active defects required to account for the observed⁵⁷ flatband voltage shifts.

The model discussed above to explain the behavior of $|\Delta V_{FB}|$ as a function of nitridation time also explains the behavior of $|\Delta V_{FB}|$ as a function of other processing variables. For $t_N = 30$ minutes, the maximum value of $|\Delta V_{FB}|$ occurs⁵⁷ at $T_N = 1000^\circ\text{C}$. For $t_N = 60$ minutes, $|\Delta V_{FB}|$ reaches a maximum⁵⁷ at $T_N = 950^\circ\text{C}$. For $t_N = 90$ minutes, the maximum value of $|\Delta V_{FB}|$ still occurs⁵⁷ at $T_N = 950^\circ\text{C}$ although the absolute value is lower than for $t_N = 60$ minutes. For $t_N = 180$ minutes, the maximum value of $|\Delta V_{FB}|$ occurs⁵⁷ at $T_N = 900^\circ\text{C}$. This behavior is a consequence of slower nitridation reaction rates at low temperatures. This can be seen by noting that for $T_N = 800^\circ\text{C}$, $d_{Np} = 0$ even for $t_N = 240$ minutes, as shown in Fig. 3.5, while for nitridation temperatures of 1000°C (see Fig. 3.3), 1100°C ,⁶⁷⁻⁶⁹ and 1150°C (see Fig. 3.4), d_{Np} becomes nonzero within $t_N < 15$ minutes. Thus, at lower temperatures, the nitridation-induced defects form at a slower rate and are in the strained region near the interface longer, resulting in $|\Delta V_{FB}|$ reaching a maximum value at a later time. It would appear that a nitridation temperature near the viscous flow temperature of SiO_2 separates fast from slow nitridation reaction rates.

It has also been reported⁸⁵ that under the same nitridation conditions, nitridation of thicker oxides results in increased values of $|\Delta V_{FB}|$. Furthermore, under the same nitridation conditions, thicker oxides have been reported⁶⁴ to have less nitrogen incorporated in the interfacial region. Results of simulations also show (see section IV.D) a reduced interfacial nitrogen concentration for a larger initial oxide thickness, as well as a smaller value of

d_{Np} . A lower value of $[N]_p$ implies a lower defect concentration, and thus a lower value of $|\Delta V_{FB}|$ within the model discussed here. However, a lower value of d_{Np} implies a higher defect concentration. The net effect may be an increased defect concentration and could explain the observed⁸⁵ larger values of $|\Delta V_{FB}|$.

An indication of the defect distribution in the dielectric film can also be obtained from the XPS data by use of a fluorine marker. The HF/EtOH etchant used in this work leaves a fluorine residue on the surface. It is suggested that the fluorine makes bonds preferentially to defects in the dielectric film. The intensity of the F 1s photoelectron peak after each etch may thus yield a measure of the defect distribution in the dielectric film. The surface fluorine concentration should be considered an upper limit to the defect concentration, since some of the fluorine may be adsorbed, possibly weakly, at sites other than defect sites.

Figure 3.8 shows the number of F atoms bonded to the dielectric surface during the course of the depth profiling of samples 1 and 2, corresponding to the data in Figs. 3.3(a) and 3.3(b). The number of F atoms on the surface was estimated by calculating the F 1s/Si 2p ratio which would be expected for a monolayer (6.8×10^{14} atoms/cm²) of F atoms on Si, assuming that Δ_F (see Appendix A) is 1. The Si 2p intensity is estimated by calculating the expected attenuation of the measured clean Si substrate signal when a 2.5 Å thick overlayer with a 25 Å escape depth is present on the surface. The absolute intensity of the F 1s photoelectron peak for a monolayer of F atoms can thus be estimated and compared to the actual F 1s intensities measured during the course of the depth profile. In Fig. 3.8(a), a relatively large amount of F

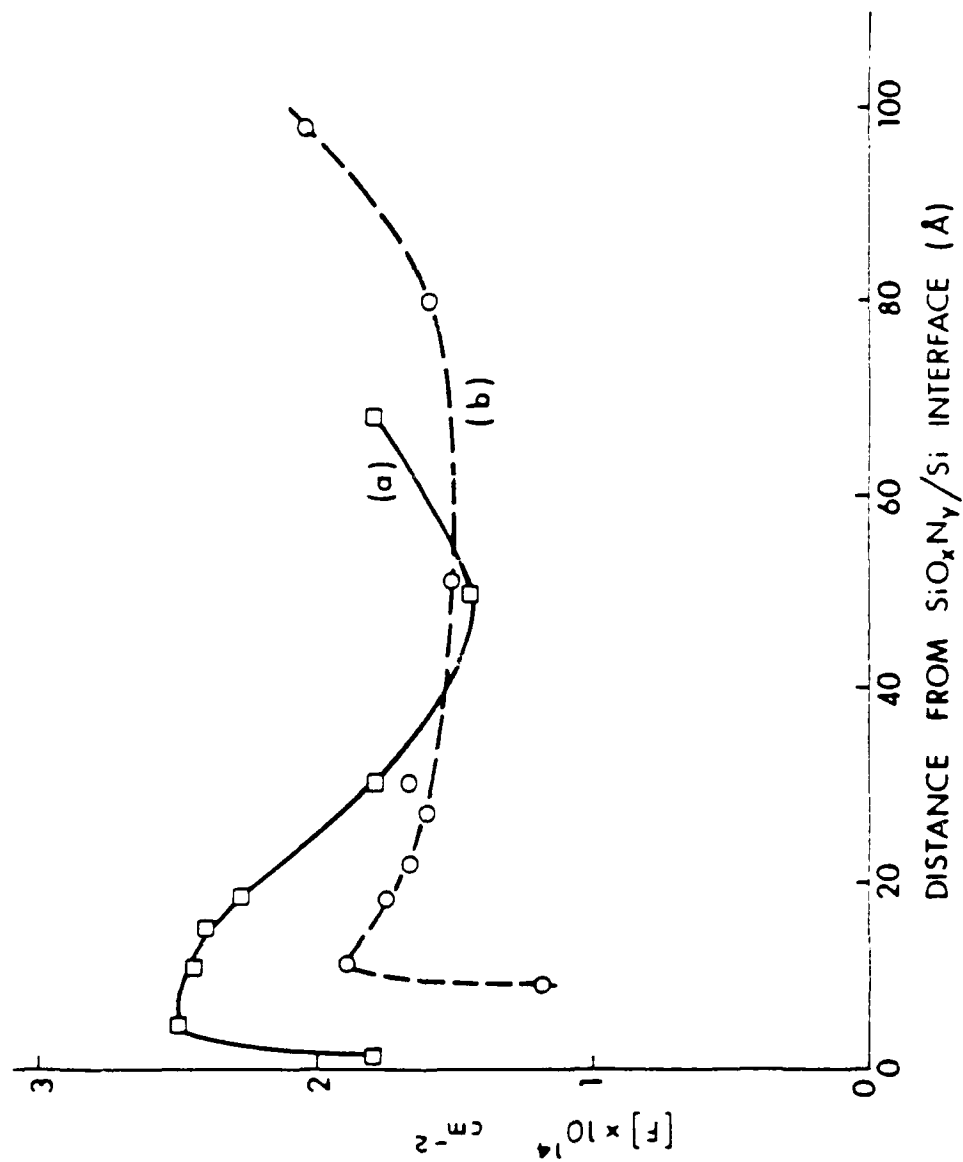


Figure 3.8. Surface fluorine concentrations measured during the course of depth profiles of samples nitrided at 1000°C for (a) 10 minutes, and (b) 30 minutes.

binds to the surface when the interfacial region has been exposed to the etchant, suggesting the formation of a large number of defects at the interface in the initial stages of nitridation. Comparing Fig. 3.8(b) to Fig. 3.8(b) shows that as the nitridation proceeds and the interfacial nitrogen peak occurs away from the interface, the maximum surface fluorine concentration is lower and also occurs further from the interface. This is precisely the behavior expected of the defect distribution based on the previously proposed strain-dependent defect formation model.

Figure 3.9 shows the surface fluorine concentration corresponding to the data in Fig. 3.4. The surface fluorine concentration correlates with the nitrogen distribution, suggesting an increased number of defects as the nitridation time increases from 5 minutes to 10 minutes, but distributed somewhat further from the interface. An increased concentration of charged defects would cause an increase in the flatband voltage shift. However, an increase in the separation of the charge from the interface would decrease the flatband voltage shift. Since the flatband voltage depends on both the concentration and spatial distribution of the charged defects, it is not clear how the electrical measurements would be affected. The electrical measurements⁵⁷ on which the defect formation model is based do not cover the nitridation conditions used for the samples corresponding to Figs. 3.4 and 3.9.

Figure 3.10 shows the surface fluorine concentration corresponding to the data in Fig. 3.5. Comparing Figs. 3.10(a) and 3.10(b) to Fig. 3.10(c) suggests an increased defect concentration at the interface as the nitridation time increases from 1 hour to 4 hours. This is consistent with the reported⁵⁷

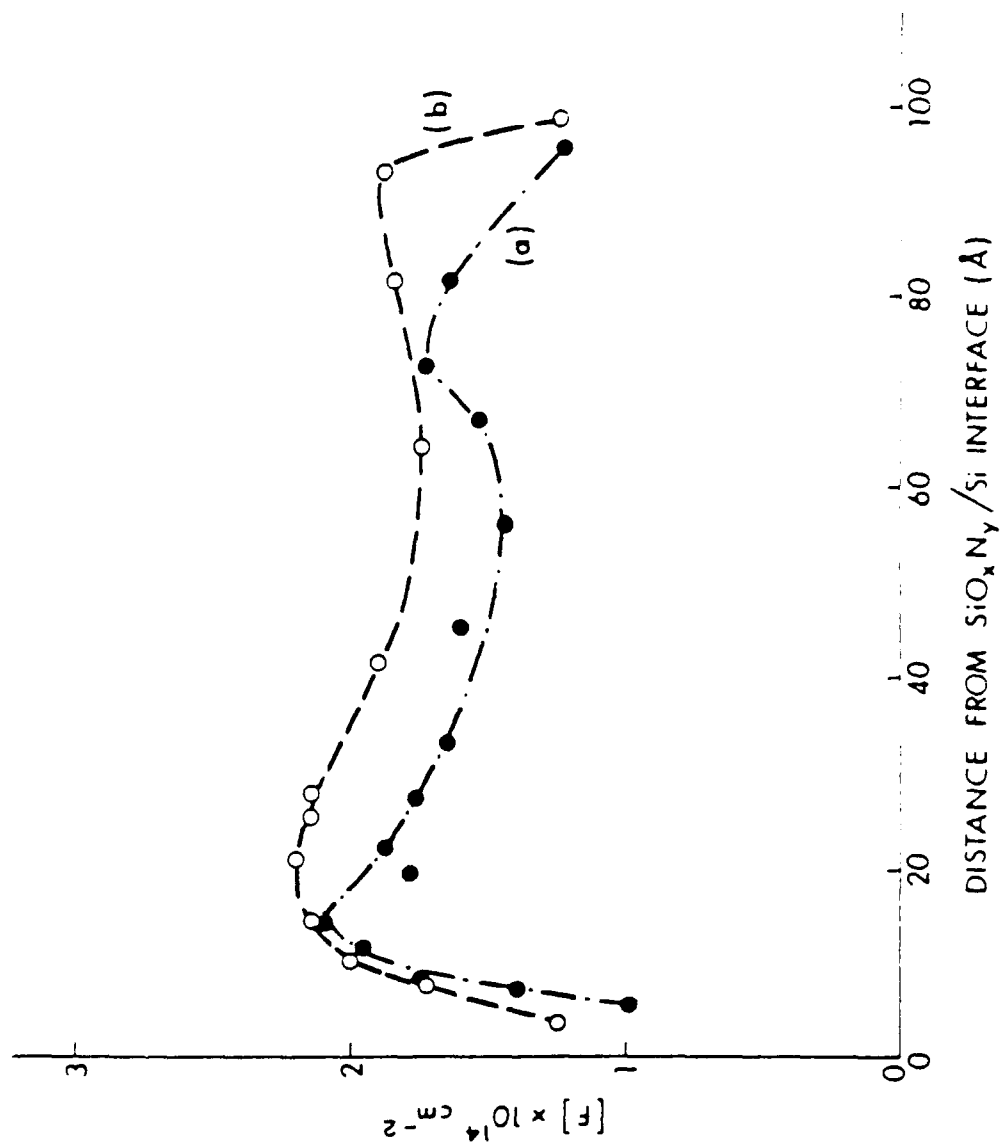


Figure 3.9. Surface fluorine concentrations measured during the course of depth profiles of samples nitrided at 1150°C for (a) 5 minutes, and (b) 10 minutes.

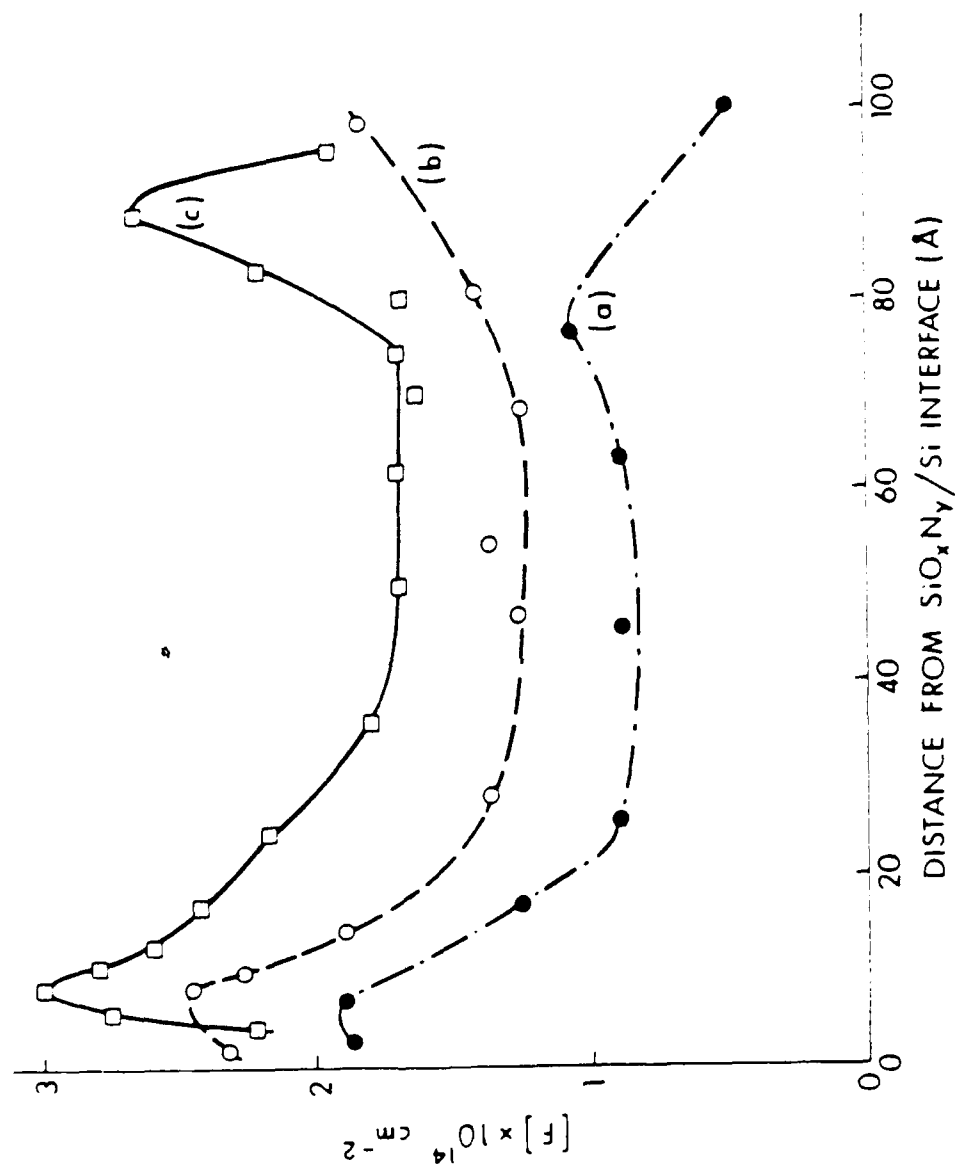


Figure 3.10. Surface fluorine concentrations measured during the course of depth profiles of samples (a) oxidized at 825°C , then nitrified at 800°C for 60 minutes, (b) oxidized at 1000°C , then nitrified at 800°C for 60 minutes, and (c) oxidized at 1000°C , then nitrified at 800°C for 240 minutes.

monotonic increase in the magnitude of the flatband voltage shift with increasing nitridation time at low nitridation temperatures. Comparing Figs. 3.10(a) and 3.10(b) to Fig. 3.5(a) suggests that, even though the oxidation temperature does not appear to affect the nitridation kinetics responsible for the nitrogen distribution, it does affect the defect formation kinetics. The data in Fig. 3.10 suggest that defect formation is reduced in the oxide which is expected to have the higher strain. It has previously been suggested^{83,84} that increased strain in the bulk of the oxide reduces the interfacial strain gradient, resulting in a reduced concentration of radiation-generated interface traps. An analogous effect may be occurring in the present work.

Figures 3.8 through 3.10 show that the surface fluorine concentration in nitrided oxides is near 10^{14} cm^{-2} . This is far greater than the number of charged defects required to account for observed⁵⁷ flatband voltage shifts. For comparison, the surface fluorine concentration observed during the course of a depth profile of a thermally grown SiO_2 film on Si is near 10^{13} cm^{-2} , and is near 10^{12} cm^{-2} on the surface of the clean Si substrate after the SiO_2 has been completely removed. However, device quality thermal oxides have a concentration of electrically active defects as low as $10^{10} \text{ eV}^{-1} \text{ cm}^{-2}$ at midgap. It is clear that only a small fraction of the defects associated with the fluorine marker can be electrically active. It is suggested, however, that the distribution of electrically active defects may follow the same behavior as the distribution of defects deduced from the surface fluorine concentration. Comparing Figs. 3.8 to 3.10 with Figs. 3.3 to 3.5, it is clear that the surface fluorine concentration, and hence the defect distribution, is correlated to the nitrogen distribution. This is consistent with the strain-dependent energy of

formation of defects, proposed earlier to explain the observed⁵⁷ behavior of the flatband voltage shift. In addition, recent electrical measurements⁵⁸ show that the positive charge is centered 24 Å from the $\text{SiO}_x\text{N}_y/\text{Si}$ interface for a 100 Å SiO_2 film which has been nitrified at 1000°C for 10 minutes. The fact that the peak interfacial nitrogen concentration, the maximum surface fluorine concentration, and the positive charge center all occur away from the interface strongly suggests that the defects are associated with the nitrogen and that the fluorine makes bonds preferentially with defect sites, thus supporting the previously proposed defect model.

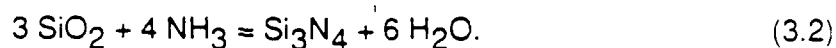
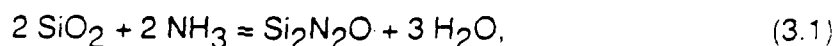
IV. Modeling of the Kinetics of Nitridation

This section describes simulations of the nitridation process. The nitridation process is described in section IV.A, the kinetic model presented in section IV.B, the choice of kinetic parameters described in section IV.C, and the simulation results are presented in section IV.D.

IV. A. The Nitridation Process

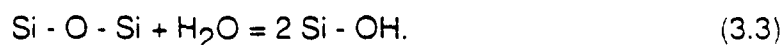
Several reactions are involved in the nitridation process. These include reaction of the SiO_2 with NH_3 , diffusion of the NH_3 and reaction byproducts through the oxynitride, possible reaction of the byproducts with the SiO_xN_y , and reaction of the substrate with the diffusing species. In the following, the nature of each of these reactions will be considered.

There are three stable phases in the Si - N - O phase diagram⁸⁶ -- SiO_2 , $\text{Si}_2\text{N}_2\text{O}$, and Si_3N_4 . The reaction of SiO_2 with NH_3 may therefore be described by the following reactions:

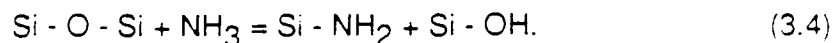


A recent infrared (IR) study⁶¹ found that nitrided oxides have an IR absorption at a frequency which is near that observed for trisilylamine ($\text{N}(\text{SiH}_3)_3$). The bonding about the nitrogen in trisilylamine is trigonal planar, rather than the more common pyramidal. The IR study⁶¹ would not distinguish between $\text{Si}_2\text{N}_2\text{O}$ and Si_3N_4 , however, since the Si-N-Si bond angle in $\text{Si}_2\text{N}_2\text{O}$ is^{87,88} 120° , while that in Si_3N_4 is⁸⁸ 119.9° , both consistent with trigonal planar bonding. In the depth profiles of nitrided oxides presented in Section III.A, the concentration ratio $[\text{N}]/([\text{O}] + [\text{N}])$ never exceeds 0.67, consistent with the final reaction product being $\text{Si}_2\text{N}_2\text{O}$. Of the two reactions being considered, (3.1) is thermodynamically favored.^{60,65} Finally, $\text{Si}_2\text{N}_2\text{O}$ has been reported⁸⁹ to form when SiO_2 is heated in NH_3 in the temperature range $550\text{-}1250^\circ\text{C}$, while formation of Si_3N_4 is reported⁸⁹ at higher temperatures. We therefore conclude that the formation of $\text{Si}_2\text{N}_2\text{O}$ via reaction (3.1) is more likely to occur for the nitridation conditions being considered here.

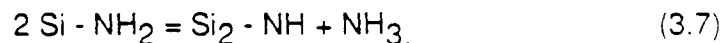
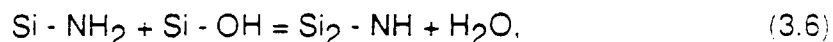
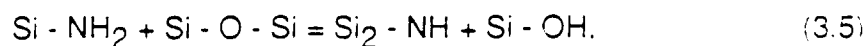
The diffusion of gases in fused silica has been extensively studied.⁷¹⁻⁷³ H_2O reacts with SiO_2 to form silanol via the reaction



This reaction is reversible, with the H_2O being the diffusing species. A similar reaction presumably occurs with NH_3 :



This differs from the case of H_2O , however, since the amino groups may become immobile by the formation of multiple Si - N bonds, without necessarily releasing the diffusing NH_3 , via the reactions

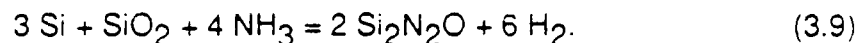


and similar reactions involving the formation of a third Si - N bond. These reactions may be reversible. However, the necessity of breaking multiple Si - N bonds before diffusion can occur would be expected to greatly reduce the rate of formation of the diffusing NH_3 , compared to the rate in the case of Si - NH_2 , which requires breaking a single Si - N bond.

The occurrence of reactions such as (3.6) means that H_2O , as well as NH_3 , is present and diffusing in the SiO_xN_y during the nitridation. The presence of both diffusing species makes it unlikely that SiO_2 or Si_3N_4 will result from the reaction of the substrate with the diffusing species. The formation of $\text{Si}_2\text{N}_2\text{O}$ could result from reaction of the substrate directly with the diffusing species, via the reaction^{60,65}



Alternatively, the interfacial SiO_2 may also be involved, via the reaction⁶⁵



Of these two reactions, (3.8) is energetically more favorable.⁶⁵ Depending on the relative concentrations of the diffusing species, nowever, oxynitrides of different average stoichiometries could result.

The nitridation process can be summarized as follows. The ammonia enters the SiO_2 , through which it can diffuse and chemically react. The substitution of N for O in the oxide can release H_2O , which is then free to diffuse and possibly react with the oxynitride. Those diffusing species which do not become immobilized by reaction with the oxynitride and which diffuse to the interface can react with the substrate. A kinetic model of the various reactions discussed above which are involved in the nitridation process will now be described.

IV. B. The Kinetic Model

The processes discussed in Section IV.A can be modeled using either a numerical approach or by attempting an analytical solution of the diffusion equation with chemical reaction. The diffusion equation with chemical reaction has been solved for several cases.⁹⁰ However, the cases considered⁹⁰ involved a constant diffusion coefficient. In the present case, the diffusion coefficient will depend upon the amount of nitrogen incorporated in the oxynitride, since nitrided oxides are known^{50,52,53,60} to be better diffusion barriers than is SiO_2 . From the data presented in Section III.A, it is

clear that the nitrogen concentration varies both with the nitridation time and the position within the oxide. The diffusion coefficient will therefore also be a function of position and time, greatly complicating the solution even for simplified cases. Adding the effects of strain and multiple diffusing species (e.g. to account for reaction (3.6)) further complicates the equation to be solved. A numerical method then becomes preferable for reasons of simplicity and flexibility.

Since amorphous materials (SiO_2 , SiO_xN_y) are being considered, a model which considers local atomic arrangements is impractical, especially for the size (~ 100 Å thick SiO_2 layer) of the system being modeled. It is therefore necessary to consider only average properties. This makes dealing with a large number of each reacting species feasible, which is necessary if the probabilities for the various reactions (diffusion, incorporation) vary widely. In addition, a model which considers only average properties and a large number of each reacting species will result in less statistical scatter in the final results than a Monte-Carlo approach in which every atom is considered.

Assume that the SiO_xN_y is laterally uniform both chemically and structurally at all times. The dielectric layer can then be divided into a number of thinner layers, each with its own average diffusion coefficients, incorporation probabilities, and chemical composition. This reduces the problem to one dimension. We shall assume that the hopping distance for diffusing species is 2.63 Å, which is the O - O nearest neighbor separation in α -quartz. Letting the layer thickness be the same as the hopping distance, 35 layers would then correspond to a 92-Å-thick dielectric layer.

Before discussing the simulated nitridation in detail, an overview is presented in the following. After each time interval Δt , the amount of diffusing nitrogen in the surface layer is initialized to the solubility limit. Each diffusing species (NH_3 and H_2O) is then allowed a single incorporation attempt in the oxynitride or substrate layer in which it is located. That fraction of each diffusing species which does not react is then allowed a single interlayer hopping attempt, and the process repeats. An overview of the kinetic simulation is shown schematically in Fig. 3.11. The probability of each of these reactions occurring within Δt can be calculated, as discussed later. In the following, the probabilities will be assumed to be known.

Let N_0 be the total number of available hopping sites within each layer, and f_0 the fraction of available sites in the surface layer which are occupied by the diffusing N species at time $t = t_0$, when nitridation is initiated. Let $N_{\text{hop},j}(t)$ and $N_{\text{inc},j}(t)$ be the amount of nitrogen hopping and incorporated, respectively, within the j^{th} layer at time t , where $j = 1$ is the surface layer. $N_{\text{hop},1}(t_0)$ is then equal to $f_0 N_0$ and $N_{\text{inc},j}(t)$ is zero for all j . Since the surface layer is in direct contact with the NH_3 ambient, f_0 will be chosen so that $f_0 N_0$ is the solubility limit of the diffusing N species in SiO_2 , as discussed in the next section. As the nitridation proceeds, the incorporation of nitrogen will decrease the solubility limit, since nitrided oxides are known to be good diffusion barriers.^{50,52,53,60} It is assumed that the solubility limit for the diffusing N species decreases linearly as $N_{\text{inc},1}(t)$ increases to some limiting value, i.e. the final reaction product is assumed to be a perfect diffusion barrier. The effect of this assumption is to halt the nitridation as $N_{\text{inc},1}(t)$ asymptotically approaches the limiting value. The choice of this limiting value determines

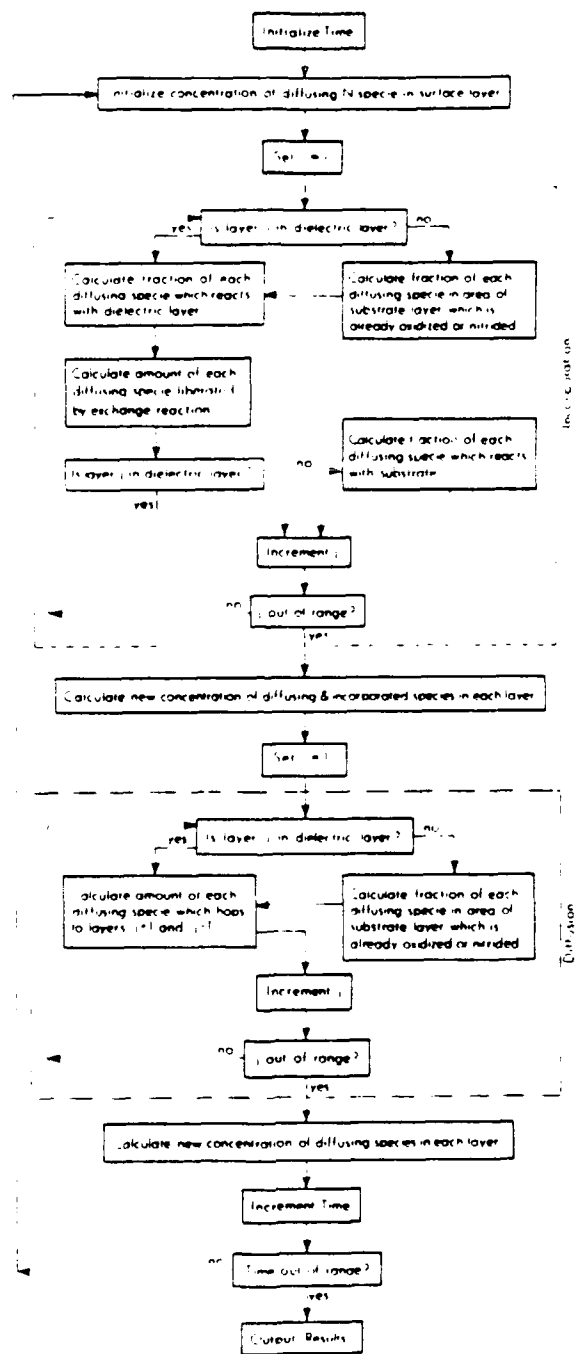


Figure 3.11. Schematic overview of the kinetic model.

the final reaction product in the simulated nitridation process. The limiting value will be written as $x_L N_O$, so that the final reaction product, $Si_3N_{4x}O_{6(1-x)}$, is obtained when $x = x_L$. The amount of diffusing nitrogen in the surface layer is then determined by

$$N_{hop,1}(t) = f_0(N_0 - N_{inc,1}(t)/x_L). \quad (3.10)$$

The process of incorporation is shown schematically in the portion of Fig. 3.11 enclosed by the dashed lines. The amount of diffusing nitrogen which incorporates in the j^{th} oxynitride layer within the n^{th} time interval Δt is given by

$$\Delta N_{inc,j}(t_n) = N_{hop,j}(t_n) P_{N,ox,inc,j}(\Delta t), \quad (3.11)$$

where $t_n = t_0 + n\Delta t$ and $P_{N,ox,inc,j}(\Delta t)$ is the probability of nitrogen incorporation in the j^{th} oxynitride layer within time Δt . The total amount of nitrogen incorporated in the j^{th} oxynitride layer is then

$$N_{inc,j}(t_n) = \Delta N_{inc,j}(t_n) + N_{inc,j}(t_{n-1}). \quad (3.12)$$

$N_{hop,j}(t_n)$ is correspondingly decreased by $\Delta N_{inc,j}(t_n)$. From reactions (3.1) and (3.2), each nitrogen which incorporates in the dielectric layer displaces on the average $3/2$ O. Therefore, $O_{hop,j}(t_n)$ is increased by $3/2 \Delta N_{inc,j}(t_n)$. Incorporation of oxygen in the oxynitride is similar.

Incorporation of nitrogen and oxygen in the substrate is only slightly more involved (see Fig. 3.11). For a substrate layer which has only partially

been converted to an oxynitride, the probability that the diffusing species occupy sites which have already been oxidized or nitrified is calculated. That fraction of each diffusing species contained in oxynitride areas is treated in exactly the same manner as discussed above. The fraction which occupies unreacted substrate areas is treated in a similar manner, using appropriately different probabilities and with no displacement to create diffusing species.

The fraction of each diffusing species which has not incorporated is next allowed to diffuse, as shown schematically in the portion of Fig. 3.11 enclosed by dot-dashed lines. In this model, only single-layer hops are allowed, and only one interlayer hop is allowed within the time interval Δt . The probability that a hop will occur is decreased by the probability of target sites already being occupied by diffusing species, and by the fact that some of the target sites are part of a diffusion barrier. This model results in a diffusion constant which decreases linearly with increasing N incorporation until it is zero for $x = x_L$. It is assumed that the diffusing species and the SiO_xN_y form an ideal solution, with no heat of mixing and no change in chemical potential as a function of position in a concentration gradient, so that a chemical potential does not provide a driving force for diffusion. The simplifying assumptions of no interaction between diffusing species and no dependence of the diffusion constant on the concentration of diffusing species are also made. The amount of nitrogen which hops from layer j in the + (towards the substrate) and - (towards the surface) directions is then given by

$$\Delta N_{\text{hop},j\pm 1}(t_n) = (1/2)N_{\text{hop},j}(t_n)P_{N,\text{hop},j\pm 1}(t_n)\{1 - [N_{\text{inc},j\pm 1}(t_n)/x_L + N_{\text{hop},j\pm 1}(t_n) + O_{\text{hop},j\pm 1}(t_n)]/N_0\}. \quad (3.13)$$

The factor of 1/2 gives equal weight to forward and backward hopping, *i. e.* only self-diffusion is considered, and there are no driving forces which result in a preferential hopping direction. $N_{\text{hop},j}(t_n)$ is decreased and $N_{\text{hop},j\pm 1}(t_n)$ are increased by $\Delta N_{\text{hop},j\pm 1}(t_n)$. Similar equations determine oxygen hopping. Diffusing species which occupy unreacted substrate sites are not allowed to hop further into the substrate, *i.e.* the solubility of the diffusing species in the substrate is assumed to be negligible.

Each of the probabilities mentioned above must be estimated. In order to calculate the probability, it is assumed that each of the reactions considered follows first order chemical kinetics. The concentration of a reacting species as a function of time $c(t_n)$ is then given by

$$c(t_n) = c(t_{n-1})\exp(-R\Delta t), \quad (3.14)$$

where R is the rate constant. Within time Δt , the probability $P(\Delta t)$ for the reaction to occur is

$$P(\Delta t) = 1 - c(t_n)/c(t_{n-1}) = 1 - \exp(-R\Delta t). \quad (3.15)$$

Assuming an Arrhenius form for the temperature dependence of the reaction rate, Eq. (3.15) becomes

$$P(\Delta t) = 1 - \exp[-\Delta t R_0 \exp(-\Delta E_A/k_B T)], \quad (3.16)$$

where ΔE_A is the activation energy and k_B is Boltzman's constant. Thus, if ΔE_A and R_0 can be determined, the probability of a reaction occurring within time Δt can be calculated. The choice of these kinetic parameters will now be considered.

IV. C. Choice of Kinetic Parameters

The solubility limits in fused silica of gases which do not readily react with the SiO_2 matrix, such as He, O_2 , and N_2 , are generally 0.01 - 0.03 times the concentration of the atoms or molecules in the gas phase.⁷¹ For reactive H_2O , however, the solubility limit is three orders of magnitude higher⁷¹⁻⁷³ due to reaction (3.3). It is estimated⁷² that the solubility of free H_2O is about the same as other gases in SiO_2 , with the apparent higher solubility due to the fact that most of the H_2O is trapped as silanol at any given time. Experiments have shown⁷³ that the solubility of H_2O in fused silica is nearly constant in the temperature range 900-1200°C, and increases at lower temperatures. Expressed as the number of hydroxyl groups per Si atom in SiO_2 , the solubility limit of H_2O ranges⁷³ from 3×10^{-3} at 1200°C to 4×10^{-3} at 800°C, which is the nitridation temperature range of interest in this work. The occurrence of reaction (3.4) is likely to make the solubility of NH_3 in SiO_2 close to that of H_2O , or possibly somewhat lower due to the larger size of NH_3 compared to H_2O . For these simulations, f_0 was chosen to be 2×10^{-3} at high nitridation temperatures, and 2.7×10^{-3} below 900°C. Since f_0 is defined relative to the number of nitrogen incorporation sites, and 4 nitrogen atoms can incorporate for every 3 Si atoms, the corresponding number of amino groups per Si atom is 2.7×10^{-3} for nitridation temperatures of 900°C and

above, and 3.6×10^{-3} at lower temperatures. For reasons discussed in Section IV.A, the final nitridation reaction product is likely to be $\text{Si}_2\text{N}_2\text{O}$, so x_L is set to 0.75 in the simulation. The value of Δt is chosen to be large enough to minimize computing time, yet small enough to prevent the reaction probabilities from approaching 1. The value of Δt is therefore chosen to be in the range 10^{-2} - 10^{-4} seconds, depending on the nitridation temperature. The value of N_0 is chosen to be 10^{12} , which would correspond to a surface area of the order of 10^{-4} cm^2 .

To the author's knowledge, no experimental measurements of the kinetic parameters for reactions (3.1) and (3.2) have been reported. R_0 and ΔE_A for nitrogen incorporation in the oxide, $R_{0,(N,inc,ox)}$ and $\Delta E_{A,(N,inc,ox)}$, can be estimated from measured surface nitrogen concentrations from samples nitrided at 1000°C (Fig. 3.3) and 800°C (Fig. 3.4) for times sufficiently short that the surface has not reached its saturation nitrogen concentration. Equation (3.16) can be written as

$$R_0(T_1) = -(1/\Delta t) \exp[\Delta E_A/k_B T_1] \ln[1 - P(\Delta t, T_1)]. \quad (3.17)$$

A similar equation can be written at $T = T_2$. Assuming that R_0 is independent of temperature, the two equations can be set equal to each other to obtain

$$\Delta E_A = [k_B T_1 T_2 / (T_2 - T_1)] \ln[P(\Delta t, T_2)/P(\Delta t, T_1)], \quad (3.18)$$

which is valid if the probabilities are much less than 1. Estimates for the probabilities at T_1 and T_2 are obtained by using the assumed values of f_0 and

adjusting the probabilities to obtain the observed surface nitrogen concentrations at the temperatures and times considered. This gives $\Delta E_{A,(N,inc,ox)} = 1.47$ eV and, from Eq. (3.17), $R_{0,(N,inc,ox)} = 3.65 \times 10^5 \text{ sec}^{-1}$. If the temperature dependence of the solubility is taken into account, $\Delta E_{A,(N,inc,ox)} = 1.6$ eV and $R_{0,(N,inc,ox)} = 1.2 \times 10^6 \text{ sec}^{-1}$ are obtained.

Estimates of the kinetic parameters for the reverse reaction are more difficult to obtain. For each Si-O bond which is replaced by a Si-N bond via reaction (3.1) or (3.2), the free energy is increased by ~ 0.2 eV.^{60,65} If the energy barrier is unchanged by the nitridation reaction, ΔE_A for the reverse reaction, $\Delta E_{A,(O,inc,ox)}$, would therefore be 0.2 eV less than $\Delta E_{A,(N,inc,ox)}$. Relaxation of the local atomic environment to a more stable arrangement after the nitridation, however, may affect the barrier height. For those calculations considering a reversible nitridation, $R_{0,(O,inc,ox)}$ is assumed to be the same as $R_{0,(N,inc,ox)}$, and $\Delta E_{A,(O,inc,ox)}$ is 1.4 eV.

Macroscopic stress is assumed not to affect the incorporation reactions discussed above, but the effects of interfacial strain are included in the simulation. Since the strained bonds are more easily broken,^{76,77,79,80} a lower activation energy for nitrogen incorporation in the interfacial region is assumed, decreasing linearly by 0.3 eV as the interface is approached in the 10 dielectric layers (26.3 Å) closest to the interface, to simulate the bond strain gradient.^{76,77} Enhanced nitrogen incorporation in the interfacial region may be an indirect consequence of strain, since increased hydrogen incorporation near the interface^{64,91} may act as a strain relief mechanism. Replacing Si-OH or Si-H bonds with Si-N bonds may be energetically more favorable than reaction (3.4).

The activation energy for the reaction of the diffusing H_2O with the substrate, $\Delta E_{A,(O,inc,Si)}$, can be obtained from kinetic studies of the steam oxidation of Si (100). The oxide thickness increases linearly⁹² with time in the thin oxide regime where the oxidation rate is limited by the interfacial reaction, and parabolically⁹² for thicker oxides where the oxidation is diffusion limited. In the regime where the oxidation is reaction limited, the activation energy has been measured⁹³ to be 2.05 eV for oxidation temperatures above 900°C and 1.6 eV for oxidation temperatures of 900°C and below. A similar temperature effect has been observed^{94,95} for oxidation of Si in O_2 and has been attributed to the macroscopic stress observed⁷⁴ in low temperature oxides. In the simulation, $R_{O,(O,inc,Si)}$ is set arbitrarily large (10^{12} sec^{-1}) to ensure that the reaction is diffusion limited. Although an oxide thickness of 100 Å is not in the diffusion limited regime, this choice is motivated by the fact that nitrided oxides are good diffusion barriers,^{50,52,53,60} and nitrogen incorporates rapidly in the interfacial region,^{13-18,67-69} thus forming a diffusion barrier early in the nitridation process.

The kinetics of the reaction between Si and NH_3 are poorly understood, though some studies have been done.^{59,60,64,67,96,97} Attempts to determine the linear rate constant, which is determined by the interfacial reaction, are complicated by the fact that the thickness of the grown Si_3N_4 film is self-limiting at a few tens of Angstroms, and the grown films have a significant oxygen content which may affect the nitridation kinetics. In the simulations, the kinetic parameters for the reaction of the substrate with NH_3 , $R_{O,(N,inc,Si)}$ and $\Delta E_{A,(N,inc,Si)}$ are chosen to be the same as for the reaction with H_2O .

As previously mentioned, the diffusion of H_2O in fused silica has been

extensively studied.⁷¹⁻⁷³ Reaction (3.3) is not a first order reaction, but rather depends on the square root of the H₂O concentration, as expected if reaction (3.3) is an elementary reaction. Reaction (3.3) is not the only pathway by which H₂O diffusion can occur, however. Reactions such as (3.6) can also occur, and hydroxyl groups in a strain gradient can diffuse singly,⁷⁷ rather than in pairs as expected from reaction (3.3). The existence of multiple reaction pathways makes estimating the overall order of the reaction difficult. For simplicity, first order kinetics will be assumed.

The activation energy for diffusion of H₂O in fused silica is 0.78 eV, in exact agreement with measurements⁹³ of the parabolic (diffusion limited) rate constant for oxidation of Si in H₂O above 900°C. At 900°C and below, the activation energy is⁹³ 1.17 eV. In the simulations, the activation energy for diffusion of H₂O in the oxynitride, $\Delta E_{A,(O,hop,ox)}$, is set to these values in the appropriate temperature ranges. $R_{0,(O,hop,ox)}$ can be estimated from the effective diffusion constant D_{eff} , which is¹⁵⁷ $6.3 \times 10^{-10} \text{ cm}^2 \text{ sec}^{-1}$ at 1000°C, using the relation⁹⁸

$$D_{eff} = (1/2)Ra^2, \quad (3.19)$$

where a is the hopping distance. Using the Arrhenius relationship between R and R_0 and $\Delta E_{A,(O,hop,ox)} = 0.78 \text{ eV}$, which is appropriate at 1000°C, $R_{0,(O,hop,ox)} = 2.2 \times 10^9 \text{ sec}^{-1}$ is obtained. In the simulations, $R_{0,(O,hop,ox)}$ is assumed to be independent of temperature, and only $\Delta E_{A,(O,hop,ox)}$ is changed at low nitridation temperatures.

Interfacial strain may also affect the diffusion kinetics. The smaller ring

size in the strained region should increase the activation energy for diffusion of species which do not react with the SiO_2 matrix. In fact, the kinetics of the dry O_2 oxidation of Si has been explained^{99,100} with an interfacial layer in which a lower diffusivity is exhibited, and a higher activation energy has been measured¹⁰¹ for thin oxides. Enhanced diffusivity has been proposed,⁷⁷ however, for hydroxyl groups in the bond strain gradient model. Enhanced diffusivity in thin ($< 100 \text{ \AA}$) oxides via transport through micropores has also been proposed¹⁰² to explain the initial oxidation of Si in O_2 , which is faster than the linear-parabolic model predicts. Increased incorporation of hydrogen near the interface^{64,91} may contribute to a more open oxide structure in which diffusion is enhanced. The effect of interfacial strain on diffusion is therefore simulated by linearly decreasing the activation energy (i.e. increasing the hopping probability) by 0.15 eV as the interface is approached in the 10 dielectric layers closest to the interface.

The activation energy for ammonia diffusion in fused silica, $\Delta E_{A,(N,hop,ox)}$, has not been reported, but can be estimated. Activation energies for diffusion in fused silica for many gases follow the relation⁷¹

$$(\Delta E_A)^{1/2} = a + br, \quad (3.20)$$

where a and b are constants and r is the molecular radius. However, molecular size alone does not determine the activation energy. For example, H_2O ($r = 1.65 \text{ \AA}$, $\Delta E_A = 0.78 \text{ eV}$) is close in size^{71,72} to Ar ($r = 1.6 \text{ \AA}$, $\Delta E_A = 1.16 \text{ eV}$), O_2 ($r = 1.6 \text{ \AA}$, $\Delta E_A = 1.09 \text{ eV}$), and N_2 ($r = 1.7 \text{ \AA}$, $\Delta E_A = 1.12 \text{ eV}$), but the activation energy is lower than expected from size considerations alone.

Part of the problem may be the measurement of the molecular radius, which is typically calculated from gas viscosities assuming a spherical molecule, which is inappropriate for H_2O .

An alternative explanation is that, of the gases studied,^{71,72} only H_2O has a dipole moment (1.85 debye). The interaction of the dipole with the polarizable SiO_2 matrix could lower the activation energy. The activation energy for NH_3 diffusion in SiO_2 based on molecular size ($r = 1.82 \text{ \AA}$) alone would be $\sim 1.5 \text{ eV}$. However, since NH_3 has a dipole moment (1.47 debye) and is likely to diffuse by a mechanism similar to that of H_2O , a lower activation energy would be expected.

In the simulations, $\Delta E_{A,(N,hop,ox)}$ is set to 1.2 eV for nitridation temperatures above 900°C , while 1.4 eV is used for nitridation temperatures of 900°C and below. $R_{0,(N,hop,ox)}$ is adjusted to reasonably reproduce data from 1000°C nitridations, then fixed at the same value at other temperatures. In the simulations, $R_{0,(N,hop,ox)} = 3.5 \times 10^7 \text{ sec}^{-1}$ has been used. This gives a diffusion coefficient of $\sim 2 \times 10^{-13} \text{ cm}^2 \text{ sec}^{-1}$ at 1000°C , considerably larger than the previously reported⁶⁵ 10^{-16} - $10^{-15} \text{ cm}^2 \text{ sec}^{-1}$. However, the mathematical treatment used in that study^{65,90} neglects the chemical reaction occurring and treats the measured concentration of nitrogen incorporated in the oxynitride as the concentration of the diffusing species. For reasons previously discussed, however, the concentration of diffusing NH_3 is likely to be quite small ($f_0 = 2 \times 10^{-3}$), and the measured incorporated nitrogen concentration consists primarily of the immobile nitrogen which has formed multiple Si-N bonds. In the simulations, the effect of interfacial strain on the diffusion of NH_3 is assumed to be the same as that for H_2O .

Table II. Summary of the kinetic parameters used in this work.

<u>Parameter</u>	<u>T>900°C</u>	<u>T≤900°C</u>
f_0	2×10^{-3}	2.7×10^{-3}
x_L	0.75	0.75
$\Delta E_{A,(N,inc,ox)}$	1.6 eV	1.6 eV
$R_{0,(N,inc,ox)}$	$1.2 \times 10^6 \text{ sec}^{-1}$	$1.2 \times 10^6 \text{ sec}^{-1}$
$\Delta E_{A,(O,inc,ox)}$	1.4 eV	1.4 eV
$R_{0,(O,inc,ox)}$	$1.2 \times 10^6 \text{ sec}^{-1}$	$1.2 \times 10^6 \text{ sec}^{-1}$
$\Delta E_{A,(O,inc,Si)}$	2.05 eV	1.6 eV
$R_{0,(O,inc,Si)}$	10^{12} sec^{-1}	10^{12} sec^{-1}
$\Delta E_{A,(N,inc,Si)}$	2.05 eV	1.6 eV
$R_{0,(N,inc,Si)}$	10^{12} sec^{-1}	10^{12} sec^{-1}
$\Delta E_{A,(O,hop,ox)}$	0.78 eV	1.17 eV
$R_{0,(O,hop,ox)}$	$2.2 \times 10^9 \text{ sec}^{-1}$	$2.2 \times 10^9 \text{ sec}^{-1}$
$\Delta E_{A,(N,hop,ox)}$	1.2 eV	1.4 eV
$R_{0,(N,hop,ox)}$	$3.5 \times 10^7 \text{ sec}^{-1}$	$3.5 \times 10^7 \text{ sec}^{-1}$

The values of the kinetic parameters used in the simulations are summarized in Table II.

IV. D. Results and Discussion

Figure 3.12 shows results of the kinetic modeling for a 1000°C nitridation temperature at various times, for the simplest case, in which the nitridation is irreversible and there are no strain effects (*i. e.* the kinetic parameters are the same in each dielectric layer). The peak N concentration near the interface forms very early in the nitridation process as the substrate reacts with the diffusing species, which initially consist primarily of the diffusing N species. The abrupt jump in the interfacial nitrogen concentration shown in Fig. 3.12 corresponds to the discontinuity in the nitrogen incorporation probability at the SiO_2/Si interface. As the amount of nitrogen incorporated in the oxide increases, more diffusing oxygen becomes available with increasing nitridation time. The increasing concentration of the diffusing O species relative to the diffusing N species results in a more oxygen-rich oxynitride forming at the interface as the reaction proceeds. In addition, the reaction of the substrate with the diffusing species means that the interface moves away from the initial interfacial nitrogen peak with increasing nitridation time. These two effects result in a peak in the interfacial nitrogen concentration which appears to move away from the interface with increasing nitridation time, as shown in Fig. 3.12. Thus, even the simplest model qualitatively reproduces observed^{13,14,17} nitrogen distributions for the same nitridation conditions. However, there are quantitative discrepancies. The width of the calculated interfacial nitrogen peak is much less than the observed width (see

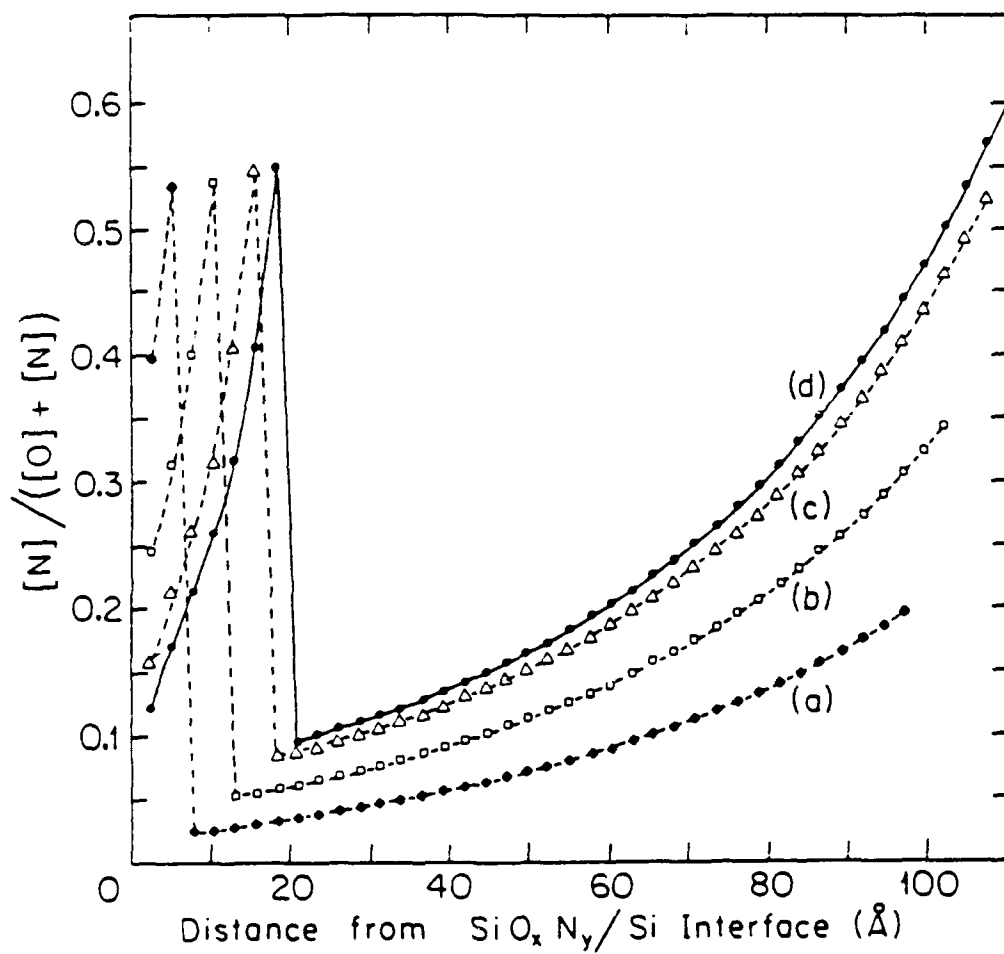


Figure 3.12. Calculated distribution of N in a SiO_xN_y film produced by nitriding a 92 Å-thick SiO_2 film at 1000°C for (a) 5 minutes, (b) 10 minutes, (c) 20 minutes, and (d) 30 minutes.

Fig. 3.3). The broadening of the interfacial peak in nitrogen concentration may be a manifestation of interfacial strain.

The effects of interfacial strain on the calculated nitrogen distribution for a 30 minute nitridation at 1000°C are shown in Fig. 3.13. The calculated curve from Fig. 3.12(d) (no strain effects) is shown in Fig. 3.13(a). Figure 3.13(b) shows the effect of including a decreased activation energy for nitrogen incorporation in the oxide near the interface, as discussed in the previous section. Although some broadening of the interfacial peak in nitrogen concentration is achieved, the discontinuity due to the dielectric/substrate interface is still clearly evident. Figure 3.13(c) shows the effect of including a decreasing activation energy for diffusion near the interface, in conformity with the bond strain gradient model. Including the enhanced diffusivity near the interface brings the calculated curve into closer agreement with the measured^{14,17} nitrogen distribution, and reduces the magnitude of the discontinuity in the nitrogen concentration. A slight further improvement can be obtained by extending the region of graded reactivity to the substrate side of the interface. Figure 3.13(d) shows the calculated nitrogen distribution which is obtained by reducing the probability (increasing the activation energy) for incorporation of nitrogen and oxygen in the two silicon layers closest to the interface. The calculated curves from Figs. 3.13(a) and 3.13(d) are shown in Fig. 3.14 together with the measured nitrogen distribution from Fig. 3.3(b).

While good agreement can be obtained between the experimental and calculated nitrogen distributions for a nitridation temperature of 1000°C, a critical test of the essential correctness of the kinetic model is its ability to

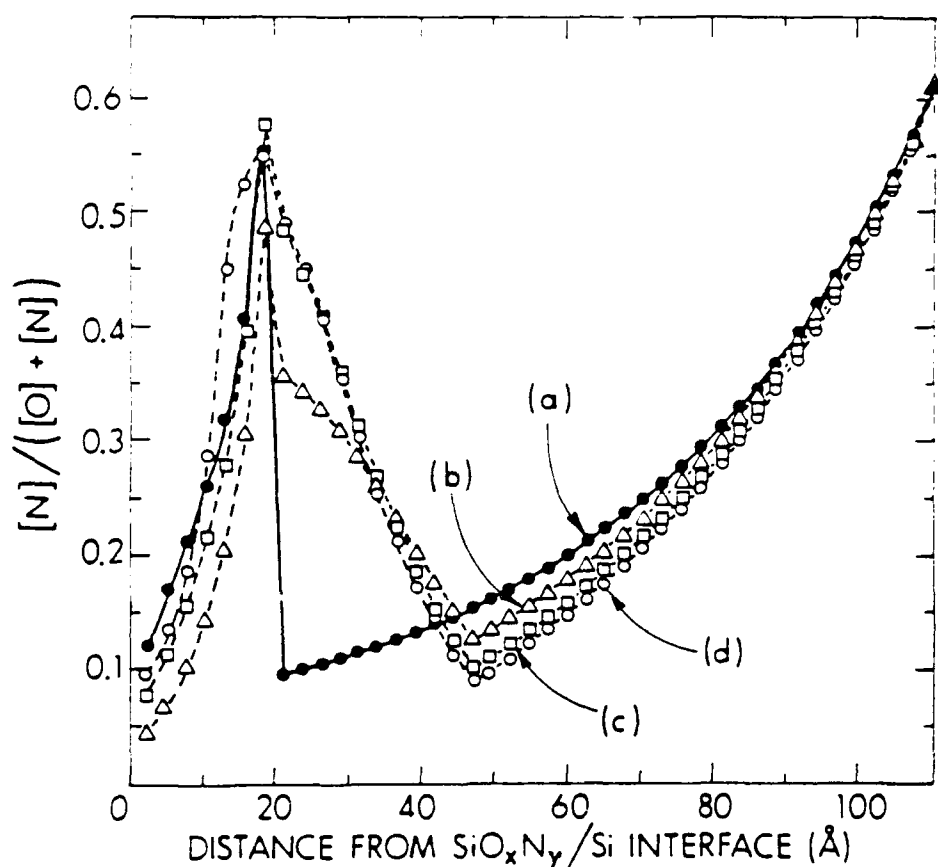


Figure 3.13. (a) Calculated curve from Fig. 3.12(d). (b) Effect of including an activation energy for nitrogen incorporation in the oxide which decreases linearly within 26 Å of the interface as the interface is approached. (c) Same as (b), but including activation energies for hopping of diffusing species in the oxynitride which decrease linearly in the interfacial region. (d) Same as (c) but extending the region of graded reactivity to include the two Si layers in the substrate which are closest to the $\text{SiO}_x\text{N}_y/\text{Si}$ interface.

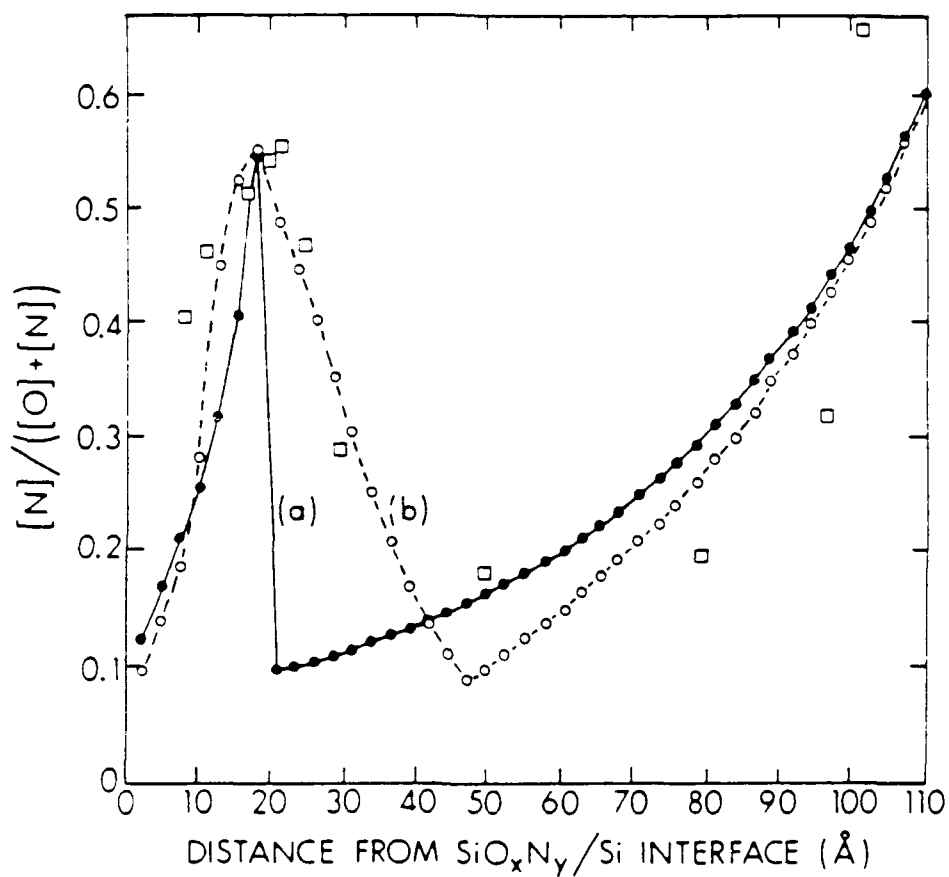


Figure 3.14. Comparison of the experimental nitrogen distribution in a SiO_xN_y film, produced from a 100 \AA -thick SiO_2 film nitrided for 30 minutes at 1000°C (squares, from Fig. 3.3(b)), to the calculated nitrogen distributions (a) from Fig. 3.13(a), and (b) from Fig. 3.13(d).

predict nitrogen distributions obtained at other nitridation temperatures. Figure 3.15(a) shows the calculated nitrogen distribution for a 10 minute nitridation at 1150°C, using the same kinetic parameters that were used to calculate the nitrogen distribution shown in Figs. 3.13(d) and 3.14(b). The experimental nitrogen distribution from Fig. 3.4(b) is also shown in Fig. 3.15. Reasonable agreement between the experimental data and the simulation is evident. The nitridation occurs on a faster time scale due to the higher temperature, and the peak interfacial nitrogen concentration saturates at a lower value, as can be seen by comparing Figs. 3.14 and 3.15. The lower value of the peak interfacial nitrogen concentration is due to the increased probability of NH_3 reacting with Si-O bonds at the elevated temperature, resulting in more nitrogen incorporating in the oxynitride and less diffusing to the interface. The increased nitrogen incorporation in the oxynitride also results in an increase in the concentration of diffusing oxygen, so that a more oxygen-rich oxynitride forms at the interface compared to the 1000°C nitridation. The fact that the simulation correctly predicts this key feature strongly suggests that the essential physics of the nitridation process is contained in the kinetic model.

Figure 3.15(b) shows the calculated nitrogen distribution which is obtained using the same kinetic parameters used in the calculation of Fig. 3.15(a), but also including the effects of a reversible nitridation reaction, i.e. the reverse of reaction (3.4) is allowed to occur, as discussed in Section IV. Somewhat better agreement between experiment and the simulation is obtained assuming the nitridation is reversible. However, this assumption results in a calculated nitrogen distribution at a nitridation temperature of

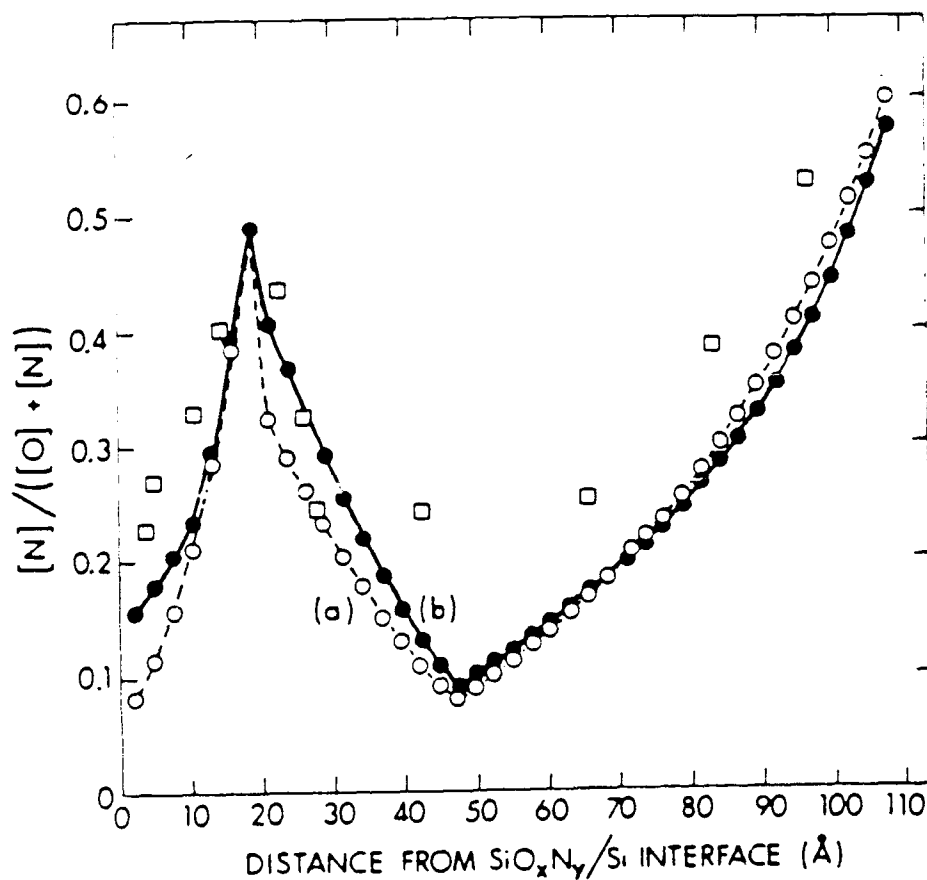


Figure 3.15. Comparison of the experimental nitrogen distribution in a SiO_xN_y film, produced from a 100 \AA -thick SiO_2 film nitrified for 10 minutes at 1150°C (squares, from Fig. 3.4(b)), to the calculated nitrogen distribution (a) using the same kinetic parameters as in Fig. 3.13(d), and (b) including the effects of a reversible nitridation.

1000°C which agrees less well with the experimental nitrogen distribution, as shown in Fig. 3.16. The data shown in Figs. 3.14 and 3.15 can be seen to be most consistent with an irreversible nitridation. The results of the kinetic model thus suggest that the energy barrier for the reverse of reaction (3.4) has been increased relative to the forward reaction, making oxidation of a nitrated oxide less likely. This suggestion is consistent with the known oxidation resistance of nitrated oxides.^{50,52,53,60}

The possibility that the nitridation kinetics are different above and below ~900°C introduces more uncertainty into the calculation of nitrogen distributions at low temperatures. Figure 3.17(a) shows the calculated nitrogen distribution for a 60 minute nitridation at a nitridation temperature of 800°C, using kinetic parameters which are appropriate for low temperature nitridation, as discussed in Section IV.C. Also shown in Fig. 3.17 are the experimental nitrogen distributions from Fig. 3.5(a) for two films nitrated at the same conditions. For comparison, Fig. 3.17(b) shows the calculated nitrogen distribution using the same kinetic parameters used at higher temperatures. Both sets of parameters result in calculated nitrogen distributions which predict a key feature of the measured nitrogen distribution: the peak interfacial nitrogen concentration occurs at the interface and does not occur away from the interface for long nitridation times, as at higher temperatures. At this low nitridation temperature, the probability of reaction (3.4) occurring is lowered so that more nitrogen diffuses to the dielectric/substrate interface. Sufficient nitrogen reacts with the substrate to form a diffusion barrier before a significant amount of diffusing oxygen is released by the slower substitution reaction occurring in the oxide. The quantitative

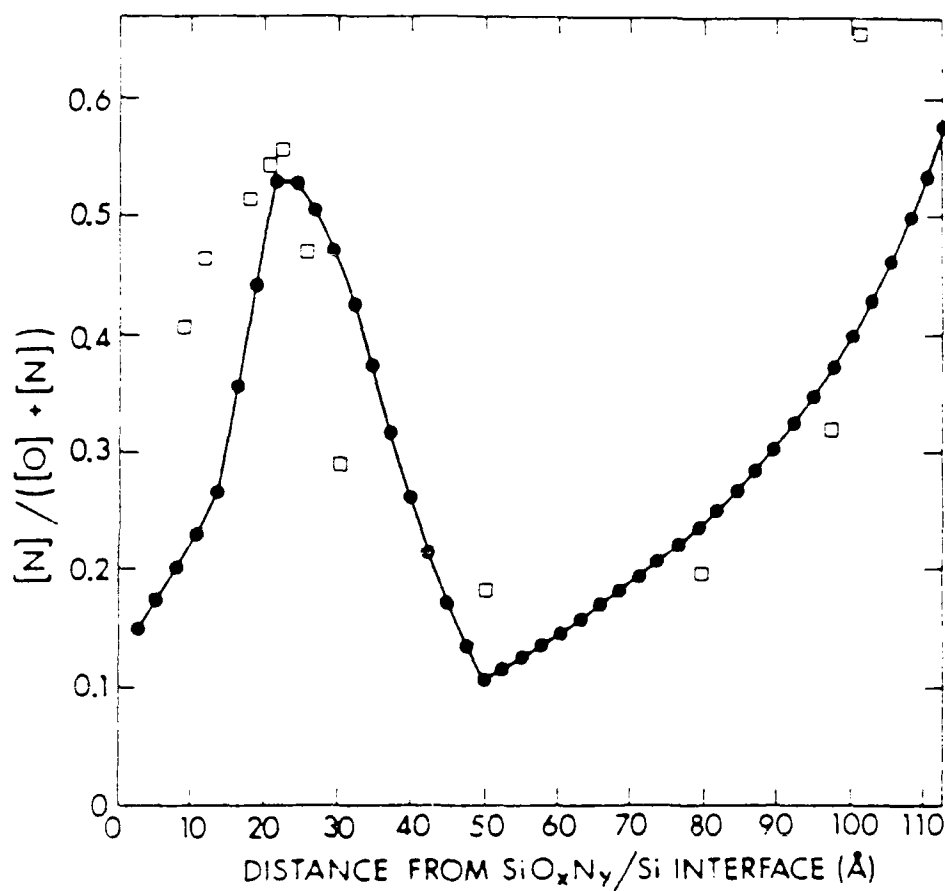


Figure 3.16. Comparison of the experimental data points from Fig. 3.3(b) (squares) to the calculated nitrogen distribution using the same kinetic parameters as in Fig. 3.15(b) for a 30 minute nitridation at 1000°C.

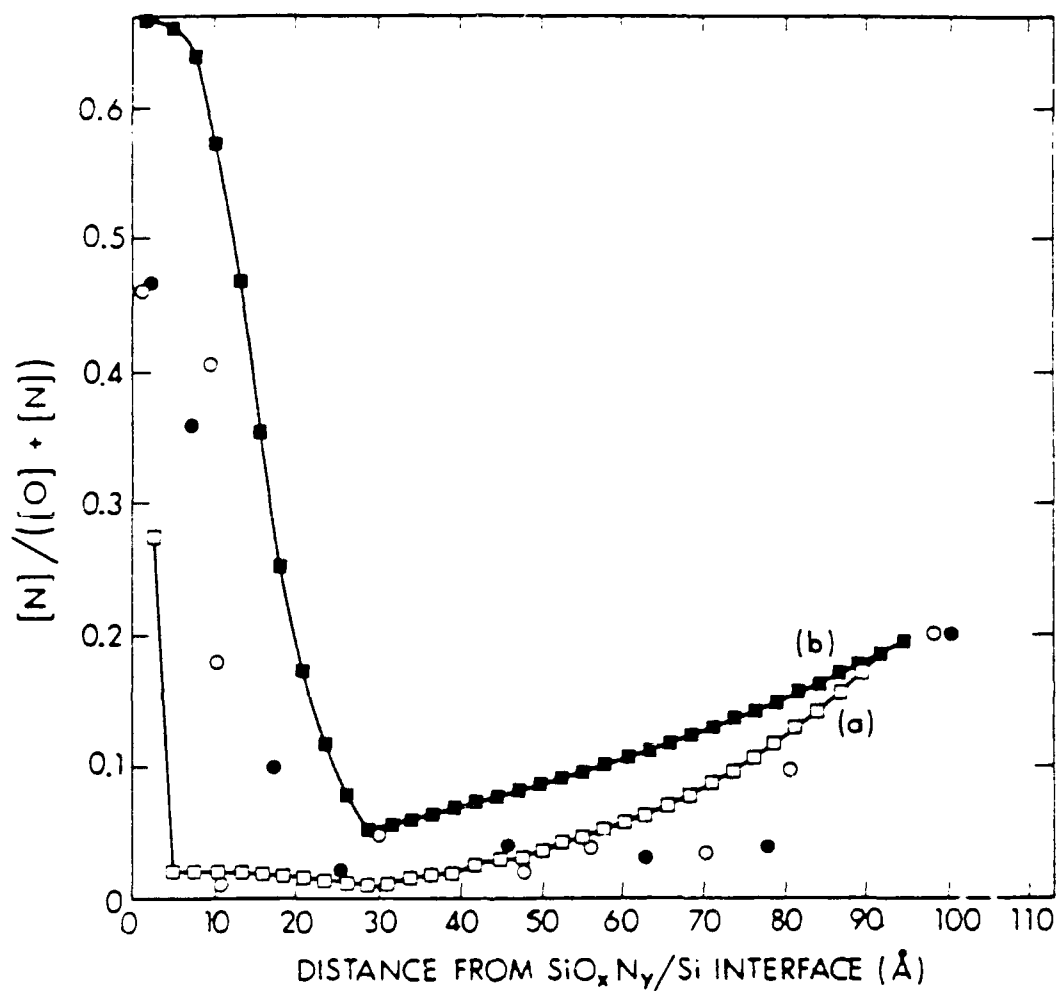


Figure 3.17. Comparison of the experimental nitrogen distribution in SiO_xN_y films, produced from 100 Å-thick SiO_2 films nitrided for 60 minutes at 800°C (solid and open circles, from Fig. 3.5(a)), to the calculated nitrogen distribution (a) using kinetic parameters appropriate for low temperature nitridation, and (b) using kinetic parameters appropriate for high temperature nitridation.

discrepancy between Fig. 3.17(b) and the measured nitrogen distribution suggests that the nitridation kinetics are indeed different above and below $\sim 900^{\circ}\text{C}$. However, the quantitative discrepancy between Fig. 3.17(a) and the measured nitrogen distribution is an indication that the low temperature kinetic parameters are not optimized. The most likely source of error is the assumption that R_0 for the various reactions does not vary with temperature, even though ΔE_A does vary.

The calculated nitrogen distributions shown in Figs. 3.12 to 3.17 were all using an initial SiO_2 thickness near 100 \AA . The effect of increasing oxide thickness is shown in Fig. 3.18 for a 30 minute nitridation at 1000°C . The peak interfacial nitrogen concentration is seen to decrease in magnitude and occur closer to the interface with increasing initial oxide thickness. This trend, together with the reduced interfacial nitrogen incorporation at higher temperatures previously discussed, may explain the failure to observe⁵⁰ an interfacial nitrogen buildup for a 500 \AA oxide nitrided at 1200°C . The magnitude of the decrease shown in Fig. 4.18 is likely to be larger than what would occur experimentally, however, since an interfacial nitrogen buildup is clearly evident⁶⁷⁻⁶⁹ in 400 \AA thick oxides which have been nitrided at 1100°C .

In addition to the quantitative discrepancies noted above for low nitridation temperatures, quantitative discrepancies between the data and the results of the simulations are apparent in the higher temperature nitridations shown in Figs. 3.14 and 3.15. The nitrogen concentration in the bulk (between the surface and interfacial peaks in nitrogen concentration) of the film is generally underestimated, especially for long nitridation times. In the simulations, after sufficient nitrogen has incorporated in the surface layer of

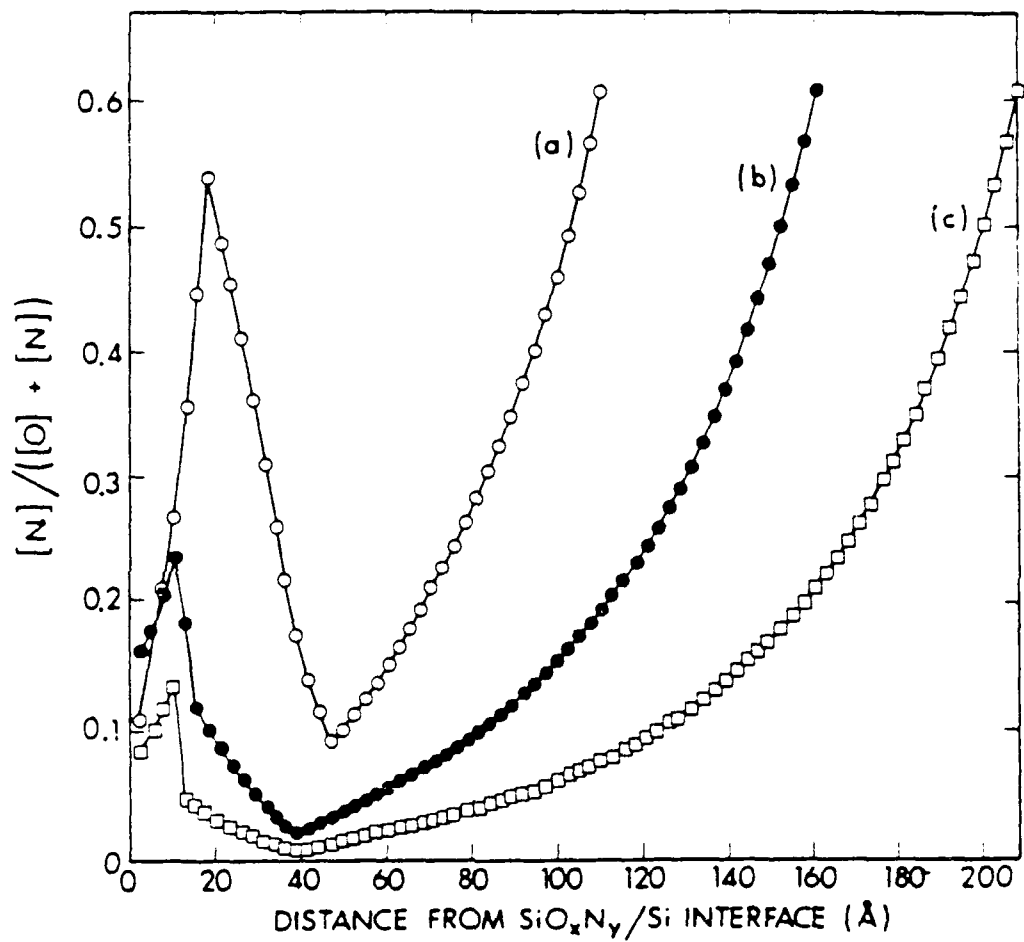


Figure 3.18. Calculate nitrogen distribution using the same kinetic parameters as Figure 3.13(d) for a 30 minute nitridation at 1000°C for an initial oxide thickness of (a) 100 Å, (b) 150 Å, and (c) 200 Å.

the nitrated oxide, no additional diffusing nitrogen can enter the oxynitride film from the gas phase and the distribution of nitrogen in the film reaches the steady state. Experimentally, however, nitrogen incorporation continues in the bulk of the film even after the N distribution in the interfacial region and the surface N concentration cease to change.^{14-17,67-69} This may indicate that the heavily nitrated surface layer is too thin to be an effective diffusion barrier, whereas in the simulations only a single layer (2.63 Å) of Si₂N₂O forms a perfect diffusion barrier. Another discrepancy is apparent in the interfacial region, where the simulations show the nitrogen concentration decreasing more rapidly than is experimentally observed in the region between the interface and the maximum in the interfacial nitrogen concentration. Preferential etching could account for this discrepancy if the distribution of nitrogen is laterally nonuniform, since the available experimental evidence shows that a higher nitrogen concentration lowers the etch rate. Nitrogen-rich regions would then etch last, skewing the distribution towards the interface. Interfacial kinetics which differ from that assumed in this simple model may also cause the discrepancy.

V. Spectroscopic Ellipsometry Measurements

Spectroscopic ellipsometry measurements were taken on the samples which were prepared as summarized in Table I. Two different single-layer models were fit to data taken on sample 2. In the first, the SiO_xN_y layer was modeled as a mixture of SiO₂ and voids. The best fit obtained had a mean square error (MSE) of 5.8×10^{-4} with an oxide thickness $t_{ox} = 127$ Å when the void fraction f_v was fixed at 0. When f_v was allowed to vary, the best fit (MSE =

3.6×10^{-4}) was obtained with $t_{\text{ox}} = 112 \text{ \AA}$ and $f_v = -0.35$.

The second model considered the SiO_xN_y layer to be a physical mixture of SiO_2 and Si_3N_4 . It is to be noted that in this special case, a physical mixture is equivalent to a chemical mixture. This is because for both SiO_2 and Si_3N_4 absorption in the energy range of interest is dominated by the lone pair electrons on O or N,⁴⁸ rather than the bonding electrons. Within the second model, the best fit ($\text{MSE} = 1.3 \times 10^{-4}$) was obtained for $t_{\text{ox}} = 116 \text{ \AA}$ and a nitride fraction $f_N = 0.065$. For comparison, the MSE between two sets of data taken on the same sample was 1.4×10^{-4} .

Samples 1 to 9 can clearly provide no information on the interface, since the data can be well fit with a simple one-layer model. The lack of sensitivity can be traced to the thin dielectric film. For a thickness of 100 \AA , the phase difference between light reflected at the ambient/film and film/substrate interfaces is insufficient to cause the extinction of s-polarized light which gives rise to a peak in $\tan \psi$, and hence enhanced interfacial sensitivity. Nevertheless, a two-layer model has been used⁶⁴ on spectroscopic ellipsometry data taken on 200-\AA -thick nitrided oxides. However, f_v was the only new information measured, with the N fraction provided by RBS. For these thin dielectric films, spectroscopic ellipsometry is clearly insufficiently sensitive to determine the complex nitrogen distributions observed in nitrided oxides.

Figures 3.19 and 3.20 show the data taken on samples 10 and 11, as well as a sample taken from a wafer oxidized at the same time under the same conditions, but with no nitridation. Comparing the oxide curve in Figs. 3.19(a) and 3.20(a) to similar data presented elsewhere,⁴⁷ the major

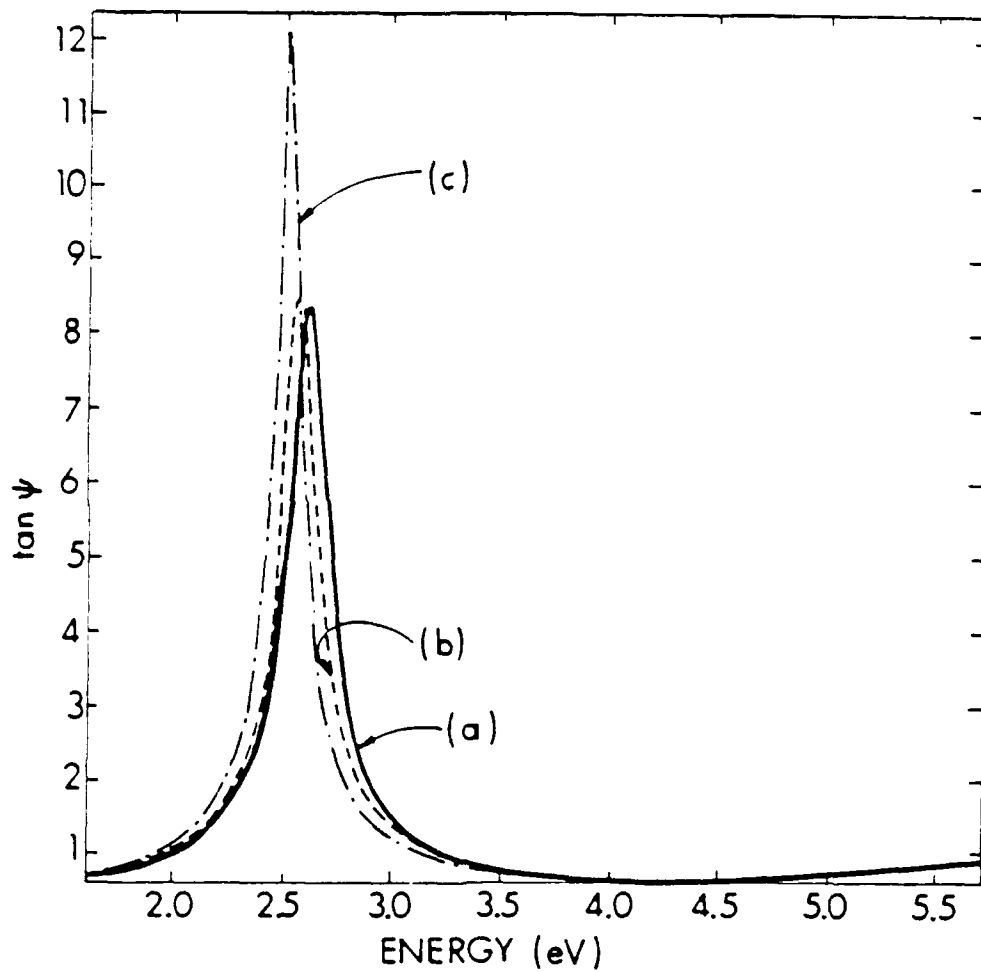


Figure 3.19. Spectra of $\tan \psi$ obtained for (a) a 1030 Å-thick layer of SiO_2 on Si, (b) a 1030 Å-thick layer of SiO_2 on Si, nitrified for 2 hours at 800°C, and (c) a 1030 Å-thick layer of SiO_2 on Si, nitrified for 2 hours at 1000°C.

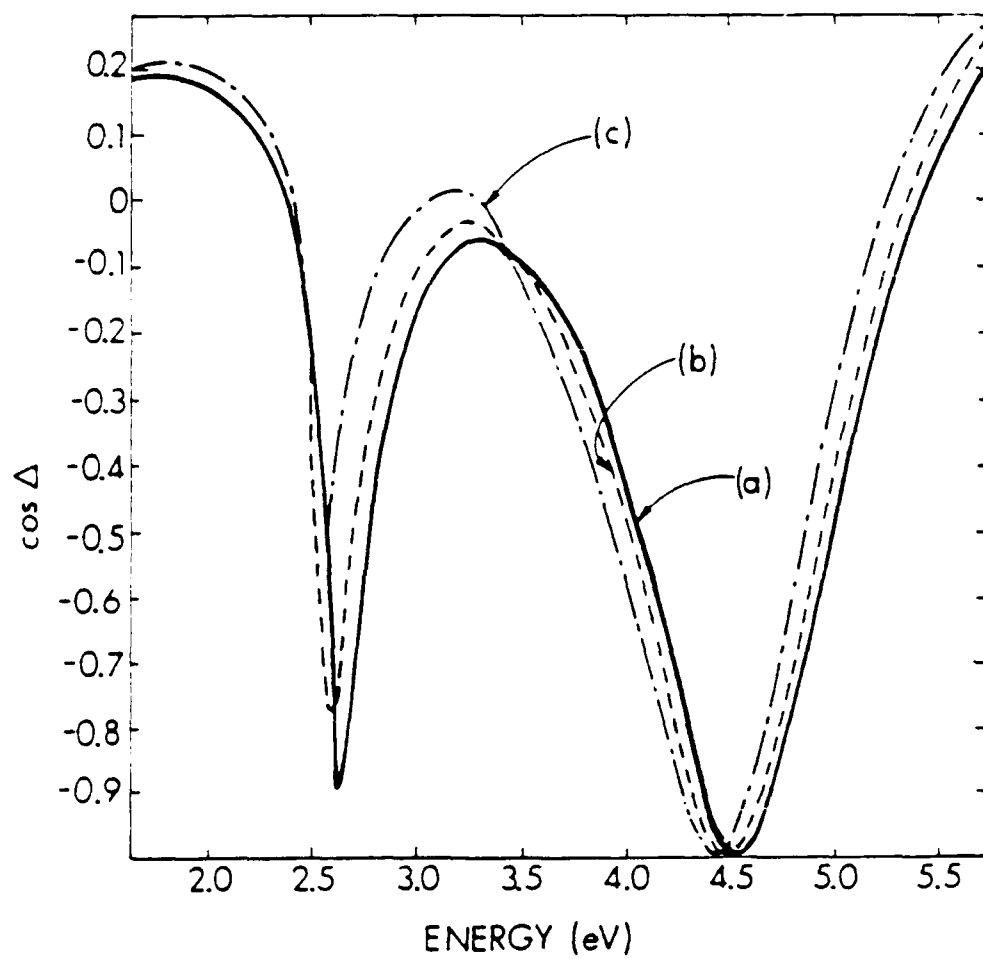


Figure 3.20. Spectra of $\cos \Delta$ corresponding to the data in Fig. 3.19.

qualitative discrepancy is that in Fig. 3.20(a), the minimum in $\cos \Delta$ near 2.6 eV does not reach -1. Such an observation has previously¹⁰³ been interpreted as evidence of thickness nonuniformity. The degree of thickness variation required, however, is several tens of Angstroms. This explanation seems unlikely for the device-quality thermal oxide sample used. As seen in Figs. 3.20(b) and (c), this situation becomes worse with an increasing degree of nitridation. Two possible causes are roughening of either the surface or interface, or laterally nonuniform nitrogen incorporation in the oxide. In this latter case, nitrogen-rich regions would have a higher index of refraction and would appear to be optically thicker than surrounding regions.

Several models were fit to the data taken on sample 11, shown in Figs. 3.19(c) and 3.20(c). A good fit could be obtained to $\tan \psi$ in all cases, so only the fit to $\cos \Delta$ will be shown. Figure 3.21 shows the result of fitting a single-layer model to the data, consisting of a physical mixture of SiO_2 and Si_3N_4 . The best fit ($\text{MSE} = 6 \times 10^{-3}$) was obtained for $t_{\text{ox}} = 1074 \text{ \AA}$ and $f_{\text{N}} = 0.034$. As can be seen, $\cos \Delta$ is not fit well near 2.5 eV. A fit to $\cos \Delta$ only yields $\text{MSE} = 6.65 \times 10^{-4}$, $t_{\text{ox}} = 1033 \text{ \AA}$, and $f_{\text{N}} = 0.091$. However, in this case $\tan \psi$ has a maximum value of 19.5, compared to the observed value near 12 in the data. Including additional layers in the model at the surface and near the interface with each layer allowed to have different values of f_{N} only marginally decreased the MSE (by $< 10\%$).

Figures 3.22 and 3.23 shows data taken on the same sample for two different aperture sizes. This technique was previously used¹⁰³ to demonstrate the effects of thickness nonuniformities. The aperture sizes used (for the aperture nearest the detector) were 0.6 mm and 2 mm. This

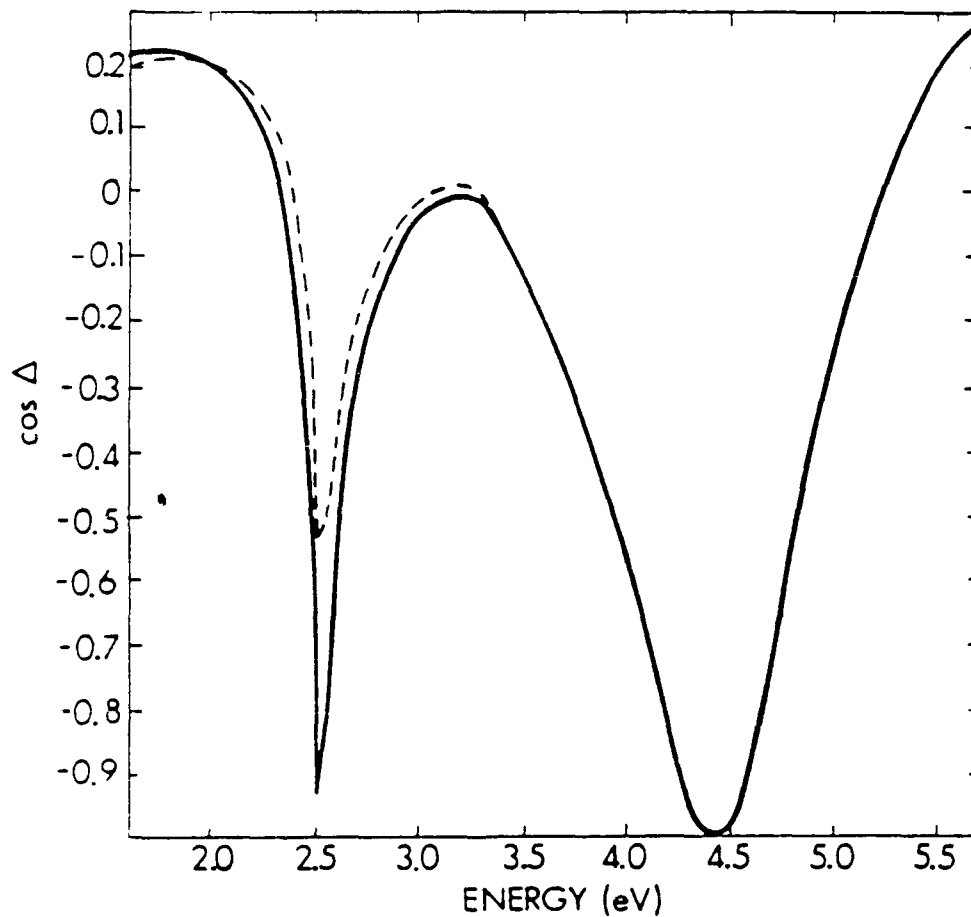


Figure 3.21. Best fit to the data from Figs. 3.19(c) and 3.20(c), obtained using a single-layer model in which the dielectric consists of a physical mixture of SiO_2 and Si_3N_4 . Only the fit to $\cos \Delta$ is shown, since $\tan \psi$ could be fit well enough that no difference between the data and the fit is apparent to the eye.

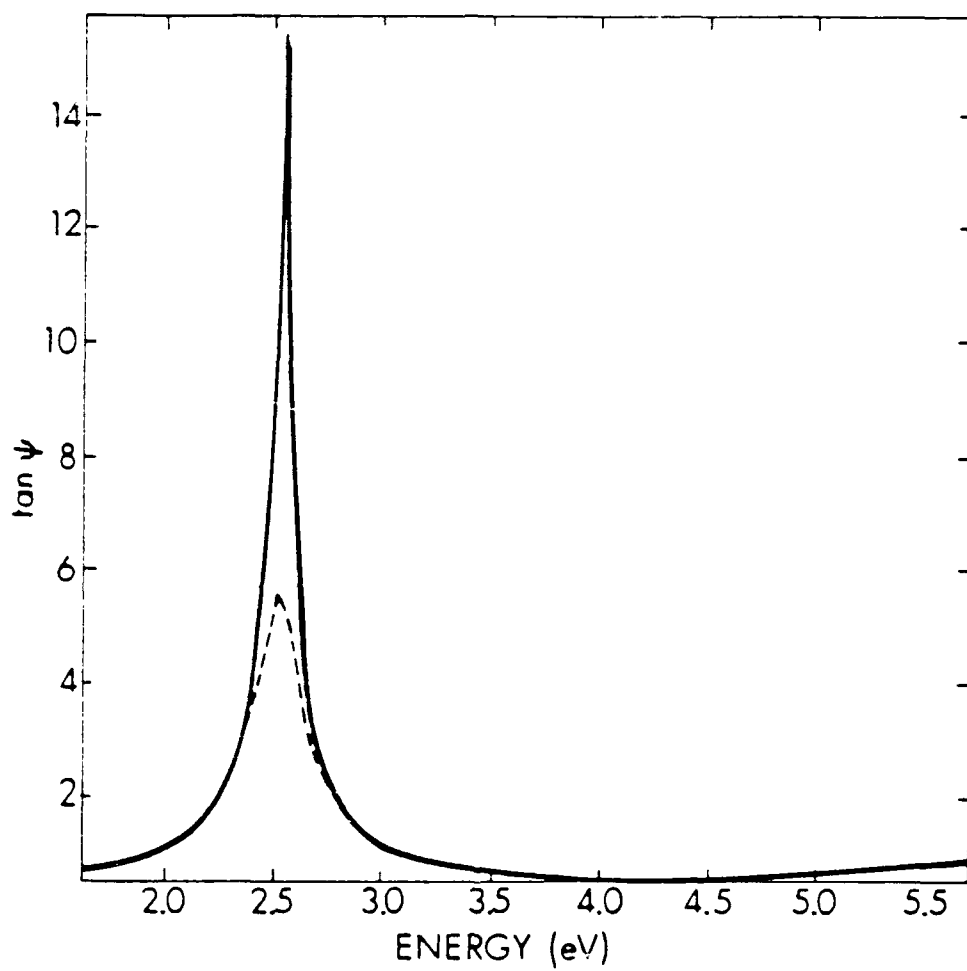


Figure 3.22. Comparison of $\tan \psi$ spectra obtained from sample 11 using aperture sizes of 0.6 mm and 2 mm.

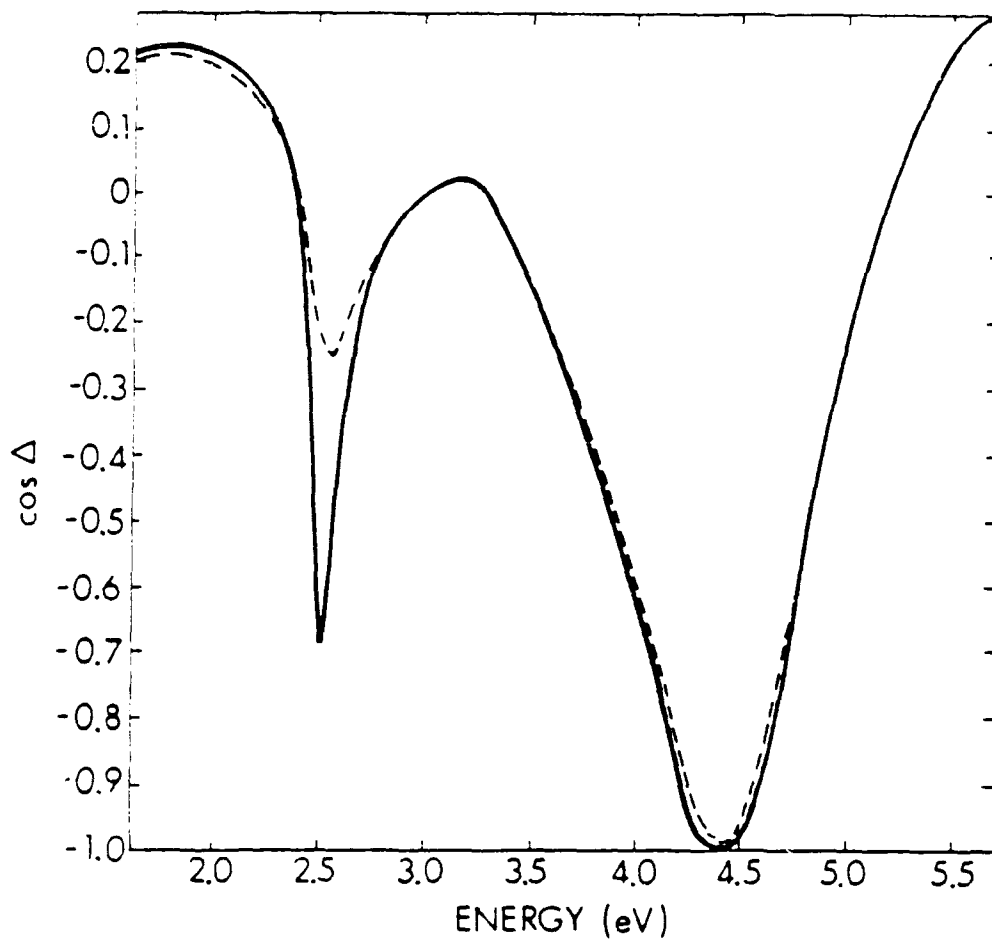


Figure 3.23. Comparison of $\cos \Delta$ spectra obtained from sample 11 using aperture sizes of 0.6 mm and 2 mm.

corresponds to a smaller spot on the sample, since the beam diverges between the sample and the detector. Some attempts were made to include the effects of nonuniformities in the modeling. Within a single-layer model, a Gaussian distribution of thicknesses about some mean value of t_{ox} was assumed. The best fit was for a Gaussian full width at half maximum of 26 Å, but the quality of the fit was not better than that shown in Fig. 3.21. A similar fit was attempted assuming nonuniformities in f_N , but no improvement in the fit could be obtained. It may be that the nonuniformities are greater than assumed, and the fits are not converging at the true minimum in the MSE. At this time, the data is not understood.

Some model data was calculated in order to determine limits on the usefulness of spectroscopic ellipsometry in the study of nitrided oxides, and to determine the usefulness of infrared ellipsometry in studying this material system. Figures 3.24 and 3.25 shows calculated spectra for a 1030 Å thick film on Si with $f_N = 0.1$ in the dielectric. As can be seen, $\tan \psi$ is a slowly varying function below 1.6 eV, and $\cos \Delta$ is rapidly varying. The MSE between these curves and similar curves calculated with a 15-Å-thick Si_3N_4 layer at the interface and reducing the bulk dielectric layer thickness by the same amount is 0.15. However, the differences are apparent primarily in the visible-UV region. There would thus appear to be no advantage to using infrared ellipsometry on this material system.

The calculated curve with the 15-Å-thick Si_3N_4 interface layer and a 1015-Å-thick bulk with $f_N = 0.1$ was fit with a single-layer model. The best fit had a $\text{MSE} = 5 \times 10^{-4}$, so the interface is detectable. The two-layer calculated curve was compared to a three-layer calculated curve in which the interface

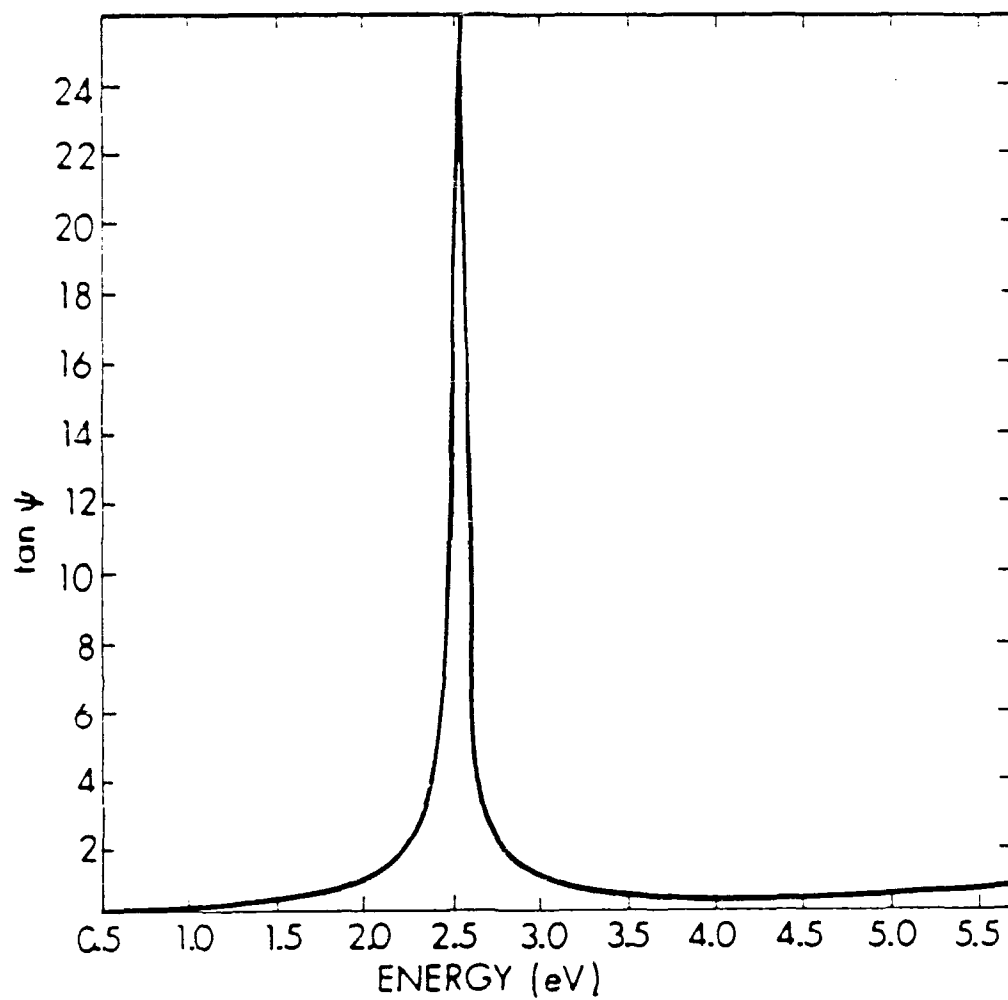


Figure 3.24. Calculated spectrum of $\tan \psi$ for a 1030 Å-thick dielectric on Si, consisting of a physical mixture of 10% Si_3N_4 and 90% SiO_2 , in the energy range 0.5-5.7 eV.

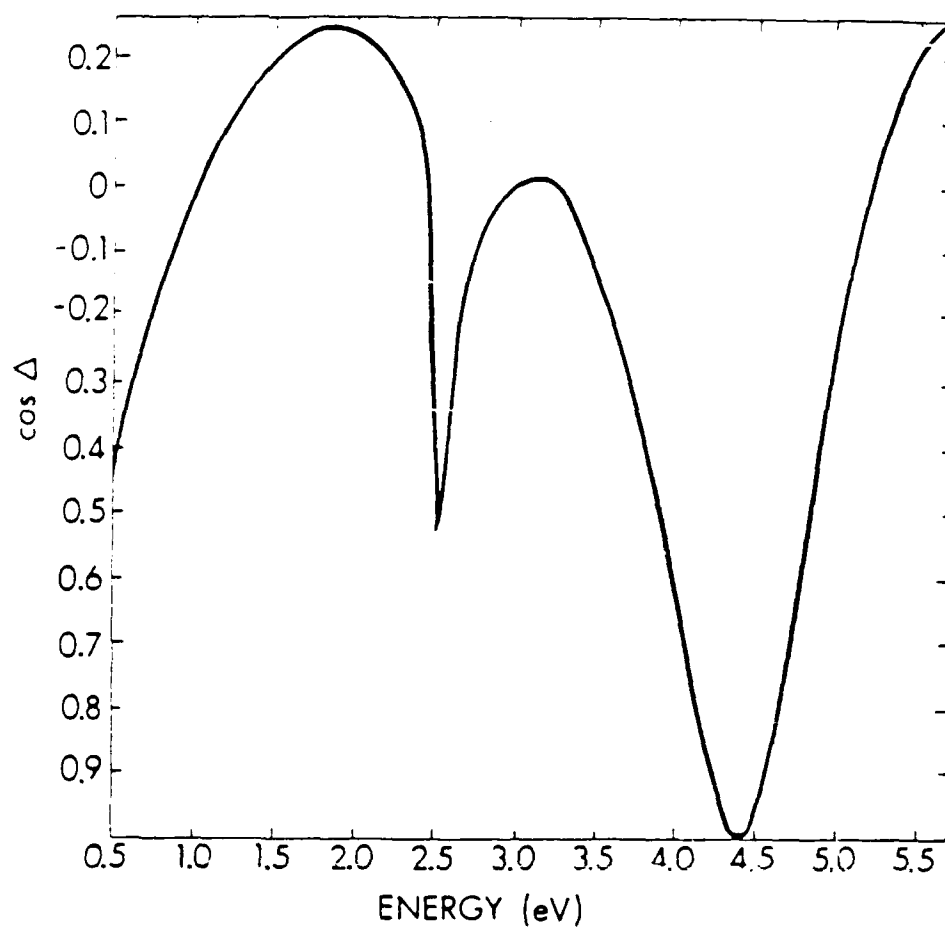


Figure 3.25. Calculated spectrum of $\cos \Delta$ for a 1030 Å-thick dielectric on Si, consisting of a physical mixture of 10% Si_3N_4 and 90% SiO_2 , in the energy range 0.5-5.7 eV.

consisted of 15 Å of Si_3N_4 on top of 15 Å of SiO_2 . The MSE was 3.7×10^{-3} . However, when a two-layer model was fit to the three-layer calculated curve, the MSE was 5×10^{-6} , well below the noise level. Spectroscopic ellipsometry would thus not be capable of distinguishing a nitride-rich interface from a nitrogen-rich region separated from the interface by an oxygen-rich region. Both of these structures occur in the nitrated oxides, depending on the nitridation conditions. Spectroscopic ellipsometry would thus appear to be of limited usefulness in studying nitrated oxides.

VI. Summary and Conclusions

In summary, the thermal nitridation of SiO_2 films on Si has been studied by measuring the nitrogen concentration depth profiles with XPS as a function of oxidation temperature and nitridation time and temperature. The peak interfacial nitrogen concentration initially occurs at the $\text{SiO}_x\text{N}_y/\text{Si}$ interface, then appears to move away from the interface with increasing nitridation time for sufficiently high nitridation temperatures. The behavior of $|\Delta V_{\text{FB}}|$ correlates well with the observed nitrogen distributions. This correlation is shown to consistently follow from the simple postulate that it is the strain-dependence of the kinetics of formation of defect states which allow lowering of the system energy by relieving interfacial strain. The distribution of defects is deduced from the intensity of a fluorine marker, and is found to be consistent with the proposed model explaining the behavior of flatband voltage shifts as a function of nitridation conditions. Macroscopic intrinsic stress is not observed to affect the nitrogen distribution, but does affect the defect formation kinetics.

Modeling of the kinetics of the nitridation of SiO_2/Si in NH_3 has been done in this study, and reveals a mechanism in which diffusing species, initially consisting primarily of the nitrogen species, react with the substrate, forming a nitrogen-rich oxynitride at the interface. At sufficiently high nitridation temperatures, an oxygen-rich oxynitride subsequently forms at the interface due to reaction of the substrate with an increasing concentration of diffusing oxygen which has been displaced by the slower nitridation of the dielectric. The data are consistent with the mechanism discussed above, provided the influence of the interfacial strain on the nitridation and oxidation kinetics is explicitly accounted for. The fact that the XPS data qualitatively confirm the predictions of the kinetic model is an indication that the essential physics of the nitridation process is contained in the model, although quantitative discrepancies indicate that the kinetic parameters are not yet optimized. In spite of the discrepancies, the model successfully predicts that (a) the maximum nitrogen concentration in the interfacial region initially occurs at the interface and occurs away from the interface with increasing nitridation time at sufficiently high nitridation temperatures, (b) the maximum nitrogen concentration in the interfacial region remains at the interface even for long nitridation times at low nitridation temperatures, and (c) the peak interfacial nitrogen concentration is lower for the highest nitridation temperature studied. The simulations provide valuable insight into the reasons for these experimentally confirmed observations, and also provide insight into the role of interfacial strain in the nitridation kinetics.

Chapter 4

Studies of Semiconductor-on-Insulator (SOI) Structures

I. Introduction

Semiconductor-on-insulator (SOI) structures consisting of Si/SiO₂/Si are a potentially low-cost alternative to silicon-on-sapphire structures. Such structures show promise in high-speed complementary metal-oxide-semiconductor (CMOS) devices with applications in radiation hard electronics and VLSI circuits. The formation of SOI structures can be accomplished in several ways. Two techniques have been studied as part of this task: ion implantation and zone-melting recrystallization (ZMR).

The formation of SOI structures by ion implantation involves the high dosage implantation of ions into a single crystal Si substrate. Heating the substrate during the implantation (typically to 500° C) aids both the redistribution of the implanted species and the annealing of implantation damage in the Si surface layer and the Si substrate. A subsequent high temperature anneal, during which the implanted species react with the Si, forms the buried insulator layer. The implanted species can be oxygen to form a buried SiO₂ layer,^{19-22,106-108} nitrogen to form a buried Si₃N₄ layer,¹⁰⁹⁻¹¹² or both species to form a buried SiO_xN_y layer.¹¹³ The post-implantation annealing temperature is typically 1100° C to 1300° C, though recently excellent results have been obtained at 1405° C.¹⁰⁷ In addition to chemical, electrical, and morphological characterizations,^{19-22,106,107,109-113} the formation of SOI structures by ion implantation has also been modeled.¹⁰⁸

in this work, the morphology of the buried SiO_2/Si interfaces has been studied by SEM, and the chemical structure of the interface of thermally grown SiO_2 on the surface Si has been studied by XPS. These studies are described in section II.

The formation of SOI structures by ZMR involves the deposition of polycrystalline Si onto a SiO_2 layer which has been thermally grown on a single crystal Si substrate. A SiO_2 capping layer is deposited, and a graphite strip heater is passed over the structure to melt the poly-Si layer, which when cooled recrystallizes to form a single crystal Si layer. Experimental measurements²³ and modeling¹¹⁴ of the formation of such structures have been done. It has been reported²³ that nitridation of the capping layer improves the quality of the recrystallized layer. It has been suggested²³ that the introduction of nitrogen at the capping $\text{SiO}_2/\text{deposited Si}$ interface improves the wetting of the capping layer by the Si when it is melted. However, attempts to detect nitrogen at the capping $\text{SiO}_2/\text{deposited Si}$ interface have not been successful.²³ In this work, XPS is used in an attempt to detect the possible presence of nitrogen at the interface. The results of these studies is reported in section III.

II. SOI Formed by Ion Implantation

Four SOI samples formed by ion implantation were obtained from Dr. Peter Hemment of the University of Surrey, England. The sample preparation is described elsewhere.¹⁹⁻²² All of the samples were implanted with a dosage of $1.8 \times 10^{18} \text{ cm}^{-2}$ oxygen ions with an implantation energy of 200

keV. The implantation temperature for two of the samples was 500°C. One was subsequently annealed at 1150° C for two hours, while the other recieved no further processing. The purpose of studying these two samples is to determine the effects of annealing. The other two samples were both annealed at 1150° C for two hours; the implantation temperature for one was 425° C and for the other was 525° C. The purpose of studying these two samples is to determine the effect of varying implantation temperature.

Prior to any further processing, the surfaces of all four samples were studied using XPS and SEM. Both the XPS and SEM data suggest that the surface Si film is good quality single crystal Si, as discussed below. The SEM micrographs show no evidence of grains, which would have been an indication of polycrystalline material, suggesting that the surface Si layer is either single crystal or amorphous. However, SEM micrographs taken at glancing angles (70° from the normal to the sample surface) do show evidence of varying degrees of surface roughness, apparent as small "hillocks" on the surface approximately 100 Å in diameter, as shown in Fig. 4.1. The XPS data show substantial differences in the native oxides on these samples. Figure 4.2 shows the Si 2*p* region of the photoelectron spectrum, showing both the substrate (near 100 eV) and oxide (near 104 eV) peaks. The substrate peak shape is consistent with the surface Si layer being single crystal, and does not show the broadening exhibited⁴⁴ by amorphized Si. Differences in oxide thicknesses are exhibited in the differing oxide/substrate intensity ratios, and differences in native oxide stoichiometry are exhibited in the differing oxide-to-substrate energy separations and oxide peak shapes. It

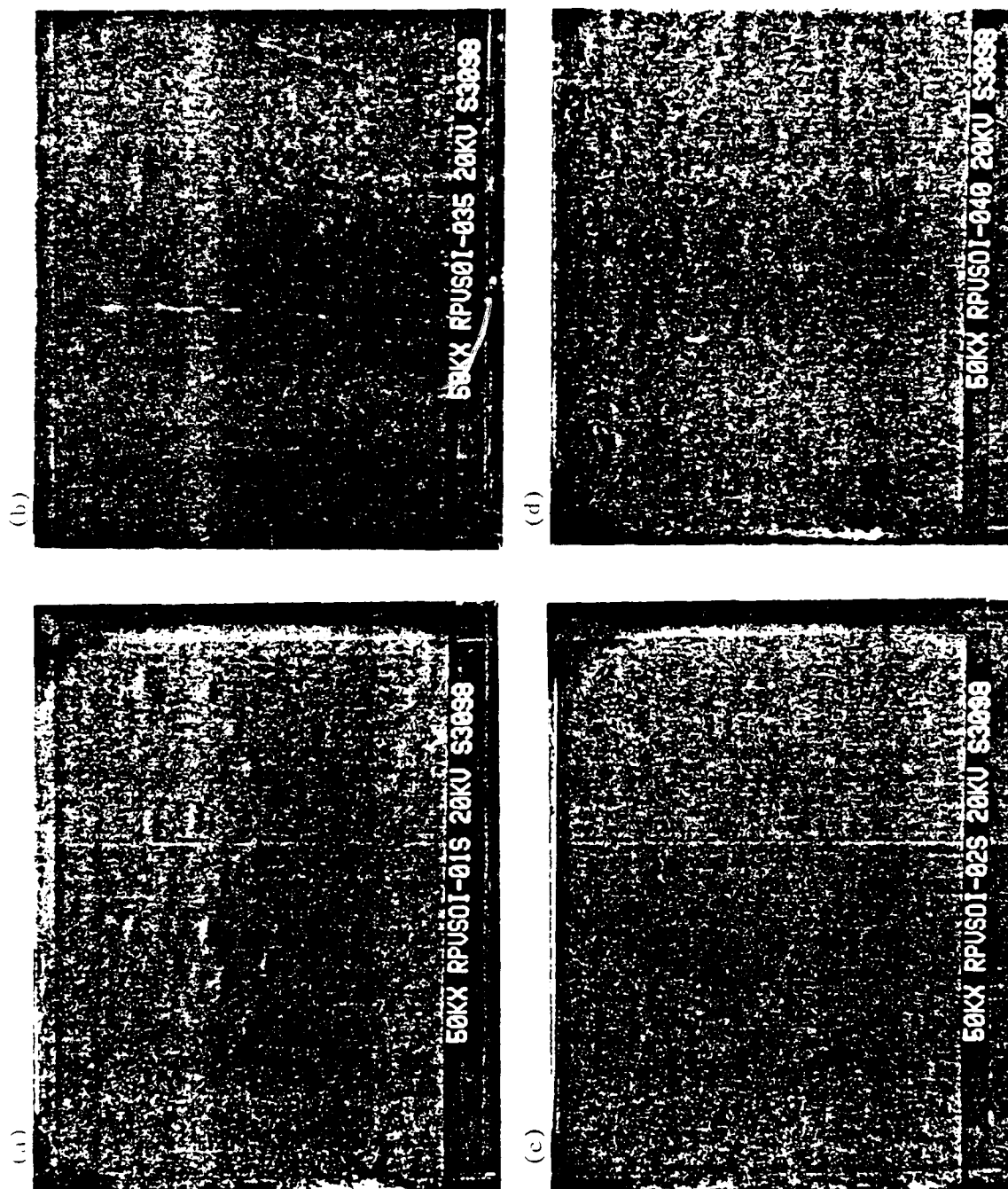


Figure 4.1. SEM micrographs of the surfaces of SOI samples formed by ion implantation of oxygen at (a) 500°C, no anneal, (b) 425°C, 2 hour 1150°C post-implantation anneal, (c) 500°C, 2 hour 1150°C anneal, and (d) 525°C, 2 hour 1150°C anneal.

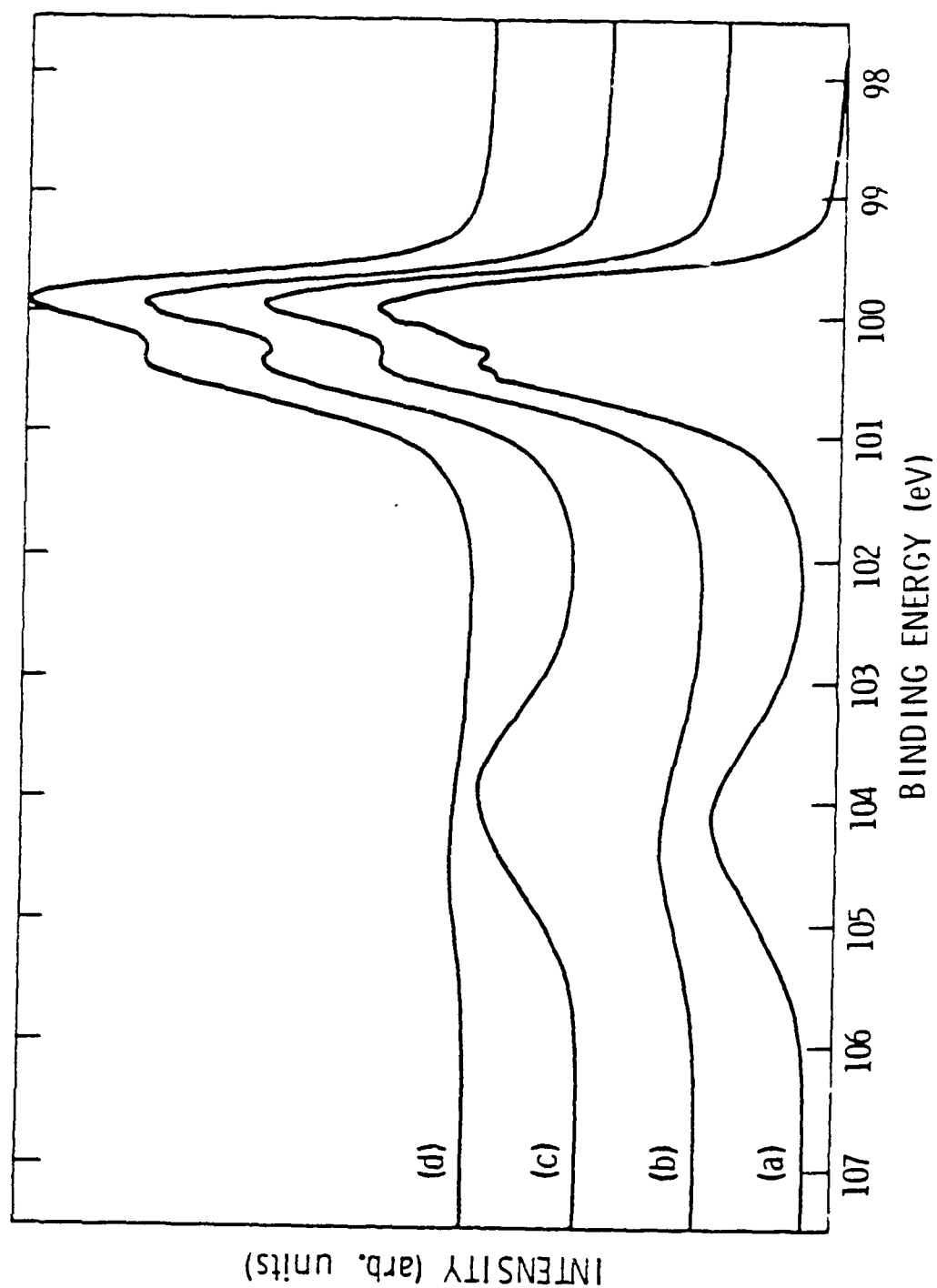


Figure 4.2. XPS spectra of the Si 2p region for the samples corresponding to the data in Fig. 4.1.

has been suggested¹¹⁵ that the suboxide distribution at the SiO_2/Si interface is affected by the surface step density. The native oxide stoichiometry may thus prove useful as a measure of the perfection of the crystalline surface.

The buried SiO_2 layer has also been studied with both XPS and SEM. The buried oxide/surface Si and buried oxide/substrate interfaces were exposed by etching away the surface Si layer and buried oxide layer, respectively. The etching technique used for removing the surface Si layer was the XeF_2 etching described briefly in Chapters 2 and 3 and in more detail elsewhere.^{37,38} The SEM micrographs of the buried SiO_2 /surface Si interface exposed in this way are shown in Fig. 4.3. Figure 4.4 shows the corresponding SEM micrographs at a higher resolution. The SEM micrographs for the unannealed sample, shown in Figs. 4.3(a) and 4.4(a), show a smooth surface, as expected if the oxygen implantation profile is laterally uniform. Figures 4.3(b) through (d) and 4.4(b) through (d) are the SEM micrographs showing the effect of increasing implantation temperature. Figures 4.3(b) and 4.4(b) show the roughest interface, indicating that for the low implantation temperature used (425°C), the redistribution of implanted oxygen is too slow to form a well-defined buried oxide with sharp interfaces. Figures 4.3 (c) and (d) and 4.4(c) and (d) show progressively smoother interfaces with increasing implantation temperature. The difference between micrographs (c) and (d) in both Figs. 4.3 and 4.4 seems surprising at first glance, since the implantation temperatures differ by only 25°C . However, the implantation temperature range 500° to 550°C is critical in determining the nature of the surface Si/buried SiO_2 interface. Below 500°C , the Si

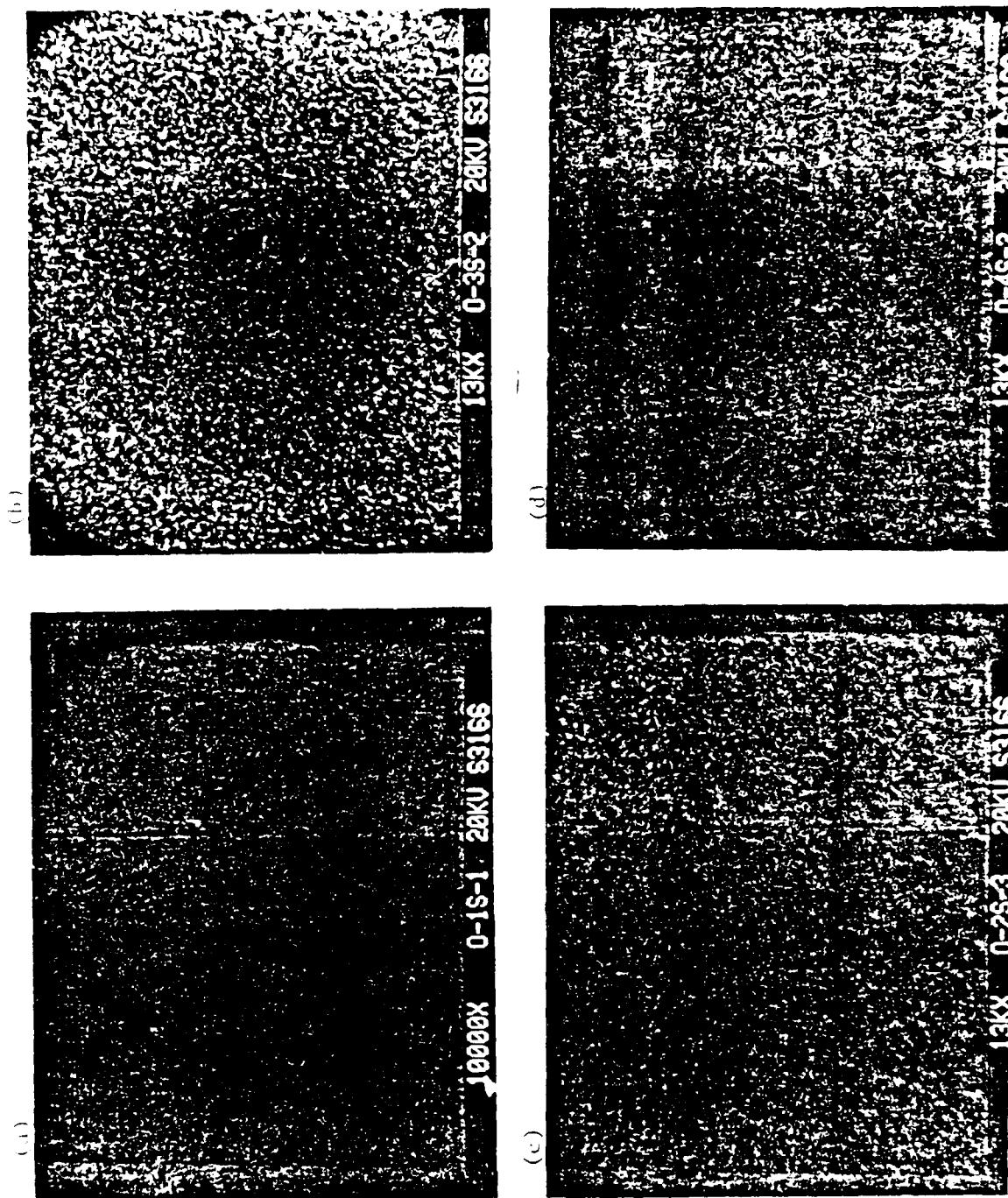


Figure 4.3. SEM micrographs (magnification 10-13kx) of the surfaces of SOI samples formed by ion implantation of oxygen at (a) 500°C, no anneal, (b) 425°C, 2 hour 1150°C post-implantation anneal, (c) 500°C, 2 hour 1150°C anneal, and (d) 525°C, 2 hour 1150°C anneal. The surface Si layer has been removed by XeF_2 etching, exposing the buried oxide.

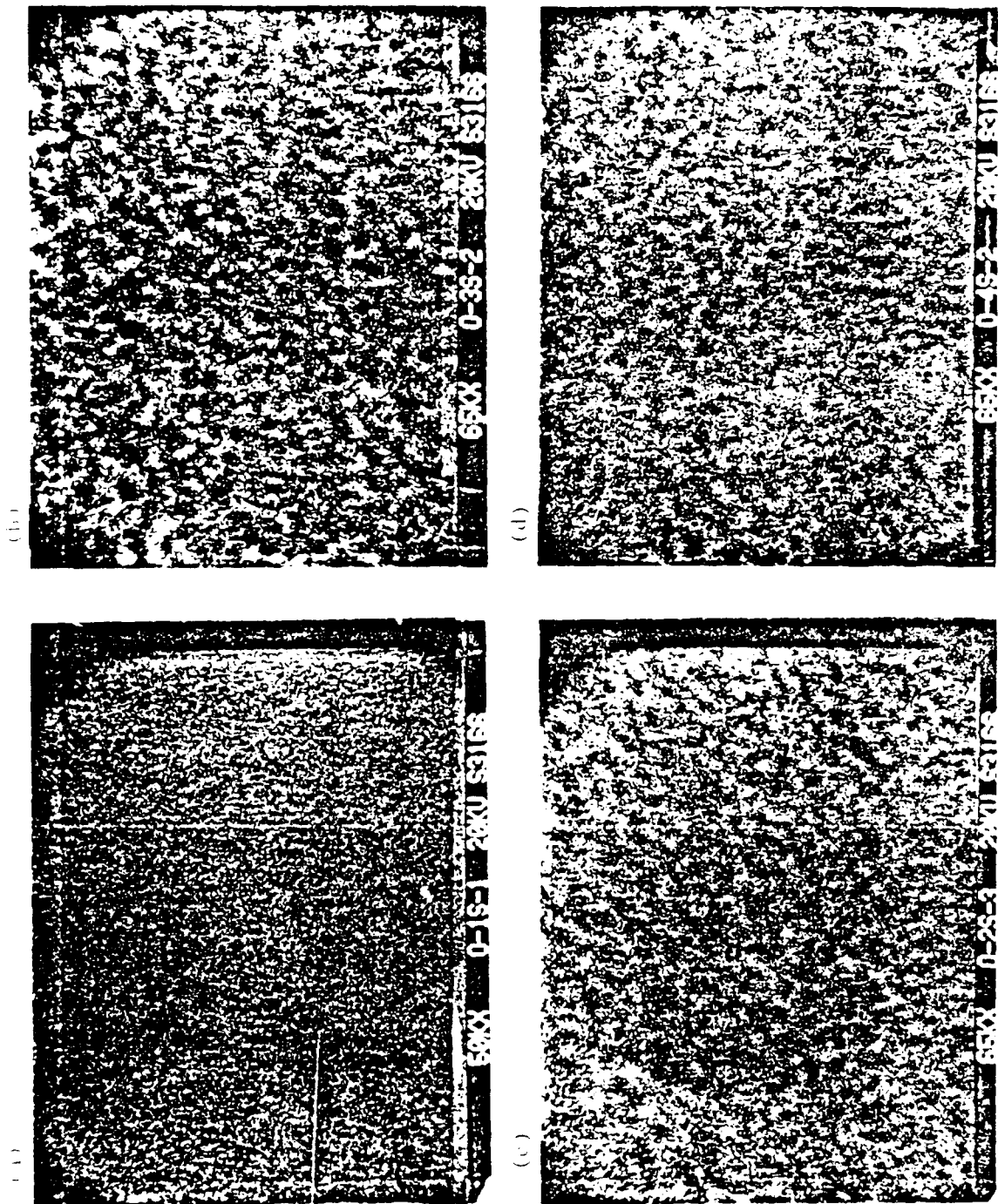


Figure 4.4 Same as Fig. 4.3, but with a magnification of 65kx.

nearest that interface is amorphous, while above 550° C it is best described as defected crystalline.¹¹⁶ In view of this, the differences apparent in Figs. 4.3 and 4.4 are not unreasonable. The XPS data taken on these samples were not considered reliable due to sample charging, a consequence of the thickness of the insulator layer.

After the studies discussed above, the buried SiO₂/substrate interface was exposed by removing the buried SiO₂ layer with HF. The SEM micrographs shown in Figs. 4.5 and 4.6 show the same trends noted above for the surface Si/buried SiO₂ interface, *i. e.* the interfaces are smoother at higher implantation temperatures. The XPS data show the unannealed sample to have a Si 2*p* lineshape which is characteristic of amorphous Si,⁴⁴ while the three annealed samples all exhibited lineshapes characteristic of crystalline Si. Only trace amounts of oxygen (corresponding to a few percent of a monolayer) were detected, probably from residual surface contaminants. However, the samples appeared visually to have a thick dielectric layer, exhibiting the colors typical of optical interference effects. The optical interference indicates a surface layer with an index of refraction which differs from that of the underlying Si substrate. Subsequent XeF₂ etching, however, removed the remainder of the samples, indicating no continuous SiO₂ layer was present. Some possible causes of the optically distinct surface layer include surface roughness, a region of defected Si, or a region with a relatively high concentration of oxygen or SiO₂ inclusions.

In devices based on SOI structures, it is the quality of the thermally grown SiO₂/surface Si interface which is important in determining device

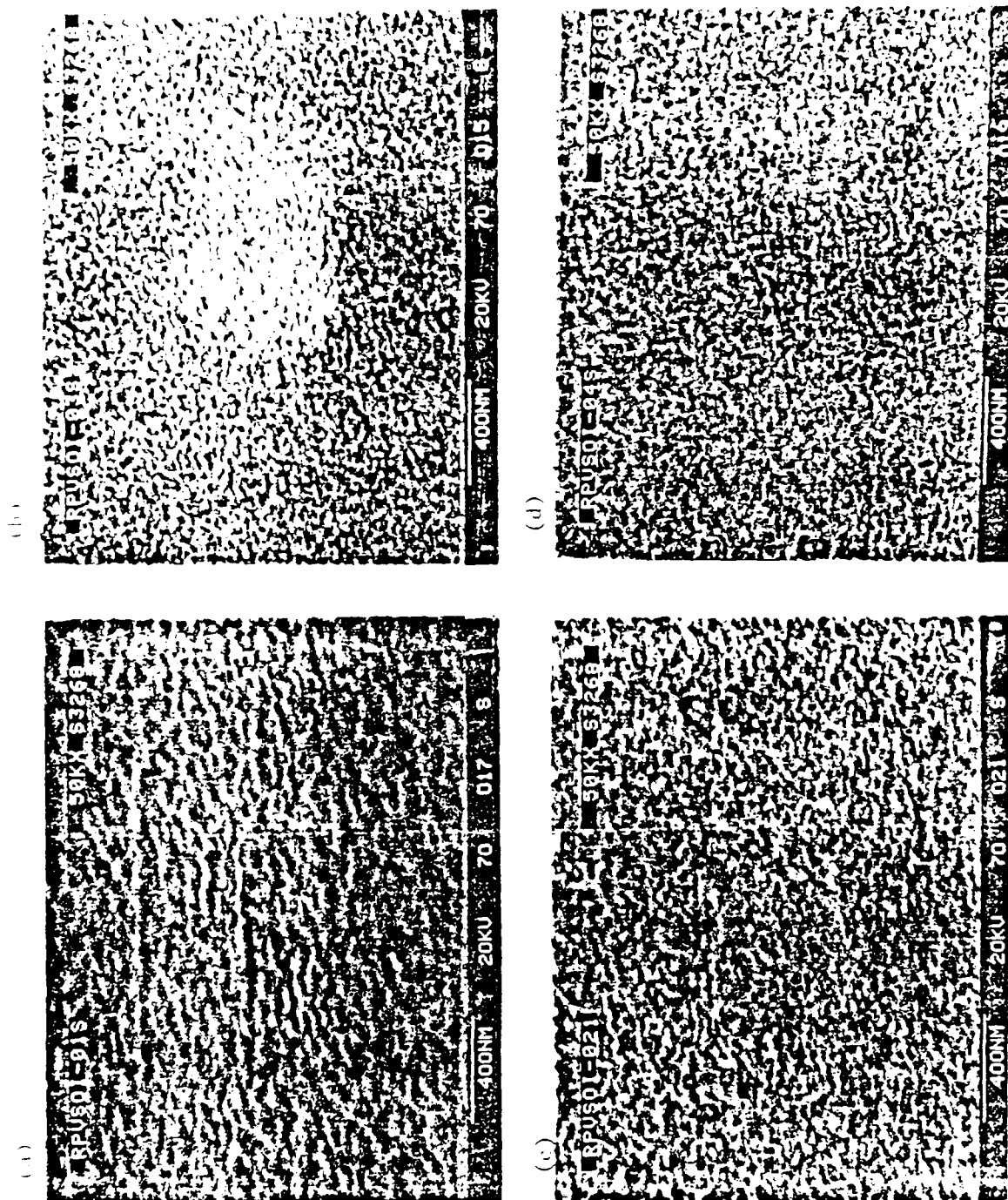


Figure 4.5 SFM micrographs (magnification 50kx) of the surfaces of SOI samples formed by ion implantation of oxygen at (a) 500 °C, no anneal, (b) 425 °C, 2 hour 1150 °C post-implantation anneal, (c) 500 °C, 2 hour 1150 °C anneal, and (d) 525 °C, 2 hour 1150 °C anneal. The surface Si layer has been removed by XeF_2 etching, and the buried oxide layer has been removed with HF, exposing the buried oxide substrate interface.

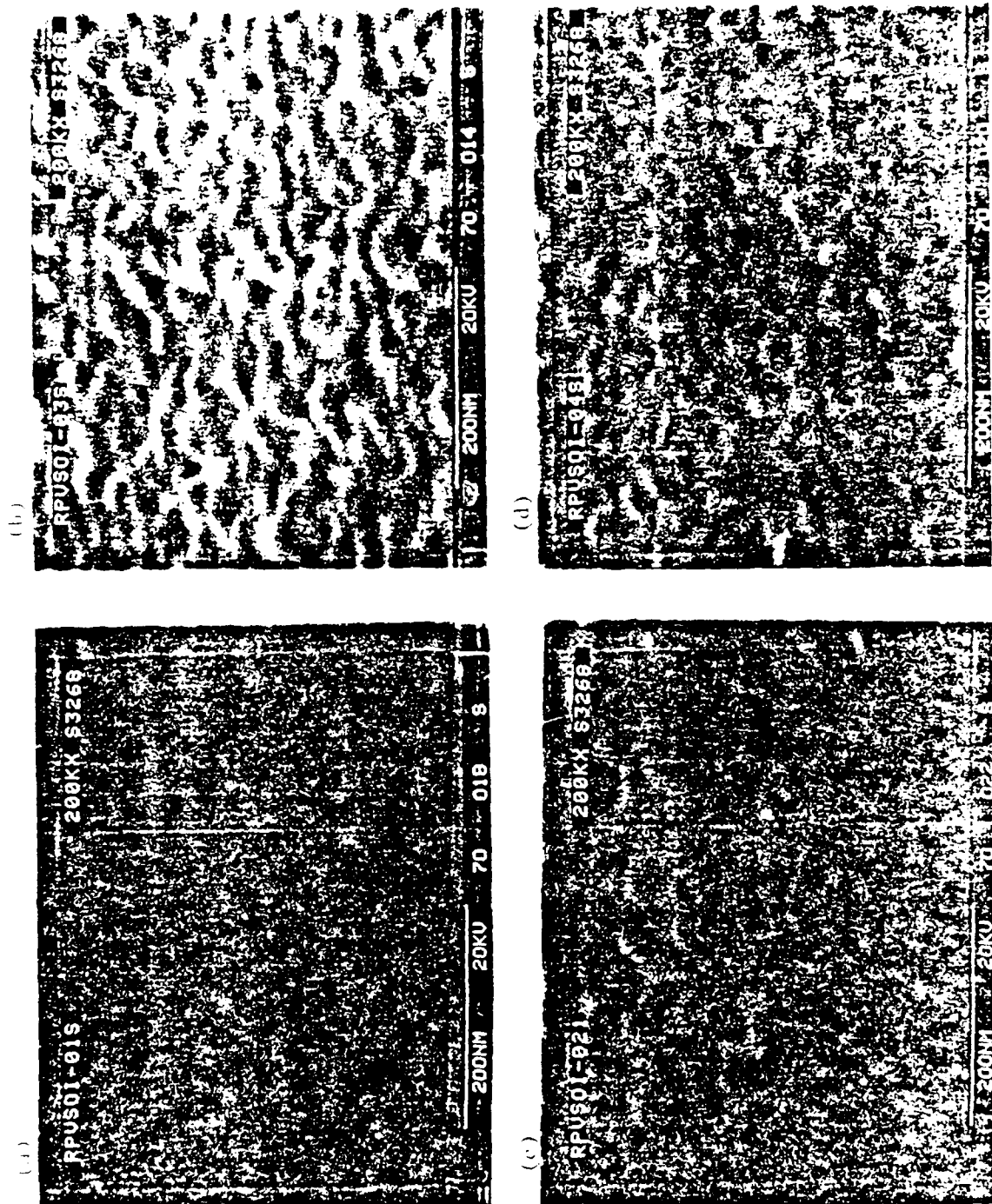


Figure 4.6 Same as Fig. 4.5, but with a magnification of 200kx

characteristics. Consequently, the samples which were implanted at 425° C and 525° C and annealed for two hours at 1150° C were oxidized in dry O₂ to give a SiO₂ layer approximately 80 Å thick. This oxide was then stripped with HF, and an 80-Å-thick SiO₂ layer was again thermally grown, which is the standard processing for device quality oxides. These thermally grown oxides were depth profiled using the sequential chemical etching technique described in Chapter 3 and elsewhere,^{1,35} with XPS spectra being recorded after each etch step. The thermally grown SiO₂/surface Si interfaces for the two samples appear to be identical within experimental error, which seems to be inconsistent with the previously noted differences in the native oxides. However, it is well known that oxidation tends to smooth the interface. These results suggest that even though the buried SiO₂ has interfaces with the Si substrate and surface Si layer with structures which depend fairly strongly on implantation temperature, the quality of the thermally grown SiO₂ and the SiO₂/surface Si interface are not significantly affected.

III. SOI Formed by Zone-Melting Recrystallization (ZMR)

Two SOI samples formed by ZMR were obtained from Dr. Chenson Chen of MIT Lincoln Laboratory. The sample preparation is described elsewhere.²³ A SiO₂ layer 2 µm thick was grown by steam oxidation on a single crystal Si substrate. A polycrystalline Si layer 0.5 µm thick was deposited, followed by the deposition of 2 µm of SiO₂ as a capping layer. One sample was used as a control, the other was nitrided in NH₃ at atmospheric pressure at 1100° C for two hours, oxidized in dry O₂ for 20 minutes, and nitrided for an additional

two hours. The purpose of the intermediate oxidation is to reoxidize the surface diffusion barrier which forms as a result of the nitridation (see Chapter 3) so that additional NH_3 is able to enter the film with additional nitridation time. It has been suggested²³ that this procedure results in the introduction of N at the capping SiO_2 /deposited Si interface, which improves the wetting of the capping layer by the molten Si in ZMR and results in superior recrystallized films. However, attempts to detect the N at the interface have been unsuccessful.²³ The purpose of the studies reported here is to determine if N has been incorporated at the interface using XPS, which may be more sensitive than the techniques previously employed.²³

In order to confirm the hypothesis that N is incorporated at the capping SiO_2 /deposited Si interface, the interface must be exposed for study by XPS. It is unlikely that an HF etch through 2 μm of SiO_2 would be uniform enough to come within a few tens of Å of the interface (within one photoelectron escape depth) without nonuniformities developing, making data analysis difficult. Exposure of the interface from the Si side is therefore desirable in this case. In order to expose the interface, the Si substrate, thermally grown SiO_2 layer, and recrystallized Si layer must be removed. This can be done by a XeF_2 etch to remove the Si substrate, followed by a HF etch to remove the thermally grown SiO_2 layer, followed by another XeF_2 etch to remove the recrystallized Si layer. One μm of Al was deposited on the front of both the nitrided and control samples for structural support of the capping layer after removal of the rest of the structure, and both samples were bonded to a Au platen using high-purity In.

It was found that the back of the samples had a thick layer of SiO_2 , apparently originating during the thermal oxidation or the deposition of the capping layer. This was removed with HF prior to exposure of the samples to XeF_2 . After removal of the Si substrate, it was found that the HF etch had apparently also removed the Al film (and probably the capping layer with it). The failure of the Al layer and In bonding to protect the sample surface requires that a method of protecting the surface be found. This problem was solved by removing the backside SiO_2 layer only from the central region of the sample. The XeF_2 etching then would leave a ring of Si around the edge of the sample, which would contain the HF etchant during removal of the buried SiO_2 layer. Removal of the recrystallized Si layer would then expose the capping SiO_2 . In practice, the intended ring of Si was not continuous, and sufficient etchant "escaped" the ring to damage the protective Al layer. As of this writing, the problem of exposing the capping SiO_2 /recrystallized Si interface has not been solved.

Chapter 5

Conclusions

The techniques of XPS, SE, and SEM have been used to study structural and chemical inhomogeneities in several electronic materials and device structures of relevance to radiation hard electronics. In many ways, XPS is complementary to SE and SEM, and this fact has been exploited in this work to elucidate information on chemical and structural properties of the materials and structures studied. The systems studied were MNOS structures, silicon oxynitride formed by the thermal nitridation of SiO_2/Si , and SOI structures. Studies of MNOS structures suggest that the effect of H_2 annealing is to make the $\text{Si}_3\text{N}_4/\text{SiO}_2$ interface less abrupt by causing interdiffusion of silanol and silamine groups with subsequent oxynitride formation. Another effect of the annealing appears to be to relieve the strain at the SiO_2/Si interface.

The thermal nitridation in NH_3 of SiO_2 films on Si results in the formation of an oxynitride film which is inhomogeneous both chemically and structurally. In addition to the structural inhomogeneities inherent in an amorphous material, the oxide near the SiO_2/Si interface (within ~ 30 Å) is also known to be structurally strained and distinct from the bulk SiO_2 . The effect of this strain on the nitridation kinetics has been shown to affect the observed nitrogen distribution in the SiO_xN_y film. The nitrogen concentration depth profiles as a function of oxidation temperature and nitridation time and temperature have been measured using XPS intensity analysis in conjunction with chemical etching. For this material system, SE was found to

be of limited usefulness, providing only some evidence of interface roughening as a result of nitridation. However, this effect could not be quantified in this work. The XPS data show that, at a nitridation temperature of 1000° C, the peak interfacial nitrogen concentration initially occurs at the $\text{SiO}_x\text{N}_y/\text{Si}$ interface, then appears to move ~ 20 Å away from the interface with nitridation time increasing from 10 to 30 minutes. For nitridation times beyond 30 minutes, the distribution of nitrogen within ~ 30 Å of the interface does not change, but nitrogen incorporation continues in the bulk of the film. At a nitridation temperature of 800° C, the peak interfacial nitrogen concentration is observed to remain at the interface for nitridation times up to 4 hours. At a nitridation temperature of 1150° C, the peak in the interfacial nitrogen concentration occurs away from the interface for a nitridation time as short as 5 minutes. The peak interfacial nitrogen concentration occurs about the same distance from the interface as is observed at a nitridation temperature of 1000° C, but saturates at a lower value.

Modeling of the kinetics of the nitridation has been done, and reveals a mechanism in which diffusing species, initially consisting primarily of the nitrogen species, react with the substrate, forming a nitrogen-rich oxynitride at the interface. At sufficiently high nitridation temperatures, an oxygen-rich oxynitride subsequently forms at the interface due to reaction of the substrate with an increasing concentration of diffusing oxygen which has been displaced by the slower nitridation of the oxide. The data are consistent with the mechanism discussed above, provided the influence of the interfacial strain on the nitridation and oxidation kinetics is explicitly accounted for.

Specifically, the effects of interfacial strain must be taken into account to explain the observed width of the peak in the interfacial nitrogen concentration. This is an example of a chemical inhomogeneity being affected by a structural inhomogeneity. The fact that the XPS data qualitatively confirm the predictions of the kinetic model is an indication that the essential physics of the nitridation process is contained in the model, although quantitative discrepancies indicate that the kinetic parameters are not yet optimized. In spite of the discrepancies, the model successfully predicts that (a) the maximum nitrogen concentration in the interfacial region initially occurs at the interface and occurs away from the interface with increasing nitridation time at sufficiently high nitridation temperatures, (b) the maximum nitrogen concentration in the interfacial region remains at the interface even for long nitridation times at low nitridation temperatures, and (c) the peak interfacial nitrogen concentration is lower for the highest nitridation temperature studied. The simulations provide valuable insight into the reasons for these experimentally confirmed observations, and also provide insight into the role of interfacial strain in the nitridation kinetics.

The behavior of $|\Delta V_{FB}|$, the magnitude of the flat band voltage shift, is correlated to the observed nitrogen distributions. This correlation is shown to consistently follow from the simple postulate that it is the strain-dependence of the kinetics of formation of defect states which allow lowering of the system energy by relieving interfacial strain. The distribution of defects is deduced from the intensity of a fluorine marker, and is found to be consistent with the proposed model explaining the behavior of flatband voltage shifts as a

function of nitridation conditions. Macroscopic intrinsic stress is not observed to affect the nitrogen distribution, but does affect the defect formation kinetics. Thus, it can be seen that the observed nitrogen distributions, the kinetics of the nitridation, and the electrical properties of the nitrided oxides can all be explained in a self-consistent manner by taking into account known properties of the initial SiO_2/Si structure.

Studies of SOI structures formed by ion implantation show that the buried oxide/Si interfaces are smoother with higher implantation temperature in the range 400° C to 525° C. While the stoichiometry of the native oxides suggests that a higher implantation temperature results in a rougher surface, the XPS data on chemical depth profiles of the thermal SiO_2 /surface Si interface shows no effect, implying no effect on device characteristics. SOI structures formed by zone-melting recrystallization have also been studied, but these studies have not yielded useful results to date.

References

1. F. J. Grunthaner, P. J. Grunthaner, R. P. Vasquez, B. F. Lewis, J. Maserjian, and A. Madhukar, *J. Vac. Sci. Technol.* **16**, 1443 (1979).
2. F. J. Grunthaner, P. J. Grunthaner, R. P. Vasquez, B. F. Lewis, J. Maserjian, and A. Madhukar, *Phys. Rev. Lett.* **43**, 1683 (1979).
3. R. N. Nucho and A. Madhukar, *Phys. Rev. B* **21**, 1576 (1980).
4. J. A. Wurzbach and F. J. Grunthaner, presented at the 3rd IEEE Non-Volatile Semiconductor Memory Workshop, Monterey, CA, March, 1979.
5. J. A. Wurzbach and F. J. Grunthaner, presented at the 10th IEEE Semiconductor Interface Specialists Conference, New Orleans, LA, November/December, 1979.
6. J. A. Wurzbach, F. J. Grunthaner, and J. Maserjian, presented at the 4th IEEE Non-Volatile Semiconductor Memory Workshop, Vail, CO, August, 1980.
7. J. A. Wurzbach, F. J. Grunthaner, and J. Maserjian, presented at the 28th American Vacuum Society National Symposium, Anaheim, CA, November 3-6, 1981; proceedings published in *J. Vac. Sci. Technol.* **20**, 962 (1982).
8. J. A. Wurzbach, F. J. Grunthaner, and J. Maserjian, presented at the 5th IEEE Non-Volatile Semiconductor Memory Workshop, Monterey, CA, March, 1982.
9. J. A. Wurzbach and F. J. Grunthaner, *J. Electrochem. Soc.* **130**, 691 (1983).
10. R. P. Vasquez and F. J. Grunthaner, presented at the 6th IEEE Non-Volatile Semiconductor Memory Workshop, Vail, CO, August, 1983.
11. R. P. Vasquez, A. Madhukar, F. J. Grunthaner, and M. L. Naiman, presented at the 15th IEEE Semiconductor Interface Specialists Conference, San Diego, CA, December 6-8, 1984.
12. R. P. Vasquez, A. Madhukar, F. J. Grunthaner, and M. L. Naiman, presented at the 7th IEEE Non-Volatile Semiconductor Memory Workshop, March 11-13, 1985.

13. R. P. Vasquez, M. H. Hecht, F. J. Grunthaner, and M. L. Naiman, Appl. Phys. Lett. **44**, 969 (1984).
14. R. P. Vasquez, A. Madhukar, F. J. Grunthaner, and M. L. Naiman, Appl. Phys. Lett. **46**, 361 (1985).
15. R. P. Vasquez and A. Madhukar, Appl. Phys. Lett. **47**, 998 (1985).
16. R. P. Vasquez, A. Madhukar, F. J. Grunthaner, and M. L. Naiman, J. Appl. Phys. **59**, 972 (1986).
17. R. P. Vasquez, A. Madhukar, F. J. Grunthaner, and M. L. Naiman, J. Appl. Phys. **60**, 226 (1986).
18. R. P. Vasquez and A. Madhukar, J. Appl. Phys. **60**, 234 (1986).
19. P. L. F. Hemment, E. Maydell-Ondrusz, K. G. Stephens, J. Butcher, D. Ioannou, and J. Alderman, Nucl. Instrum. Methods **209/210**, 157 (1983).
20. C. G. Tuppen, M. R. Taylor, P. L. F. Hemment, and R. P. Arrowsmith, Appl. Phys. Lett. **45**, 57 (1984).
21. P. L. F. Hemment, E. A. Maydell-Ondrusz, J. E. Castle, R. Paynter, M. C. Wilson, R. G. Booker, J. A. Kilner, and R. P. Arrowsmith, Thin Solid Films **128**, 125 (1985).
22. J. R. Davis, M. R. Taylor, G. D. T. Spiller, P. J. Skevington, and P. L. F. Hemment, Appl. Phys. Lett. **48**, 1279 (1986).
23. C. K. Chen, M. W. Geis, M. C. Finn, and B-Y. Tsaur, Appl. Phys. Lett. **48**, 1300 (1986).
24. e. g. see J. I. Goldstein, D. E. Newbury, P. Echlin, D. C. Joy, C. Fiori, and E. Lifshin, *Scanning Electron Microscopy and X-ray Microanalysis* (Plenum Press, New York, 1981).
25. T. A. Carlson, *Photoelectron and Auger Spectroscopy* (Plenum Press, New York, 1975).
26. M. Cardona and L. Ley, in *Photoemission in Solids I: General Principles*, edited by M. Cardona and L. Ley (Springer-Verlag, New York, 1978), p. 1.
27. D. A. Shirley, *ibid.*, p. 165.

28. C. S. Fadley, in *Electron Spectroscopy: Theory, Techniques, and Applications*, edited by C. R. Brundle and A. D. Baker (Academic Press, New York, 1978), p. 1.
29. M. H. Hecht, F. J. Grunthaner, P. Pianetta, L. I. Johansson, and I. Lindau, *J. Vac. Sci. Technol. A* **2**, 584 (1984).
30. C. S. Fadley, R. J. Baird, W. Siekhaus, T. Novakov, and S. A. L. Bergstrom, *J. Electron Spectrosc. Rel. Phenom.* **4**, 93 (1974).
31. C. S. Fadley, *Prog. Surf. Sci.* **16**, 275 (1984), and references therein.
32. T. D. Bussing and P. H. Holloway, *J. Vac. Sci. Technol. A* **3**, 1973 (1985).
33. H. Iwasaki, R. Nishitani, and S. Nakamura, *Jap. J. Appl. Phys.* **17**, 1519 (1978).
34. M. Pijolat and G. Hollinger, *Surf. Sci.* **105**, 114 (1981).
35. P. J. Grunthaner, R. P. Vasquez, and F. J. Grunthaner, *J. Vac. Sci. Technol.* **17**, 1045 (1980).
36. R. P. Vasquez and F. J. Grunthaner, *Surf. Sci.* **99**, 681 (1980).
37. M. H. Hecht, R. P. Vasquez, and F. J. Grunthaner, presented at the 14th IEEE Semiconductor Interface Specialists Conference, Ft. Lauderdale, FL, December 1-3, 1983.
38. M. H. Hecht, R. P. Vasquez, F. J. Grunthaner, N. Zamani, and J. Maserjian, *J. Appl. Phys.* **57**, 5256 (1985), and references therein.
39. D. E. Aspnes, in *Optical Properties: New Developments*, edited by B. O. Seraphin (North-Holland, Amsterdam, 1976), p. 799.
40. J. B. Theeten and D. E. Aspnes, *Ann. Rev. Mater. Sci.* **11**, 97 (1981).
41. M. Born and E. Wolf, *Principles of Optics*, 6th edition (Pergamon, New York, 1980).
42. R. M. A. Azzam and N. M. Bashara, *Ellipsometry and Polarized Light* (North-Holland, New York, 1977).
43. D. E. Aspnes and A. A. Studna, *Appl. Opt.* **14**, 220 (1975).
44. R. P. Vasquez, A. Madhukar, and A. R. Tanguay, Jr., *J. Appl. Phys.* **58**, 2337 (1985).

45. D. E. Aspnes, J. B. Theeten, and F. Hottier, *Phys. Rev. B* **20**, 3292 (1979).
46. D. E. Aspnes, *Am. J. Phys.* **50**, 704 (1982), and references therein.
47. D. E. Aspnes and J. B. Theeten, *J. Electrochem. Soc.* **127**, 1359 (1980).
48. D. E. Aspnes and J. B. Theeten, *J. Appl. Phys.* **50**, 4928 (1979).
49. R. P. Vasquez, J. D. Klein, J. J. Barton, and F. J. Grunthaner, *J. Electron Spectrosc. Rel. Phenom.* **23**, 63 (1981).
50. T. Ito, T. Nozaki, and H. Ishikawa, *J. Electrochem. Soc.* **127**, 2053 (1980).
51. M. L. Naiman, F. L. Terry, J. A. Burns, J. L. Raffel, and R. Aucoin, *IEEE IEDM 80*, 562 (1980).
52. S. S. Wong, C. G. Sodini, T. W. Ekstedt, H. R. Grinolds, K. H. Jackson, S. H. Kwan, and W. G. Oldham, *J. Electrochem. Soc.* **130**, 1139 (1983).
53. T. Ito, T. Nakamura, and H. Ishikawa, *IEEE Trans. Electron Devices* **ED-29**, 498 (1982); *J. Electrochem. Soc.* **129**, 184 (1982).
54. F. L. Terry, M. L. Naiman, R. J. Aucoin, and S. D. Senturia, *IEEE Trans. Nucl. Sci.* **NS-28**, 4389 (1981).
55. F. L. Terry, R. J. Aucoin, M. L. Naiman, and S. D. Senturia, *IEEE Electron Dev. Lett.* **EDL-4**, 191 (1983).
56. R. K. Pancholy and F. M. Erdman, *IEEE Trans. Nucl. Sci.* **NS-30**, 4141 (1983).
57. C. T. Chen, F. C. Tseng, C. Y. Chang, and M. K. Lee, *J. Electrochem. Soc.* **131**, 875 (1984).
58. P. Pan and C. Paquette, *Appl. Phys. Lett.* **47**, 473 (1985).
59. F. H. P. M. Habraken, A. E. T. Kuiper, and Y. Tamminga, *Phys. J. Res* **38**, 19 (1983).
60. Y. Hayafuji and K. Kajiwara, *J. Electrochem. Soc.* **129**, 2102 (1982).
61. M. L. Naiman, C. T. Kirk, R. J. Aucoin, F. L. Terry, R. W. Wyatt, and S. D. Senturia, *J. Electrochem. Soc.* **131**, 637 (1984).
62. F. H. P. M. Habraken, E. J. Evers, and A. E. T. Kuiper, *Appl. Phys. Lett.* **44**, 62 (1984).

63. J. Amano and T. Ekstedt, Appl. Phys. Lett. **41**, 816 (1982).
64. F. H. P. M. Habraken, A. E. T. Kuiper, Y. Tamminga, and J. B. Theeten, J. Appl. Phys. **53**, 6996 (1982).
65. Y. Yorume, J. Vac. Sci. Technol. B **1**, 67 (1983).
66. M. L. Naiman, C. T. Kirk, B. L. Emerson, J. B. Taitel, and S. D. Senturia, J. Appl. Phys. **58**, 779 (1985).
67. M. M. Moslehi and K. C. Saraswat, IEEE Trans. Electron Devices **ED-32**, 106 (1985).
68. C. J. Han, M. M. Moslehi, C. R. Helms, and K. C. Saraswat, Appl. Phys. Lett. **46**, 641 (1985); J. Vac. Sci. Technol. A **3**, 804 (1985).
69. M. M. Moslehi, C. J. Han, K. C. Saraswat, C. R. Helms, and S. Shatas, J. Electrochem. Soc. **132**, 2189 (1985).
70. F. L. Terry, private communication.
71. R. H. Doremus, *Glass Science* (Wiley, New York, 1973), and references therein; J. Am. Ceram. Soc. **49**, 461 (1966).
72. R. H. Doremus, in *Reactivity of Solids*, Eds. J. W. Mitchell, R. C. DeVries, R. W. Roberts, and P. Cannon (Wiley-Interscience, New York, 1969) p. 667; J. Phys. Chem. **80**, 1773 (1976).
73. A. J. Moulson and J. P. Roberts, Trans. Faraday Soc. **57**, 1208 (1961).
74. E. A. Irene, E. Tierney, and J. Angilello, J. Electrochem. Soc. **129**, 2594 (1982), and references therein.
75. A. Fairgeix and G. Ghibaudo, J. Appl. Phys. **54**, 7153 (1983).
76. F. J. Grunthaner, B. F. Lewis, N. Zamani, J. Maserjian, and A. Madhukar, IEEE Trans. Nucl. Sci. **NS-27**, 1640 (1980).
77. F. J. Grunthaner, P. J. Grunthaner, and J. Maserjian, IEEE Trans. Nucl. Sci. **NS-29**, 1462 (1982).
78. J. Singh and A. Madhukar, J. Vac. Sci. Technol. **19**, 437 (1981).
79. F. J. Grunthaner, B. F. Lewis, R. P. Vasquez, J. Maserjian, and A. Madhukar, in *The Physics of MCS Insulators*, Ed. G. Lucovsky (Pergamon, New York, 1980) p. 290.

80. F. J. Grunthaner, B. F. Lewis, J. Maserjian, and A. Madhukar, *J. Vac. Sci. Technol.* **20**, 747 (1982).
81. J. H. Scofield, *J. Electron Spectrosc. Rel. Phenom.* **8**, 129 (1976).
82. S. Isomae, *J. Appl. Phys.* **57**, 216 (1985), and references therein.
83. V. Zakeriya and T-P. Ma, *J. Appl. Phys.* **56**, 1017 (1984); *Appl. Phys. Lett.* **45**, 249 (1984); *IEEE Trans. Nucl. Sci.* **NS-31**, 1261 (1984).
84. V. Zakeriya, A. Wong, and T-P. Ma, *Appl. Phys. Lett.* **46**, 80 (1985).
85. M. Severi, L. Dori, and M. Impronta, *IEEE Electron Device Lett.* **EDL-6**, 3 (1985).
86. I. Colquhoun, S. Wild, P. Grieveson, and K. H. Jack, *Proc. Brit. Ceram. Soc.* **22**, 207 (1973).
87. I. Idrestedt and C. Brosset, *Acta Chem. Scand.* **18**, 1879 (1964).
88. W. Y. Ching and S. Y. Ren, *Phys. Rev. B* **24**, 5788 (1981).
89. R. Marchand and J. Lang, *C. R. Acad. Sci., Paris, Ser. C* **264**, 969 (1967).
90. J. Crank, *The Mathematics of Diffusion* (Clarendon Press, Oxford, 1975).
91. P. J. Grunthaner and M. H. Hecht, unpublished.
92. B. E. Deal and A. S. Grove, *J. Appl. Phys.* **36**, 3770 (1965).
93. R. R. Razouk, L. N. Lie, and B. E. Deal, *J. Electrochem. Soc.* **128**, 2214 (1981).
94. L. N. Lie, R. R. Razouk, and B. E. Deal, *J. Electrochem. Soc.* **129**, 2828 (1982).
95. H. Z. Massoud, J. D. Plummer, and E. A. Irene, *J. Electrochem. Soc.* **132**, 1745 (1985).
96. S. P. Murarka, C. C. Chang, and A. C. Adams, *J. Electrochem. Soc.* **126**, 996 (1979).
97. C. Y. Wu, C. W. King, M. K. Lee, and C. T. Chen, *J. Electrochem. Soc.* **129**, 1559 (1982).

98. J. R. Manning, *Diffusion Kinetics for Atoms in Crystals* (E. Van Nostrand Co., Princeton, NJ, 1968).
99. W. A. Tiller, *J. Electrochem. Soc.* **130**, 501 (1983).
100. A. Fargeix, G. Ghibaudo, and G. Kamarinos, *J. Appl. Phys.* **54**, 2878 (1983).
101. K. K. Ng, W. J. Polito, and J. R. Ligenza, *Appl. Phys. Lett.* **44**, 626 (1984).
102. E. A. Irene, *J. Appl. Phys.* **54**, 5416 (1983).
103. J. B. Theeten, R. P. H. Chang, D. E. Aspnes, and T. E. Adams, *J. Electrochem. Soc.* **127**, 378 (1980).
104. B.-Y. Mao, P.-H. Chang, H. W. Lam, B. W. Shen, and J. A. Keenan, *Appl. Phys. Lett.* **48**, 794 (1986).
105. J. Stoemenos, J. Margail, C. Jaussaud, M. Dupuy, and M. Bruel, *Appl. Phys. Lett.* **48**, 1470 (1986).
106. A. Mogro-Campero, R. P. Love, N. Lewis, E. L. Hall, and M. D. McConnell, *J. Appl. Phys.* **60**, 2103 (1986).
107. G. K. Celler, P. L. F. Hemment, K. W. West, and J. M. Gibson, *Appl. Phys. Lett.* **48**, 532 (1986).
108. H. U. Jager, E. Hensel, U. Kreissig, W. Skorupa, and E. Sobeslavsky, *Thin Solid Films* **123**, 159 (1985).
109. P. L. F. Hemment, R. F. Peart, M. F. Yao, K. G. Stephens, R. J. Chater, J. A. Kilner, D. Meekison, G. R. Booker, and R. P. Arrowsmith, *Appl. Phys. Lett.* **46**, 952 (1985).
110. L. Nesbit, S. Stiffler, G. Slusser, and H. Vinton, *J. Electrochem. Soc.* **132**, 2713 (1985).
111. D. Eirug Davies, J. A. Adamski, and E. F. Kennedy, *Appl. Phys. Lett.* **48**, 347 (1986).
112. Z. Liliental, R. W. Carpenter, and J. C. Kelly, *Thin Solid Films* **138**, 141 (1986).
113. L. Nesbit, G. Slusser, R. Frenette, and R. Halbach, *J. Electrochem. Soc.* **133**, 1186 (1986).
114. L. O. Wilson and G. K. Celler, *J. Electrochem. Soc.* **132**, 2748 (1985).

115. P. J. Grunthaner, M. H. Hecht, F. J. Grunthaner, and N. M. Johnson, J. Appl. Phys. **61**, 629 (1987).
116. P. L. F. Hemment, private communication.
117. B. L. Henke, Phys. Rev. A **6**, 94 (1972).
118. T. A. Carlson and G. E. McGuire, J. Electron Spectrosc. Rel. Phenom. **1**, 161 (1972/73).
119. C. D. Wagner, L. E. Davis, and W. M. Riggs, Surf. Interface Anal. **2**, 53 (1980).
120. J. C. Ashley and C. J. Tung, Surf. Interface Anal. **4**, 52 (1982).
121. C. J. Powell, Surf. Sci. **44**, 29 (1974).
122. R. Flitsch and S. I. Raider, J. Vac. Sci. Technol. **12**, 305 (1975).
123. J. M. Hill, D. G. Royce, C. S. Fadley, L. F. Wagner, and F. J. Grunthaner, Chem. Phys. Lett. **44**, 225 (1976).
124. H. Iwasaki and S. Nakamura, Surf. Sci. **57**, 779 (1976).

Appendix A

Intensity Analysis of XPS Data

In the present work, the distribution of nitrogen in nitrided oxide films is the desired quantity. An inhomogeneous nitrogen distribution as a function of depth in the film is evident in the behavior of the O 1s and N 1s intensities,¹⁷ as discussed in Chapter 3. However, this behavior is biased by the averaging effect of the relatively long photoelectron mean free paths, and by the fact that N 1s and O 1s photoelectrons have different photoionization cross sections, and have significantly different kinetic energies, and hence different mean free paths. An unbiased measure of the nitrogen distribution is required. In the following, the simpler case of a homogeneous film will first be considered, then the generalization to the case of an inhomogeneous film composition will be presented.

The intensity of photoelectrons of a given kinetic energy emitted from a homogenous material is a well known function.^{17,25-34,36,117-124} Let E_x be the x-ray energy, σ_{N1s} the N 1s photoionization cross section, $D_{N,ox}$ the atomic number density of N in the oxynitride (SiO_xN_y), and $\lambda_{N1s,ox}(E_{N1s})$ the inelastic mean free path of N 1s photoelectrons with kinetic energy E_{N1s} in SiO_xN_y . In the present work, E_x , and hence the kinetic energy of photoelectrons from a given core level, does not vary. The explicit dependence of σ and λ on energy will therefore no longer be written, but rather will be implicit in the use of different λ 's for different core levels. The intensity of N 1s photoelectrons from SiO_xN_y , $dI_{N1s,ox}$, which originate between z and $z + dz$ below the surface is given by

$$dI_{N1s,ox} = K\sigma_{N1s}D_{N,ox}\exp[-z/\lambda_{N1s,ox}\sin\theta]dz \quad (A1)$$

where K is a spectrometer constant depending on such factors as x-ray flux and detector efficiency and θ is the angle between the plane of the surface and the detector. The total detected intensity of photoelectrons from a semi-infinite homogeneous sample, such as Si 2p photoelectrons from a Si substrate, would be

$$I_{Si2p,Si} = \int_0^{\infty} K\sigma_{Si2p}D_{Si,Si}\exp[-z/\lambda_{Si2p,Si}\sin\theta]dz = K\sigma_{Si2p}D_{Si,Si}\lambda_{Si2p,Si}\sin\theta \quad (A2)$$

The total detected intensity of photoelectrons from a film of finite thickness such as N 1s photoelectrons from a SiO_xN_y film of thickness t_{ox} on Si, is

$$\begin{aligned} I_{N1s,ox}(t_{ox}) &= \int_0^{t_{ox}} K\sigma_{N1s}D_{N,ox}\exp[-z/\lambda_{N1s,ox}\sin\theta]dz \\ &= K\sigma_{N1s}D_{N,ox}\lambda_{N1s,ox}\sin\theta(1-\exp[-t_{ox}/\lambda_{N1s,ox}\sin\theta]) \end{aligned} \quad (A3)$$

The total intensity of the substrate Si 2p photoelectrons detected through the SiO_xN_y film is

$$\begin{aligned}
I_{Si2p, Si}(t_{ox}) &= \int_{t_{ox}}^{\infty} K \sigma_{Si2p} D_{Si, Si} \exp[-(z - t_{ox})/\lambda_{Si2p, Si} \sin \theta] \exp[-t_{ox}/\lambda_{Si2p, ox} \sin \theta] dz \\
&= K \sigma_{Si2p} D_{Si, Si} \lambda_{Si2p, Si} \sin \theta \exp[-t_{ox}/\lambda_{Si2p, ox} \sin \theta].
\end{aligned}
\tag{A4}$$

Eq. (A4) can be divided by Eq. (A2) to obtain

$$I_{Si2p, Si}(t_{ox})/I_{Si2p, Si}(0) = \exp[-t_{ox}/\lambda_{Si2p, ox} \sin \theta]. \tag{A5}$$

For notational convenience the following symbol is defined:

$$\Delta_N = D_{N, ox} \lambda_{N1s, ox} / D_{Si, Si} \lambda_{Si2p, Si}. \tag{A6}$$

We shall hereafter assume that the intensities are all divided by the appropriate photoionization cross sections, which are well known.⁸¹ Eq. (A3) can then be divided by Eq. (A4) to obtain

$$I_{N1s, ox}(t_{ox})/I_{Si2p, Si}(t_{ox}) = \Delta_N (1 - \exp[-t_{ox}/\lambda_{N1s, ox} \sin \theta]) / \exp[-t_{ox}/\lambda_{Si2p, ox} \sin \theta]. \tag{A7}$$

A similar equation can be written for the intensity of O1s photoelectrons. Note that, from Eq. (A5), t_{ox} can be determined if $\lambda_{N1s, ox}$ is known, or $\lambda_{N1s, ox}$ can be determined if t_{ox} is independently measured. $D_{Si, Si}$ and $\lambda_{Si2p, Si}$ have been measured,^{46,49,75} so that, if $\lambda_{N1s, ox}$ is known or can be estimated, $D_{N, ox}$ can be determined from Eq. (A7). In the present situation, the assumption of a

homogeneous film is invalid. For inhomogeneous films both D and λ are, in general, functions of z . The above equations must therefore be generalized to include inhomogeneous films. We begin by assuming that a film of thickness t_{ox} can be approximated by a finite number of layers, each of which is homogeneous. The i^{th} layer below the surface can then be characterized by D_i and λ_i (and hence Δ_i), and by its boundaries z_{i-1} and z_i , where $z_0 (= 0)$ is the surface. Eq. (A3) can then be rewritten as

$$\begin{aligned}
 I_{N1s,ox}(t_{ox}) &= K \int_0^{t_{ox}} D_{N,ox}(z) \exp[-z/\lambda_{N1s,ox}(z) \sin\theta] dz \\
 &= K \sum_{i=1}^n D_{i,N,ox} \int_{z_{i-1}}^{z_i} \exp[-z/\lambda_{i,N1s,ox} \sin\theta] dz \\
 &= K \sin\theta \sum_{i=1}^n D_{i,N,ox} \lambda_{i,N1s,ox} \{1 - \exp[-(z_i - z_{i-1})/\lambda_{i,N1s,ox} \sin\theta]\} \\
 &\quad \times \exp[-z_{i-1}/\lambda_{i,N1s,ox} \sin\theta].
 \end{aligned} \tag{A8}$$

The thickness of the i^{th} layer is defined by

$$t_i = z_i - z_{i-1}, \tag{A9}$$

so that

$$t_{ox} = \sum_{i=1}^n t_i. \tag{A10}$$

The z_{i-1} in the last exponent of Eq. (A8) can be replaced by

$$z_{i-1} = \sum_{j=1}^{i-1} (z_j - z_{j-1}) = \sum_{j=1}^{i-1} t_j. \quad (\text{A11})$$

Equations (A9) and (A11) can be substituted into Eq. (A8) and t_0 can be defined to be 0 to give

$$I_{N1s,ox}(t_{ox}) = K \sin \theta \sum_{i=1}^n D_{i,N,ox} \lambda_{i,N1s,ox} (1 - \exp[-t_i / \lambda_{i,N1s,ox} \sin \theta]) \times \prod_{j=0}^{i-1} \exp[-t_j / \lambda_{j,N1s,ox} \sin \theta]. \quad (\text{A12})$$

Similarly, Eq. (A4) can be rewritten as

$$I_{Si2p,Si}(t_{ox}) = K \sin \theta D_{Si,Si} \lambda_{Si2p,Si} \prod_{i=0}^n \exp[-t_i / \lambda_{i,Si2p,ox} \sin \theta]. \quad (\text{A13})$$

Equation (A12) can be divided by Eq. (A13) to obtain

$$\begin{aligned}
I_{N1s,ox}(t_{ox})/I_{Si2p,Si}(t_{ox}) &= \sum_{i=1}^n \Delta_{i,N} (1 - \exp[-t_i/\lambda_{i,N1s,ox} \sin\theta]) \\
&\times \prod_{j=0}^{i-1} \exp[-t_j/\lambda_{j,N1s,ox} \sin\theta] \prod_{k=0}^n \exp[t_k/\lambda_{k,Si2p,ox} \sin\theta] \quad (A14)
\end{aligned}$$

Equation (A14) is the same as an expression previously given³⁶ (but not derived), but generalized to include the energy dependence of the mean free paths, and $z = 0$ is now defined at the film surface, rather than at the film/substrate interface as was done previously.³⁶

It has previously been shown¹¹⁹⁻¹²¹ that the mean free path depends on the photoelectron kinetic energy via the relation $\lambda \propto E^p$, where p is in the range 0.70 - 0.81 for Si and SiO₂. For this work, $p = 0.75$ has been chosen. In Eq. (A14), $\lambda_{i,N1s,ox}$ can then be replaced by utilizing the relation

$$\lambda_{i,N1s,ox} = (E_{N1s}/E_{Si2p})^{0.75} \lambda_{i,Si2p,ox} \quad (A15)$$

For notational convenience, the following symbol is defined:

$$A_N = (E_{Si2p}/E_{N1s})^{0.75} \quad (A16)$$

Substituting Eqs. (A15) and (A16) into Eq. (A14), the following relation is obtained

$$\begin{aligned}
I_{N1s,ox}(t_{ox})/I_{Si2p,Si}(t_{ox}) &= \sum_{i=1}^n \Delta_{i,N} (1 - \exp[-t_i A_N / \lambda_{i,Si2p,ox} \sin \theta]) \\
&\times \prod_{j=0}^{i-1} \exp[-t_j (A_N - 1) / \lambda_{j,Si2p,ox} \sin \theta] \prod_{k=i}^n \exp[t_k / \lambda_{k,Si2p,ox} \sin \theta] .
\end{aligned} \tag{A17}$$

Equation (A17) can be rewritten as

$$\begin{aligned}
I_{N1s,ox}(t_{ox})/I_{Si2p,Si}(t_{ox}) &= I_{N1s,ox}(t_{ox} - t_1)/I_{Si2p,Si}(t_{ox} - t_1) \\
&+ \Delta_{1,N} (1 - \exp[-t_1 A_N / \lambda_{1,Si2p,ox} \sin \theta]) \prod_{i=1}^n \exp[t_i / \lambda_{i,Si2p,ox} \sin \theta] .
\end{aligned} \tag{A18}$$

Equation (A13) can also be written as

$$I_{Si2p,Si}(t_{ox})/I_{Si2p,Si}(t_{ox} - t_1) = \exp[-t_1 / \lambda_{1,Si2p,ox} \sin \theta] , \tag{A19}$$

and also as

$$I_{Si2p,Si}(t_{ox})/I_{Si2p,Si}(0) = \prod_{i=1}^n \exp[-t_i / \lambda_{i,Si2p,ox} \sin \theta] . \tag{A20}$$

Substituting Eqs. (A19) and (A20) into Eq. (A18), the following expression is obtained

$$\Delta_{1,N} = \left\{ \frac{I_{N1s,ox}(t_{ox})}{I_{Si2p,Si}(t_{ox} - t_1)} - \frac{I_{N1s,ox}(t_{ox} - t_1)}{I_{Si2p,Si}(t_{ox})} \right\} \quad (A21)$$

$$\times \left\{ \frac{I_{Si2p,Si}(0)}{I_{Si2p,Si}(t_{ox} - t_1)} \left[1 - \left(\frac{I_{Si2p,Si}(t_{ox})}{I_{Si2p,Si}(t_{ox} - t_1)} \right)^{A_N} \right] \right\}^{-1}.$$

Equation (A21) reduces to the expression previously derived³⁶ if $A_N = 1$, i.e. if the kinetic energy dependence of the photoelectron inelastic mean free path can be neglected. Using the O 1s photoelectron intensities and kinetic energy, expressions similar to Eqs. (A15) and (A21) can be obtained for A_O and $\Delta_{1,O}$. It is to be noted that the parameters $\Delta_{1,N}$ and $\Delta_{1,O}$ can be calculated entirely from the known quantities A_N and A_O and from the photoelectron intensities measured at film thicknesses of zero, t_{ox} , and $t_{ox} - t_1$. $\Delta_{1,N}$ and $\Delta_{1,O}$ are measures of the composition of the surface layer of thickness t_1 . The relative concentration of N in the surface layer is directly given by

$$[N]/([O] + [N]) = D_{1,N,ox}/(D_{1,O,ox} + D_{1,N,ox}) = A_N \Delta_{1,N}/(A_O \Delta_{1,O} + A_N \Delta_{1,N}). \quad (A22)$$

Measurement of the photoelectron intensities for n different values of z_i , including $z_i = t_{ox}$ (i.e. the substrate intensity with no overlayer), yields $n - 1$ values of $\Delta_{1,N}$ and $\Delta_{1,O}$, and thus the relative concentration of N as a function of depth in the nitrided oxide film can be obtained. It is to be noted that a measure of the homogeneity of the film can also be obtained at a fixed thickness by varying θ ,³⁰⁻³⁴ or by varying the x-ray photon energy.²⁹ To obtain a thickness scale, note that Eq. (A20) can be rewritten as

$$\sum_{i=1}^n t_i / \lambda_{Si2p,ox} = -\sin\theta \ln[I_{Si2p,Si}(\sum_{i=1}^n t_i) / I_{Si2p,Si}(0)] \quad (A23)$$

To obtain the depth scales shown in Figs. 3.1 to 3.8, it was assumed that $\lambda_{Si2p,ox}$ was not a function of depth in the film, and that $\lambda_{Si2p,ox} = \lambda_{Si2p,SiO_2}$. The values reported for λ_{Si2p,SiO_2} when $E_x = 1486.6$ eV are generally in the range^{29,36,122} 27 to 30 Å, although values as high as 36 Å have been reported^{29,123} for some SiO₂ films. For this work, $\lambda_{Si2p,ox} = 29$ Å was used for the purpose of obtaining the depth scales in Figs. 3.1 to 3.8 via Eq. (A23).



MISSION of *Rome Air Development Center*

RADC plans and executes research, development, test and selected acquisition programs in support of Command, Control, Communications and Intelligence (C³I) activities. Technical and engineering support within areas of competence is provided to ESD Program Offices (POs) and other ESD elements to perform effective acquisition of C³I systems. The areas of technical competence include communications, command and control, battle management information processing, surveillance sensors, intelligence data collection and handling, solid state sciences, electromagnetics, and propagation, and electronic reliability/maintainability and compatibility.